ERDA/JPL-954144-77/82
Distribution Category UC-63

SILICON RIBBON GROWTH BY A CAPILLARY ACTION SHAPING TECHNIQUE

G. H. Schwuttke, Principal Investigator, 914 - 897-3140
International Business Machines Corporation
East Fishkill Laboratories
Hopewell Junction, New York 12533

Quarterly Technical Progress Report Number 8
July 1, 1977

prepared by:
G. H. Schwuttke, T. F. Ciszek, A. Kran, and K. Yang

Under JPL Contract Number: 954144
(Subcontract under NASA Contract NAS7-100)
(Task Order No. RD-152)
Effective Date of Contract: 5/8/75
Contract Expiration Date: 11/8/77

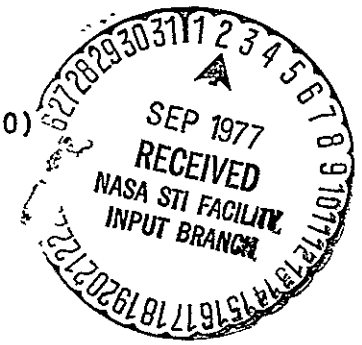

This work was performed for the Jet Propulsion Laboratory, California Institute of Technology, under NASA Contract NAS7-100 for the U. S. Energy Research and Development Administration, Division of Solar Energy.

The JPL Low-Cost Silicon Array Project is funded by ERDA and forms part of the ERDA Photovoltaic Conversion Program to initiate a major effort toward the development of low-cost solar arrays.

CONTENTS

CONTENTS (cont'd)

TECHNICAL CONTENT STATEMENT

This report contains information prepared by the International Business Machines Corporation under JPL contract. Its contents are not necessarily endorsed by the Jet Propulsion Laboratory, California Institute of Technology, or by the National Aeronautics and Space Administration.

RESEARCH PROGRAM PLAN

OBJECTIVES

1. Technological assessment of ribbon growth of silicon by a capillary action shaping technique.

2. Economic evaluation of ribbon silicon grown by a capillary action shaping technique as low-cost silicon.

SYNOPSIS OF PROGRAM OF STUDY

1. Crystal growth of silicon ribbons.

2. Characterization of silicon ribbons.

3. Economic evaluations and computer-aided simulation of ribbon growth.

EIGHTH QUARTER HIGHLIGHTS

- Over 25 meters of 50 mm wide ribbon was grown during the quarter.

- Meniscus heights were measured to lie in the range 0.6-0.8 mm for 0.25 mm thick ribbons.

- A single 50-mm SiC-coated graphite die has been used to grow 17 ribbons (13 meters) of which 7 were completely free of SiC surface particles.

- Ribbon stress levels were measured to lie in the range 2-7 x 10^8 dynes/cm^2.

- A 100-mm-wide ribbon growth furnace has been designed.

- Electrically active defects in CAST ribbons were identified as silicon carbide inclusions, high and low angle grain boundaries high order twins boundaries, multiple stacking faults, dislocation bands and dislocations.

- The electrical activity of grown-in dislocations due to their low density is only moderate. Grown-in

dislocations are generated by thermal gradients associated with the growth technique. Their density varies from 3×10^3 to 5×10^5 per cm^2.

- Dislocation bands with densities larger than 10^6 dislocations/cm^2 are strongly active. They consist of two groups of dislocations. One group is inclined towards the ribbon surface, while the other is almost parallel to ribbon surface in the growth direction. Both groups of dislocations have the same type of Burgers vectors, a/2 [011] and a/2 [101]. Dislocation networks are formed through the interaction of the two dislocations which leads to the formation of 90 degree dislocations.

- Grain boundaries are strongly active. Their formation results mainly from foreign inclusion such as silicon carbide or from the non-accommodation of crystal lattice planes. Such non-accommodation of crystal lattices occurs when two crystals of different preferred orientation, such as [011] and [211] orientations, join. The boundaries contain dislocations and/or ledges which are spaced approximately 0.1 μm apart.

- First order (coherent) twins and stacking faults are

nonactive. Their electrical activity increases as they degenerate into multiple overlapping faults and low-angle boundaries. The low-angle boundaries contain a high density of dislocations. The dislocation spacing ranges from 0.1 to 0.4 μm with an average of 0.2 μm. Degenerated twins act as dislocation sources.

- Float-zone technology is potentially less expensive than Czochralski technology and, consequently, should be rapidly developed and automated to the level of today's Czochralski technology.

- Float-zone technology can potentially outproduce Czochralski technology by a factor of 3.

NINTH QUARTER ACTIVITY PLAN

- Install and Test 100 mm growth system.
- Refine meniscus height measurement and determine process dependencies.
- Complete evaluation of SiC-coated graphite die.
- Evaluate die materials furnished by JPL.

CRYSTAL GROWTH

by

T. F. Ciszek

1.0 INTRODUCTION

The crystal-growth method under investigation is a capillary action shaping technique. Meniscus shaping for the desired ribbon geometry occurs at the vertex of a wettable die. As ribbon growth depletes the melt meniscus, capillary action supplies replacement material. The configuration of the technique used in our initial studies is shown in Fig. 1 and is similar to the edge-defined, film-fed growth (EFG) process described by LaBelle[1]. The crystal-growth method has been applied to silicon ribbons for several years[2,3,4]. As our work on silicon ribbon growth has progressed, we have found that substantial improvements in ribbon surface quality could be achieved with a higher melt meniscus than that attainable with the EFG technique. Thus, in our later work we have abandoned the EFG technique in favor of the improved capillary action shaping technique which employs the capillary die design shown in Fig. 2.

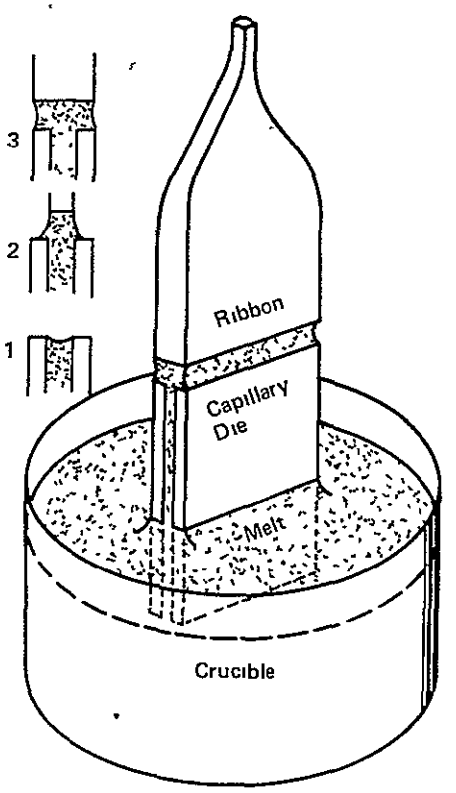

Fig. 1. A schematic diagram of the capillary action shaping technique for silicon ribbon growth.

It represents a departure from the die types used for edge-defined, film-fed growth, in that the bounding edges of the die top are not parallel or concentric with the growing ribbon. The new dies allow a higher central melt meniscus (Fig. 3) with concomitant improvements in surface smoothness and freedom from SiC surface particles, which can degrade perfection.

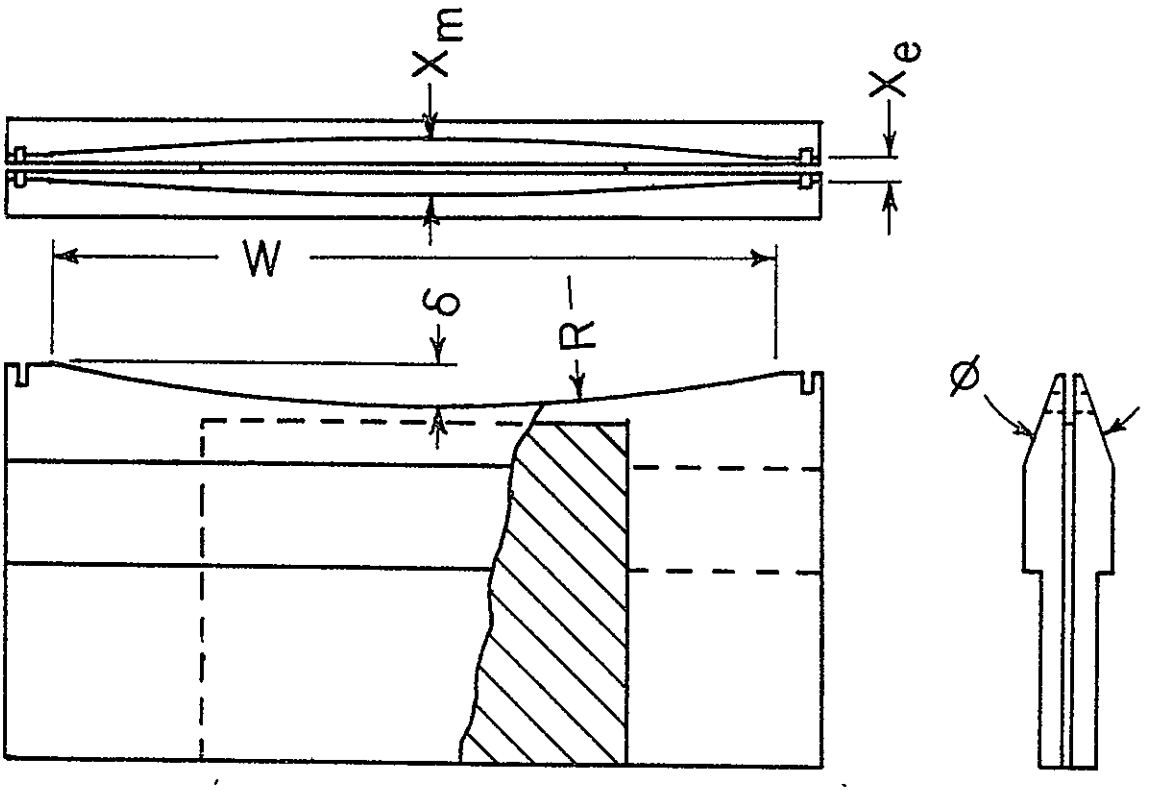

Fig. 2. Die for improved capillary action shaping technique ribbon growth.

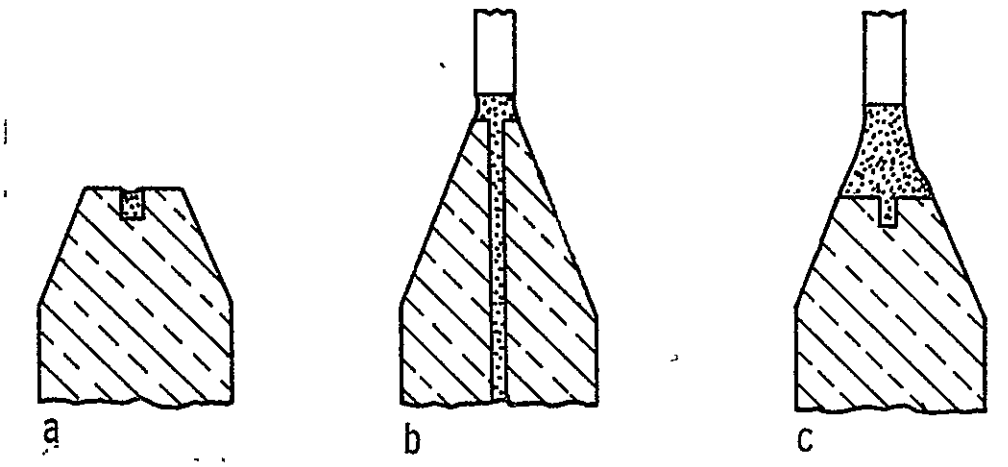

Fig. 3. Cross section through die and ribbon: (a) central die top before seeding, (b) near edge of die during growth, and (c) near central region of die top during growth.

Certain problems still await solution before the technique becomes viable for large-scale economical photovoltaic applications. High-density graphite fulfills the durability and wettability requirements of a die[2] and has been used, to date, for most silicon ribbon growth; it is not, however, completely non-reactive. Good crystallographic perfection has been achieved on small ribbon segments[2,3], but the structure of large ribbons is marred by planar, line, and point defects.

Our objective in this work is to attain a clear technological assessment of silicon ribbon growth by the capillary action shaping technique and to enhance the applicability of the technique to photovoltaic power device material.

In this report, our progress in 50-mm-wide ribbon growth is presented. Twenty-five meters of ribbon were grown during the quarter, more than half of which was shaped with a single SiC-coated graphite die. Meniscus geometry has been detailed. Meniscus heights of 0.6-0.8 mm are typical for 0.2 to 0.4 mm thick ribbons grown by the CAST method. Seven ribbons completely free of SiC surface particles and eleven ribbons with a particle density of $< 3 \times 10^{-3}/cm^2$ were grown. Stress levels of the 50 mm ribbons were found to be in the range of $2\text{-}7 \times 10^8$ dynes/cm^2. A 100-mm-wide ribbon growth system has been designed.

2.0 GROWTH EXPERIMENTS

2.1 General Description

Forty-nine growth runs were made since the last reporting period, resulting in 36 silicon ribbons. The total length was 28.8 meters, of which 24.8 meters was 50 mm wide ribbon and 4 meters was 38 mm wide ribbon. Minimum thicknesses ranged from 0.09 to 0.82 mm, and maximum thicknesses ranged from 0.17 to 1.10 mm. The fastest growth rate attained to date was for ribbon 70411. The thickness was 0.15 mm at a 4-cm/min growth rate. The ribbon growth runs made since the last reporting period are summarized in Appendix I; the dimensional characteristics of the ribbons are given in Appendix II. Several 50 mm wide ribbons are shown in Fig. 4.

Two die materials were found to be suitable for CAST growth. One is Ultracarbon UT-44 graphite (runs 70407-70412). The other is an impervious SiC-coated die using Ultracarbon UT-86 graphite as a substrate. A considerable number of runs were made to evaluate long term performance of one die made from this material (runs 70413-70604). Other process parameters addressed during this period were meniscus height, dopant distribution, and ribbon stresses.

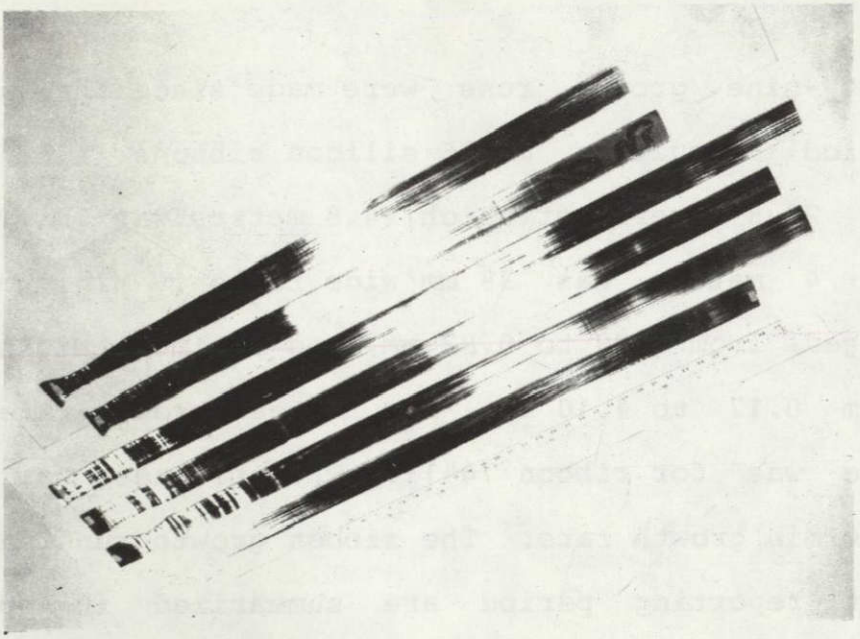

Fig. 4. Several 50 mm-wide CAST ribbons approximately 1 meter in length.

2.2 Evaluation of an SiC-coated Graphite Die

The primary objective of growth runs 70413 through 70604 was to monitor the performance of a single SiC-coated graphite die. The graphite grade was Ultracarbon UT-86, and the impervious SiC coating was applied by chemical vapor deposition. The die has been used for 24 growth attempts in 14 melt-down cycles and has produced 17 ribbons of total length 13.1 meters. The SiC particle density for individual consecutive ribbons and also the accumulative density (total SiC particles/total area grown) are summarized in Fig. 5. The accumulative SiC particle density was $1.3 \times 10^{-3}/cm^2$ after $2 \times 10^3 cm^2$ of ribbon had been pulled and rose to $9 \times 10^{-3}/cm^2$ after $4.5 \times 10^3 cm^2$ of ribbon had been grown from the die. After $6.5 \times 10^3 cm^2$ of growth, the accumulative particle density was $1.6 \times 10^{-2}/cm^2$. The rise in accumulative particle density is largely due to two ribbons which had abnormally high densities of $7.1 \times 10^{-2}/cm^2$ and $1.3 \times 10^{-1}/cm^2$. One of these (70601) occurred during a run in which the graphite heat shields were replaced.

Discounting the two high density ribbons, the accumulative SiC particle density was $3.7 \times 10^{-3}/cm^2$. Another way of expressing this result is that, on the average, one particle occurred after each 0.54 meter of growth.

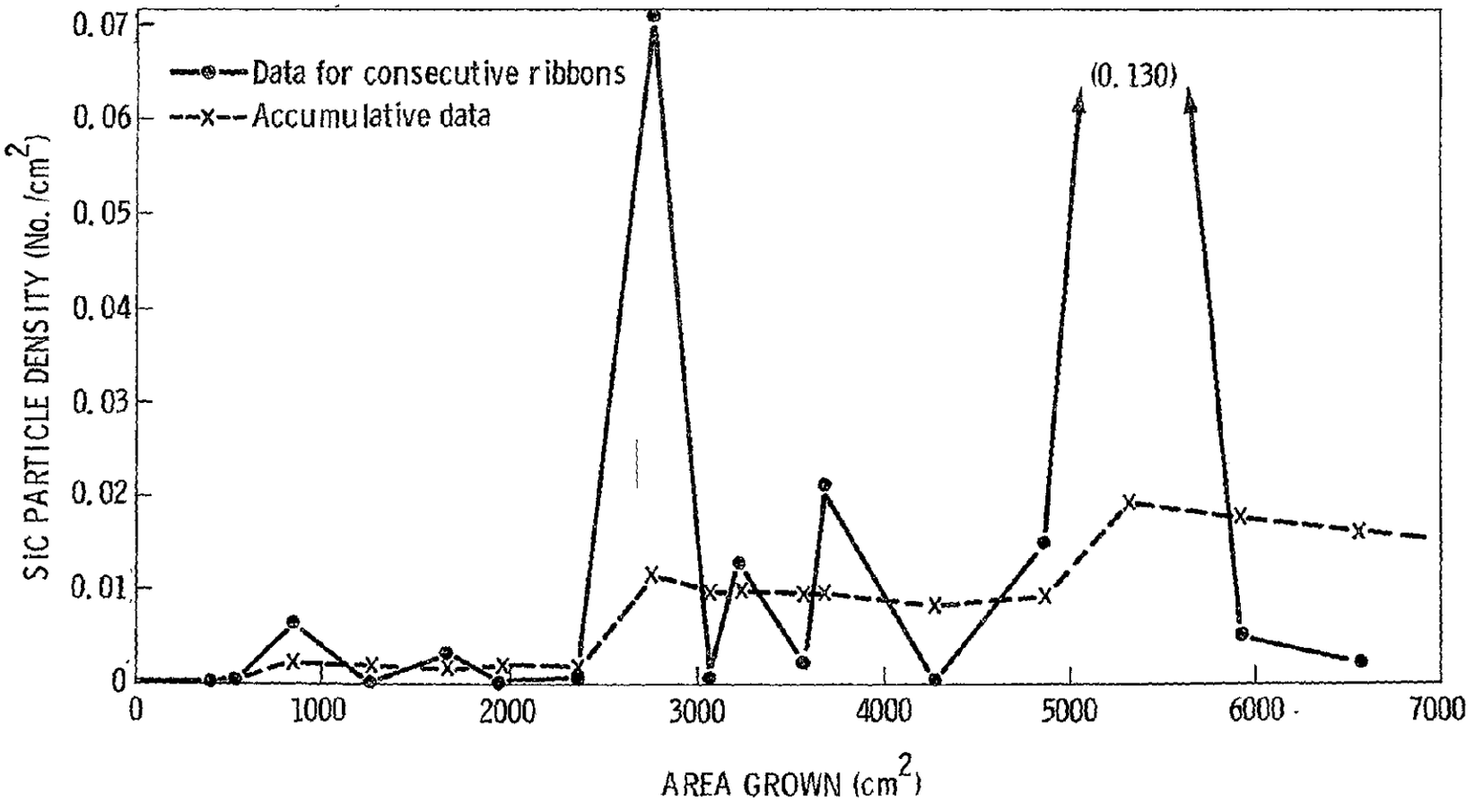

Fig. 5. Silicon carbide particle densities for 17 ribbons grown from a single SiC-coated graphite die.

ERRATA

Quarterly Technical Progress Report Number 8
July 1, 1977

Another example is shown in Fig. 9, where during the first day of operation (Monday) the equipment remains idle for 4.3 hours, or 26.6% of the workday. In a more flexible production environment, 3.4 hours of overtime (2.5 + 5.2 - 4.3) would have resulted in a second crystal for the day. This problem does not happen to occur with the FZ case (Figs. 8, 10, and 12), since the conditions (technology parameters) are such that two crystal starts per day can be readily scheduled.

A statistical break-down of the die's performance is given in Table I.

TABLE I. Statistical Break-down of SiC Particle Pick-up with SiC-coated Die.

Range of total SiC particle Count	No. of ribbons with particles in the range	Area of ribbons with particles in the range	Percentage of Total area grown
0-60	17	6575	100
0-30	16	6120	93
0-10	15	5740	87
0- 2	13	4535	69
0	7	2570	39

SiC particle densities of $< 3 \times 10^{-2}/cm^2$ are not unusual in the CAST growth configuration with graphite dies, and upon occasion a ribbon is grown with no particles -- particularly when a very high melt meniscus is maintained. However, the large number of ribbons with zero or ≤ 2 particles seen with the SiC-coated die has not been encountered before with graphite dies. The difference in particle pick-up between graphite and SiC-coated graphite dies is not thought to be related to a difference in solubility. The dissolution[5] and solid contamination[2] characteristics of SiC and C in silicon have been shown to be similar. The difference may

be due to the nature of the nucleation sites for crystallization of excess SiC from the carbon-saturated liquid silicon at the SiC die top. If the SiC die material promotes better adherence of SiC grown from solution than does graphite, then less free particulate SiC would be available in the meniscus region for incorporation in the growing ribbon. This concept has neither been verified nor disproved, as yet.

2.3 Meniscus Height Measurements

A technique was established for meniscus height measurement. The meniscus is photographed at a known viewing angle, θ, relative to the horizontal plane. For example, the meniscus of Fig. 6 was photographed at an angle of $52\text{-}1/2^{o}$. The distance from the seed to the solid-liquid interface at the time of the photograph is noted. Then, after growth, the ribbon thickness, t_r, at the location photographed is measured. The die-top thickness, t_d, is measured prior to the growth run. The apparent meniscus height, m, is obtained from a densitometer scan of the photographic negative (Fig. 7) using a Joyce, Loebl and Co. Ltd. double-beam recording microdensitometer model MK III CS. Once m, θ, t_r, and t_d are known, the meniscus height, h_m, can be obtained graphically as shown in Fig. 8. In this

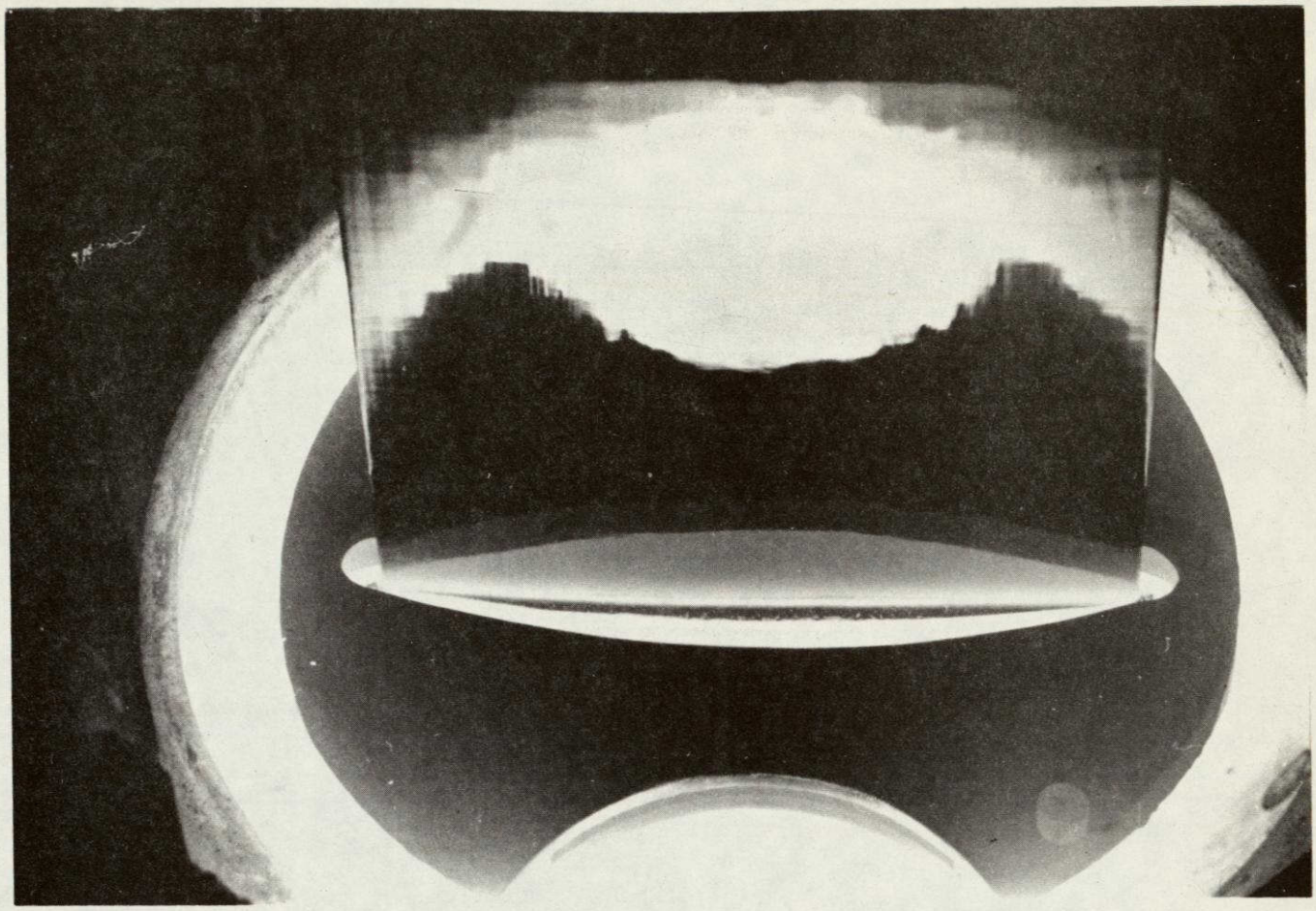

Fig. 6. Meniscus photograph of ribbon 70410: width, 50 mm; speed, 19 mm/min.

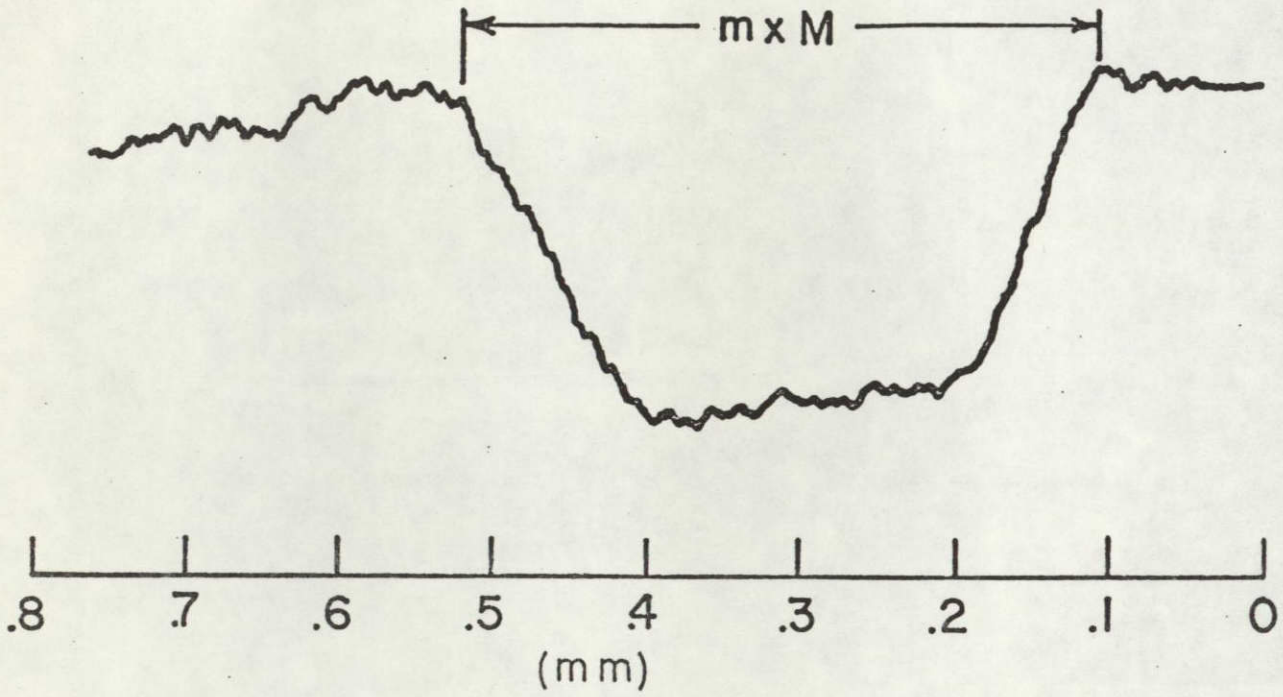

Fig. 7. Densitometer scan of meniscus region on photographic negative. The apparent meniscus height m is obtained after dividing the scan distance across the meniscus by the magnification of the negative M (usually about 0.4).

analysis, it is assumed that the ribbon grows at the geometrical center of the die-top as shown in Fig. 8. While a number of menisci have been photographed, analysis has been completed on only a few. One series of measurements was made with a 50-mm-wide die having a 2.01 mm central thickness t_d, a 0.41 mm slot dimension t_s, a 0.84 mm edge thickness, and a 1.73 mm deviation from flatness of the die top (δ in Fig. 2). The meniscus height h_m was found to increase from .53 mm to 0.75 mm as the central ribbon thickness decreased from .42 to .23 mm.

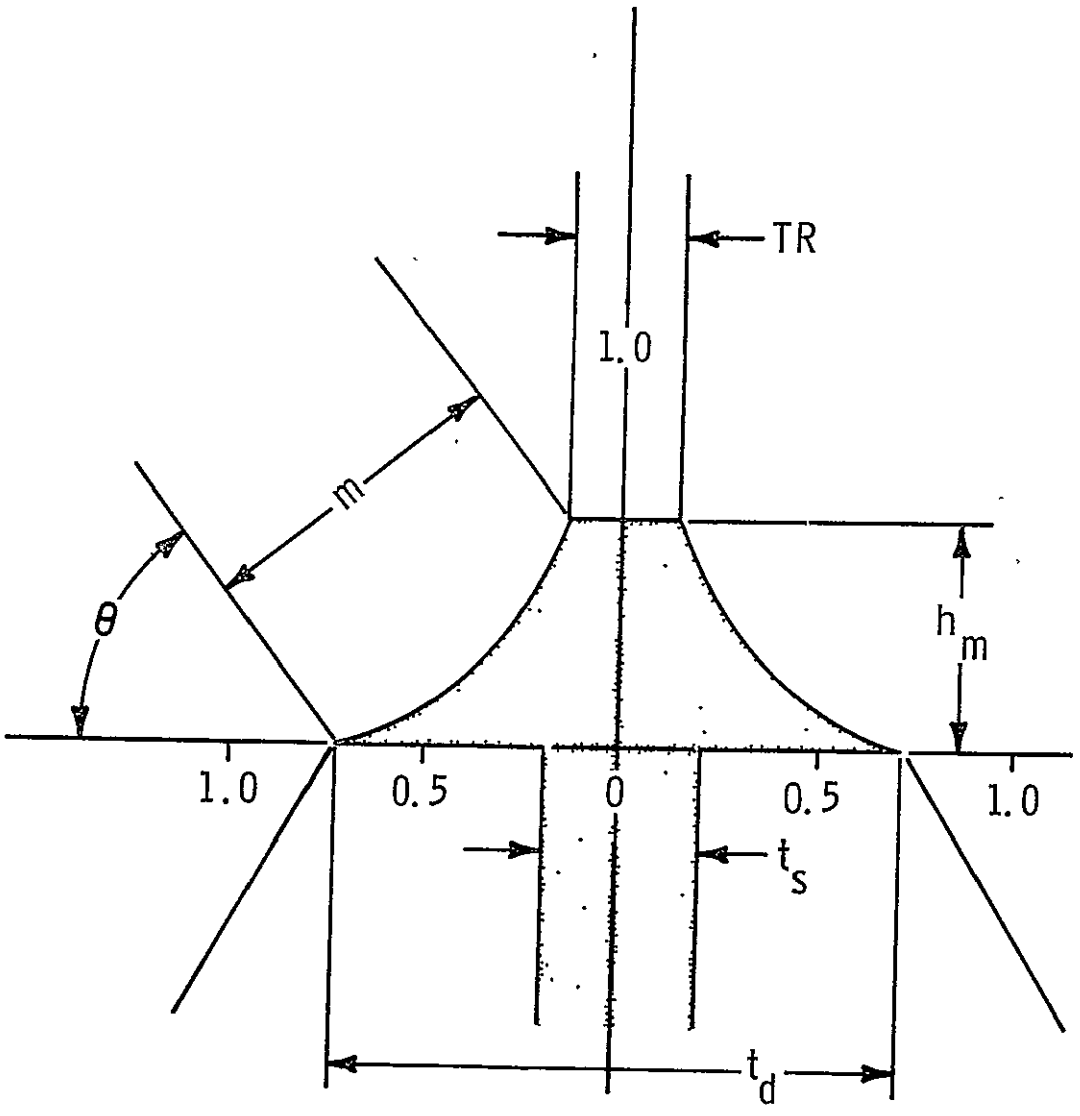

Fig. 8. Meniscus configuration in CAST ribbons.

At h_m = 0.75 mm, the ribbon is considered to be growing in the high meniscus mode of the capillary action shaping technique. The meniscus cross-sections for the two values of h_m are shown in Fig. 9. This Figure, along with Fig. 10, which is drawn from the data of reference 6, gives a comprehensive view of the growth geometry for the high melt meniscus mode of the Capillary Action Shaping Technique. For comparison, in the EFG growth technique the meniscus height is 9.06 mils (0.23 mm) for a 9.5 mil (0.24 mm) thick ribbon[7]. The factor of 3 increase in meniscus heights is a key advantage in obtaining smooth, low SiC particle density ribbons by the CAST method.

2.4 Dopant Distribution in 50 mm Ribbons

In our 6th Quarterly Progress report, a study of spreading resistance on silicon ribbons grown from various die configurations was made[8]. It was shown that open-channel dies (2-piece design) produce the most uniform transverse ribbon dopant distribution in 38 mm wide ribbons although a band of higher dopant concentration still tended to be present (Fig. 8 of ref. 8). We have done similar measurements on a 50 mm ribbon grown from a 2-piece die and still find an enhanced dopant region in the near-central area of the ribbon (Fig. 11). The transverse measurements were made on a lapped, 4.67° bevel surface extending across

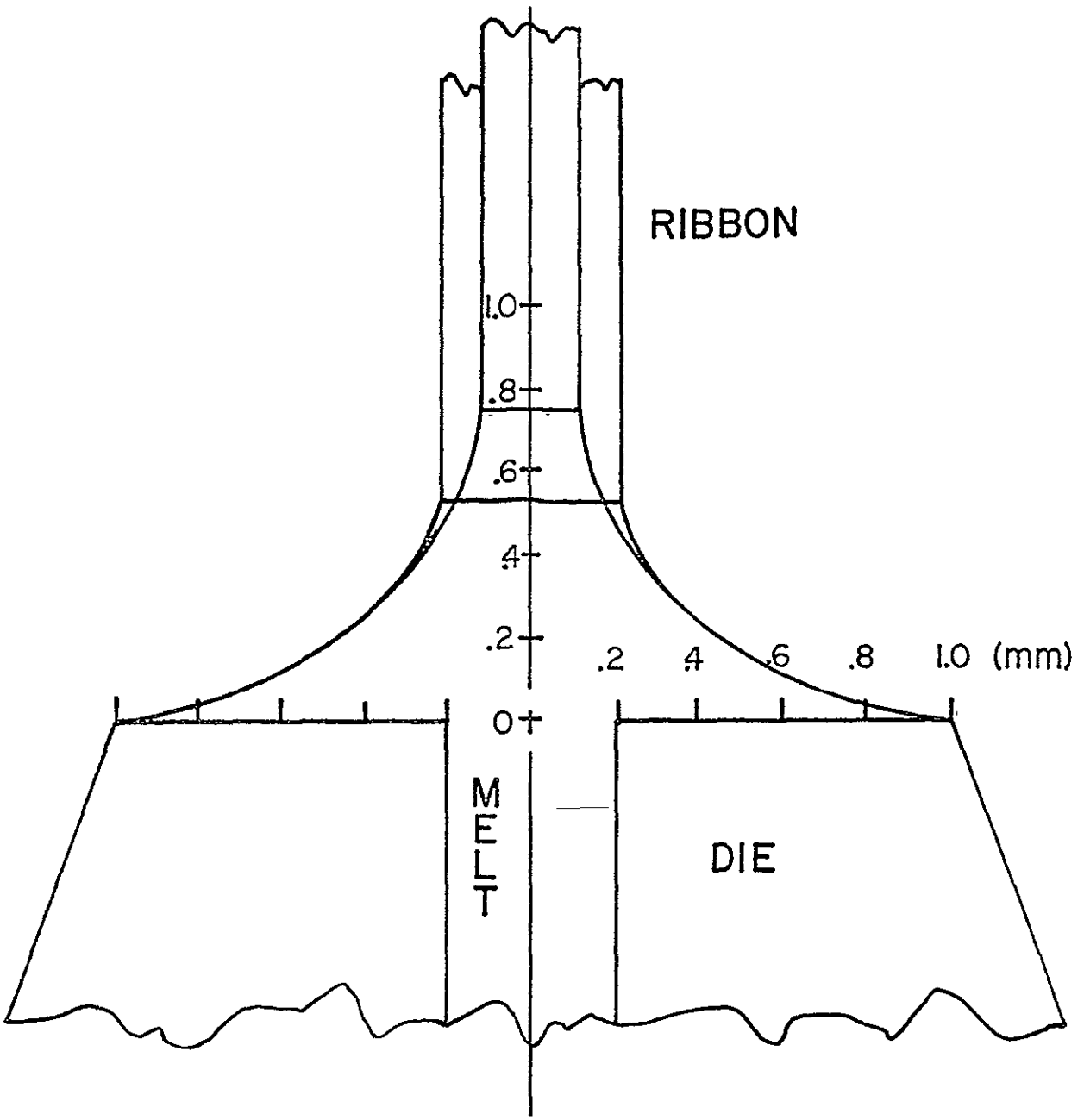

Fig. 9. Meniscus cross section for two values of ribbon thickness, using a 2 mm central die, top thickness. At 0.75 mm meniscus height, the ribbon is considered to be growing in the high meniscus mode.

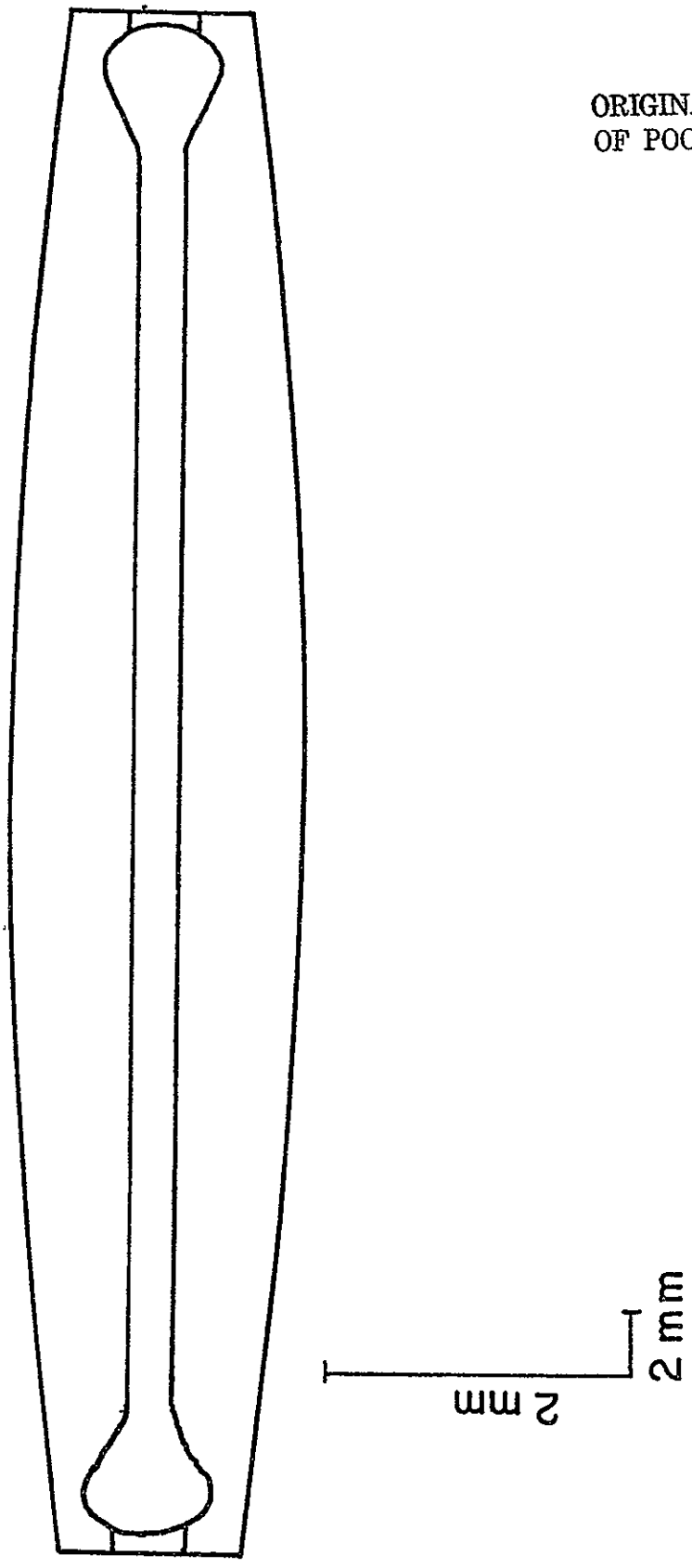

Fig. 10. Top sectional view, drawn to scale, of the die top and the silicon ribbon during capillary action shaping technique growth in the high melt meniscus mode.

the width of the ribbon. The variation of spreading resistance with depth into the ribbon was checked by making measurements down the bevel both near a high resistivity region (point A of Fig. 11) and a low resistivity region (point B). In both cases, excellent uniformity was observed in the thickness dimension (Figures 12 and 13).

2.5 Ribbon Stresses

Since breakage of ribbons during sawing has been a problem, a few runs were made with thermal modifiers near the ribbon edges to see if residual stress levels could be lowered (runs 70506-70510). Stress levels were determined by splitting the ribbons at the tail-ends and measuring the split width, s, as a function of distance, L, from the tip of the wedge-shaped crack or split opening. This was also done for several thin older ribbons not grown with thermal modifiers. Stresses were calculated in two ways. One method, suggested by M. Leipold[9], is to use the expression

$$\sigma = \frac{W Y s}{4L^2}, \qquad (1)$$

where σ is the stress in dynes/cm^2, W is the ribbon width, and Y is Young's modulus [1.9 x 10^{12} dynes/cm^2 for (111) silicon]. Generally, maximal values of L were used. The

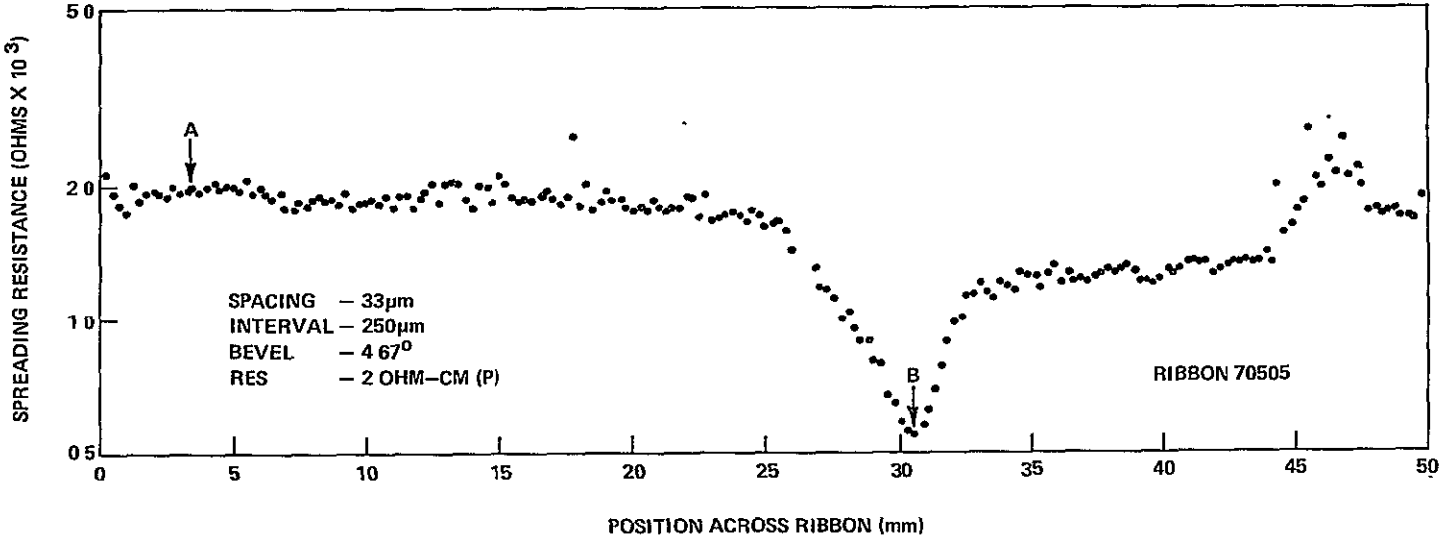

Fig. 11. Spreading resistance measurements on a 50 mm-wide ribbon grown from a two-piece die.

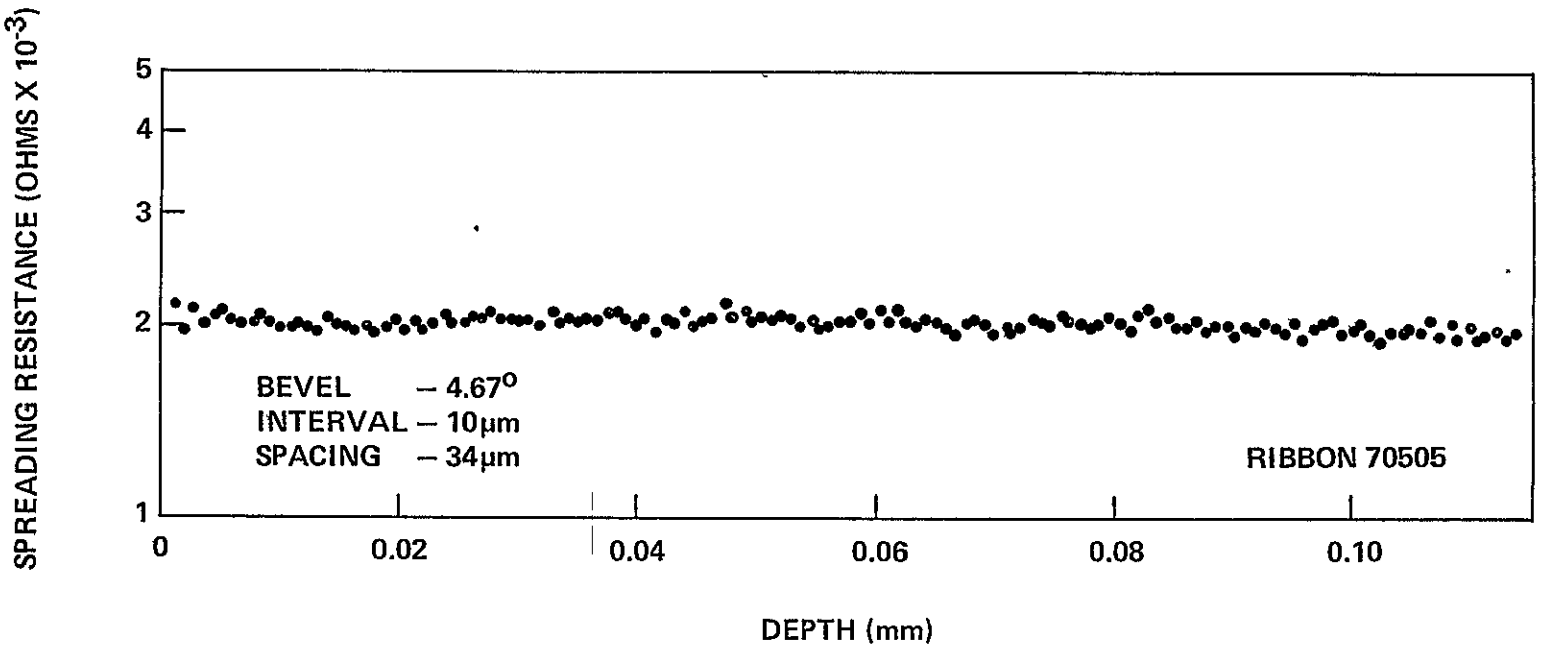

Fig. 12. Spreading resistance as a function of depth into ribbon, measured on bevel. Location of measurements corresponds to Point A on Fig. 11.

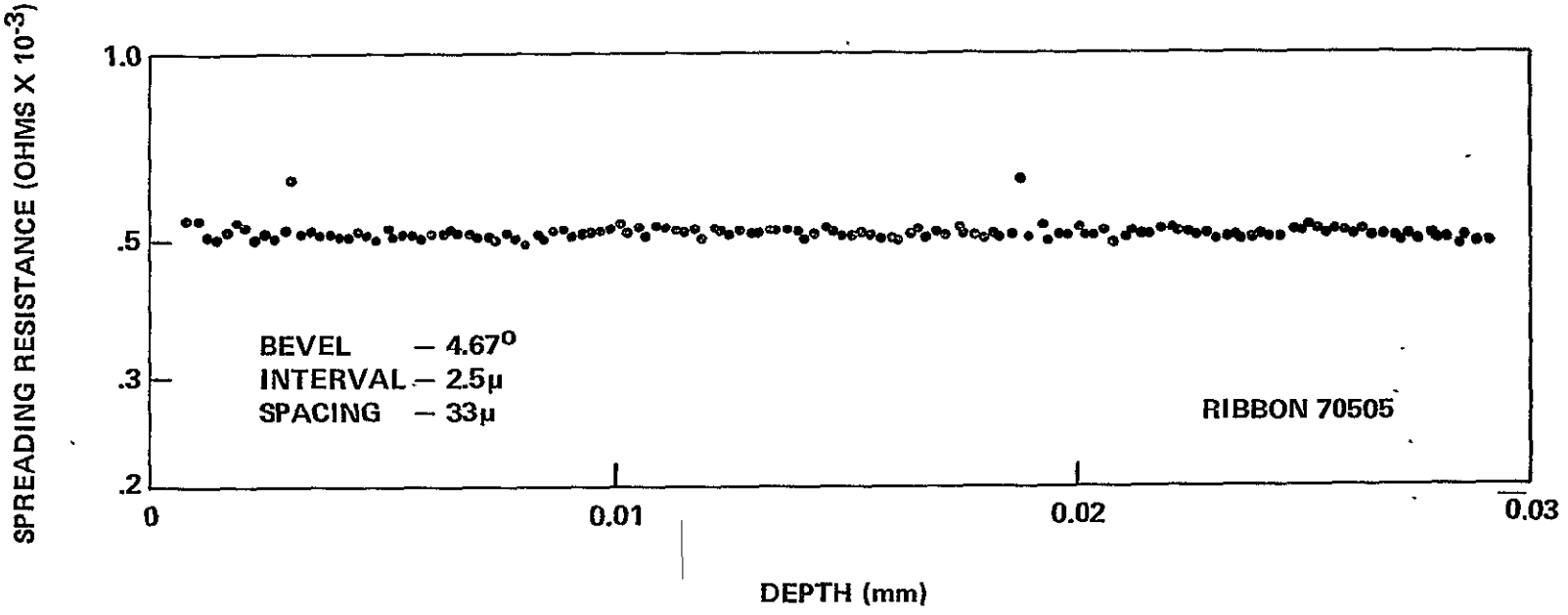

Fig. 13. Spreading resistance as a function of depth into ribbon, measured on bevel. Location of measurements corresponds to Point B on Fig. 11.

second method was to find the seven coefficients for a sixth-order polynomial least-squares fit for s vs L. The first and second derivatives ds/dL and d^2s/dL^2 were then evaluated, and the stress was calculated, as an average, over all values of L of the expression

$$\sigma = \frac{WY \quad d^2s/dL^2}{4\ [1 + (ds/dL)^2]^{3/2}} \qquad (2)$$

as proposed by Hurley and Pollock[10]. The second method is very sensitive to the accuracy of the s-vs-L measurements and to the shape of the least-squares-fit curve and gives generally larger and less consistent values. The results obtained are given in Table II.

TABLE II. Stress Values in Silicon Ribbons

Ribbon No.	$\frac{W\ Y\ s}{4L^2}$ (dynes/cm^2)	$\frac{WY\ d^2s/dL^2}{4\ [1 + (ds/dL)^2]^{3/2}}$ (dynes/cm^2)	W (cm)	Minimum Thickness (mm)	Growth Speed (mm/min
70308	2.7×10^8	5×10^8	4.95	.14	23
70417	3.7×10^8	6×10^8	4.95	.09	20
70508	4.8×10^8	---	4.4	.95	16
70509	3.5×10^8	7×10^8	4.7	.50	16

The ribbons grown with the thermal modifier (70508 and 70509) could not be brought to full width (hence they are

thicker because of the CAST growth geometry). Their stress levels were no lower than those of the normally grown ribbons. All stress levels measured were moderate and of comparable magnitude to those seen in 25- and 38-mm growth.

Even though measured stress levels in 50-mm-wide ribbons are only moderate, considerable breakage occurs when they are sawed into sections. A technique developed by F. Newman has reduced the saw breakage. The ribbon is intimately waxed to a lava substrate which has previously been waxed (with a higher-temperature wax) to an aluminum support bar. The bar can be mounted in a vise on a Micro-Mech diamond sawing machine. A 7.6-cm-diameter x 0.19-mm-thick blade is used at 450 RPM and at a lateral travel rate of 3 cm/min. The key to reducing breakage appears to lie in not cutting through the entire ribbon thickness in a single pass. Rather, the cut is made in several passes with a 0.25-mm increase in depth per pass.

3.0 100-mm System Design

Design of a 100-mm growth system has been completed, and all parts have been submitted for fabrication. An assembly drawing is shown in Fig. 14.

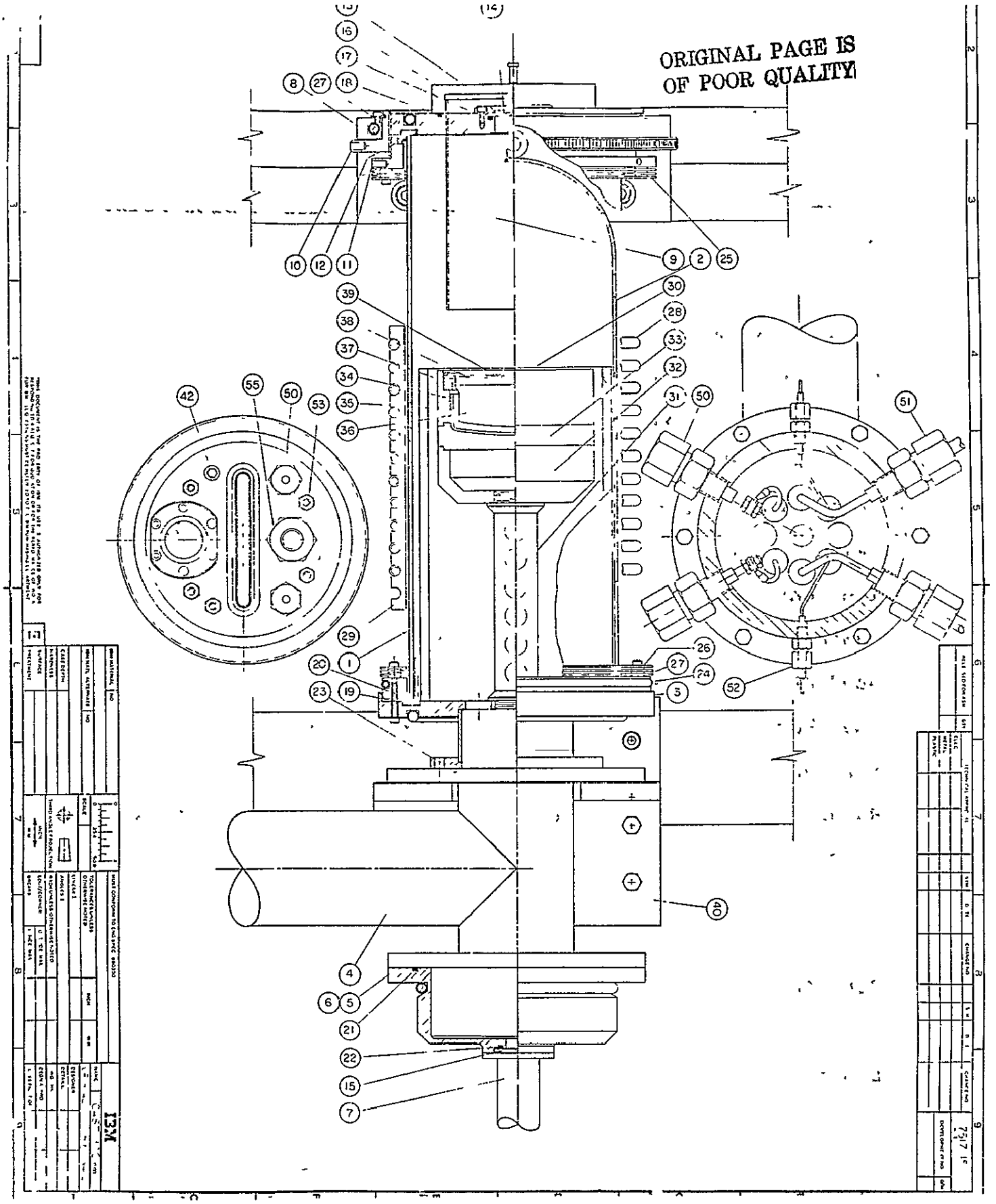

Fig. 14. Assembly drawing of 100-mm CAST ribbon growth system.

The chamber is designed to fit the hydraulic puller currently being used for 50-mm growth and will utilize the same vacuum system. The design consists of a clear uncooled quartz chamber fitted with cooled metal endplates. RF heating with an exterior coil will be used although provisions are made for an interior smaller coil if necessary. The hot-zone and pulling port will accommodate a 100-mm maximum width. Numerous inert-gas, electrical, and sensor feed-throughs are provided for versatility.

The sizing of the hot-zone components is as follows:

ITEM	Max O.D. (mm)	Min I.D. (mm)
Crucible	113	108
Susceptor	138	115
Insulation	170	145
Furnace Shell	193	181

The crucible capacity is 500 grams.

4.0 ACKNOWLEDGMENT

Technical assistance in ribbon growth experiments was provided by F. Newman, who also worked on ribbon sawing techniques. E. F. Gorey performed the spreading resistance measurements.

5.0 REFERENCES

1. H. E. LaBelle, Jr., Mater. Res. Bull. 6, 581 (1971).

2. T. F. Ciszek, Mater. Res. Bull. 7, 731 (1972).

3. T. F. Ciszek and G. H. Schwuttke, Phys. Status Solidi (a) 27, 231 (1975).

4. J. C. Swartz, T. Surek, and B. Chalmers, J. Electron. Mater. 4, 255 (1975).

5. R.I. Scace and G. A. Slack, The Si-C and Ge-C Phase Diagrams. Proceedings of the Conference on Silicon Carbide, Boston, April 1959. Pergamon Press, New York (1960).

6. G. H. Schwuttke, T. F. Ciszek, and A. Kran, "Silicon Ribbon Growth by a Capillary Action Shaping Technique", Quarterly Technical Progress Report, Number 7, ERDA/JPL 954144 April 1, 1977, p. 6.

7. A. D. Morrison, K. V. Ravi, C.V. Hari Rao, T. Surek, D. F. Bliss, L. C. Garone, and R. W. Hogencamp, "Large Area Silicon Sheet by EFG", Annual Progress Report, ERDA/JPL 954355, Sept. 15, 1976.

8. G. H. Schwuttke, T. F. Ciszek, and A. Kran, "Silicon Ribbon Growth by a Capillary Action Shaping Technique", Quarterly Technical Progress Report Number 6, ERDA/JPL 954144 Dec. 15, 1976, pp 4-11.

9. M. Leipold, private communication.

10. G. F. Hurley and J. T. A. Pollock, Metallurgical Transactions 3, 397 (1972).

Appendix I: Ribbon Growth Experiments Performed During the Current Reporting Period

Run No.	Die Width (mm)	Die Material	Experimental Variables	Results
70302	50	DFP-2	Repeat of 70301 conditions.	None
70303	50	DFP-2	Installed new quartz insulator tube. Adjusted right argon flow balancing tube.	Froze, unable to maintain full-width growth.
70304	50	DFP-2	Repeat.	Silicon splashed on die and ruined it.
70305	38	DFP-3-2	Standard growth conditions, to produce ribbons for cutting experiments.	114-cm ribbon.
70306	50	DFP-3-2	Photographic recording of meniscus heights, at speeds of 1.5-3.2 cm/min. New die.	Good ribbon. Meniscus heights under evaluation. Susceptor broke on cool-down. Photos not sharp.
70307	50	DFP-3-2	As above, except constant pull speeds of 1.9 cm/min, while varying temperature and argon flows.	92-cm-long ribbon. Meniscus heights under evaluation. Photos not sharp.
70308	50	DFP-3-2	Meniscus heights photographed at constant temperature, but varying argon flows and pull speed. Also to measure ribbon stress.	Five photos made. Ribbon is 120 cm long, 0.14-0.19 mm thick in central region. Stress calculated to be 3×10^8 dynes/cm^2 by measuring split widths. Photos not sharp.

Run No.	Die Width (mm)	Die Material	Experimental Variables	Results
70309	38	DFP-3-2	Standard conditions, to grow ribbon for cutting experiments. Also increased argon flow from furnace bottom to avoid fogging of quartz furnace tube.	90 cm x .55 mm thick ribbon grown. No change in fogging.
70310	38	DFP-3-2	Standard conditions, to grow ribbons for cutting experiments.	114 cm x .4 mm x 38 mm wide ribbon.
70311	50	DFP-3-2	New die 2PA-502.	None. Die not seated in holder. Flooded.
70312	50	DFP-3-2	2P501 die (new). Photograph of meniscus directly (no water filter).	Photos of meniscus much sharper without water filter. Good looking ribbon.
70313	50	Ultra-carbon UT-44	New die. New graphite material. Design 2PA501.	Two short pieces of ribbon grown, but froze out. Die ruined.
70314	38	DFP-3-2	Standard process to grow ribbon for cutting experiments.	78-cm-long ribbon grown.
70401	50	DFP-3-2	Evaluate thicker die top (1.3-mm edges, 2-mm center). 20-mm/min growth speed.	27-cm ribbon. Very rough. 0.95 mm thick at edges/.66 mm thick in center.
70402	50	DFP-3-2	Repeat.	110-cm-long ribbon grown, 0.39 mm thick in center.
70403	50	DFP-3-2	Repeat.	All growth attempts with this die have been easy to start.

Run No.	Die Width (mm)	Die Material	Experimental Variables	Results
70404	50	DFP-3-2	Repeat. Die was splayed from previous run. Argon flow directed at front of furnace tube to avoid oxide build-up.	Easy to start. 111-cm-long ribbon grown. Quartz tube stayed clear through run.
70405	50	DFP-3-2	Repeat. Splayed die closed again at growth temperature. Will pull crucible nearly empty for reuse.	Crucible OK for reuse.
70406	50	DFP-3-2	Reused crucible from previous run. Photograph meniscus with this 1.3-mm to 2-mm-thick die.	Five photos made. Will be analyzed. 64-cm-long ribbon grown.
70407	50	UT-44	Evaluate new die material and design. Die is 0.82 mm thick at edges and 1.99 mm thick in middle. Top has 1.7-mm deviation from flatness.	Meniscus photographed. Nice looking ribbon 35 cm long x 50.1 mm wide x .55 mm thick at edges (.28 mm in middle).
70408	50	UT-44	Repeat.	Temperature lowered too far. Ribbon froze.
70409	50	UT-44	Repeat, photograph meniscus at 20-mm/min growth speed.	80 cm x 50 mm x .50 mm thick ribbon. 3 photos made.
70410	50	UT-44	Repeat, more meniscus photographs.	Five photos made. 110 cm x 50 mm x .4 mm thick ribbon.

Run No.	Die Width (mm)	Die Material	Experimental Variables	Results
70411	50	UT-44	Repeat, to explore faster pull speeds.	Attained speed of 40 mm/min for a distance of 11 cm. Then froze. Dendritic surface morphology developed at fast speeds. Overall length is 104 cm. Thickness ranged from .30 to .15 mm (the latter at 40 mm/min).
70412	50	UT-44	Repeat, but at slow speed (18 mm/min) to see if dendritic surface morphology recurred.	No dendritic features. Ribbon is thicker (.48 mm) at slow speed.
70413	50	SiC/ Graphite	Evaluate SiC-coated graphite die. 20-mm/min growth speed.	Very smooth reflective ribbon. Zero SiC particle density. 82 cm x 50 mm ribbon. .85 mm thick at edges/.35 mm thick in center.
70414	50	SiC/ Graphite	Repeat at 26 mm/min.	Thinner ribbon (.65 edge/.27 center) 23 cm long. Again zero SiC density but ribbon has some morphological features in a thin central strip.
70415	50	SiC/ Graphite	Repeat.	Temperature lowered too far. Ribbon froze.
70416	50	SiC/ Graphite	Repeat, 20-mm/min speed.	62-cm-long ribbon. Thicker (.6-.70 in center). Two SiC particles on surface (density .006/cm^2). Same rough features present as in run 70414.

Run No.	Die Width (mm)	Die Material	Experimental Variables	Results
70417	50	SiC/ Graphite	Repeat, 20-mm/min speed photograph meniscus.	Very smooth, thin (.09-.15 mm in central region) ribbon. Zero SiC particle density. Similar appearance to run 70413.
70418	50	SiC/ Graphite	Repeat of above.	79-cm-long, smooth thin ribbon (.11-.18 mm in central region). One particle (.003/cm^2) on entire surface.
70501	50	SiC/ Graphite	Die material performance test. 18 mm/min growth speed.	60cm x 5cm x .32 to .70mm ribbon. Zero SiC density.
70502	50	SiC/ Graphite	Repeat.	Ribbon pulled out upon reaching full width. Seed broke.
70503	50	SiC/ Graphite	Repeat. New thick susceptor.	None. Could not seed.
70504	50	SiC/ Graphite	Repeat. Added argon flow directed at backside of ribbon. 20-25 mm/min growth speed.	82cm x 5cm x 0.30 to 0.68mm ribbon. Zero SiC particles. Backside of ribbon clean, but now front side has oxide power coating. Seed was loose and ribbon shifted laterally several times.
70505	50	SiC/ Graphite	Repeat, but no argon flow to ribbon back-side. 16 mm/min. growth speed.	76cm x 5cm x 0.37 to 1.00mm thick ribbon. 0.071 SiC particles per cm^2. Susceptor broke during unloading.
70506	50	SiC/ Graphite	Repeat. Heat shields placed at edges of ribbon. New susceptor.	Froze upon reaching full width.

Run No.	Die Width (mm)	Die Material	Experimental Variables	Results
70507	50	SiC/ Graphite	Repeat. 19 mm/min. growth speed. Meniscus photos made. 1.2cm x 2cm heat shields placed on susceptor rim near ribbon edges.	61cm x 5cm x .25 to .55mm ribbon. Zero SiC density
70508	50	SiC/ Graphite	Repeat, 16 mm/min. speed.	31cm x 4.4cm x .95 to 1.2 ribbon. 0.013 SiC partic cm^2. Stress level 4.8 x 1 dynes/cm^2.
70509	50	SiC/ Graphite	Repeat.	72cm x 4.7cm x .50 to 1.0 ribbon. Difficult to rea full width with shields. SiC density 0.002/cm^2.
70510	50	SiC/ Graphite	Repeat.	Froze at 19cm length. .0. SiC particles/cm^2. Width = 4.3cm^2.
70511	50	SiC/ Graphite	Repeat. Heat shields at edges removed. 25 mm/min speed.	120cm x 5cm x .16 to .62mm ribbon. Zero SiC density.
70512	50	SiC/ Graphite	Repeat.	Froze during seeding.
70513	50	SiC/ Graphite	Repeat. 18 mm/min. speed.	120cm x 5cm x .30 to .88mm ribbon. .015 SiC particle cm^2. Right side pulled out during seeding.
70514	50	SiC/ Graphite	Repeat.	Could not achieve proper seeding conditions.

Run No.	Die Width (mm)	Die Material	Experimental Variables	Results
70601	50	SiC/ Graphite	Replaced upper and lower shields. They had warped. Growth speed 16mm/min.	91cm x 5cm x .40 to .68mm ribbon. 0.13 SiC particles /cm^2. Rough surface.
70602	50	SiC/ Graphite	Repeat (continuing long-term evaluation of die first used in run 70413). 20 to 30mm/min growth speed.	121cm x 5cm x 0.18 to 0.63mm ribbon. 0.005 SiC particles /cm^2.
70603	50	SiC/ Graphite	Repeat @ 17mm/min growth speed. Took meniscus photos.	130cm x 5cm x 0.15 to 0.79mm thick ribbon. 0.002 SiC particles/cm^2.
70604	50	SiC/	Repeat (continuation)	Could not seed.

Appendix II. Dimensional Characteristics of Silicon Ribbons Grown Since Last Reporting Period

Ribbon Run No.	Seed Orientation Axis	Seed Orientation Surf	Usable Length (cm)	Width (mm) Max	Width (mm) Min	Thickness (mm) Seed Max	Thickness (mm) Seed Min	Thickness (mm) Tail Max	Thickness (mm) Tail Min
70305	110	100	114	37.4	37.1	.70	.36	.60	.28
70306	110	100	108	49.7	49.4	.73	.38	.64	.20
70307	110	100	92	49.5	49.2	.55	.36	.60	.35
70308	110	100	120	49.5	49.2	.50	.19	.48	.14
70309	110	100	90	37.6	37.1	.75	.55	.60	.52
70310	110	100	114	38.1	37.9	.62	.42	.92	.33
70312	110	100	85	49.2	48.8	.78	.25	1.08	.40
70314	110	100	78	37.6	36.5	.82	.60	.56	.45
70401	110	100	27	49.1	48.2	.85	.75	1.02	.58
70402	110	100	110	50.2	49.1	.65	.45	1.00	.33
70403	110	100	18	48.7	47.2	.90	.82	.95	.72
70404	110	100	111	49.7	48.6	.60	.70	.64	.38
70405	110	100	51	49.0	48.5	.95	.82	.90	.70
70406	110	100	64	49.3	48.7	.92	.73	.42	.32
70407	110	100	35	50.5	50.1	.50	.28	.60	.28
70409	110	100	80	50.4	47.4	.52	.40	.70	.50
70410	110	100	110	50.5	49.7	.61	.40	.52	.42
70411	110	100	104	50.5	49.7	.21	.15	.17	.15
70412	110	100	50	49.8	49.6	.65	.45	.52	.48
70413	110	100	82	50.1	48.6	.80	.37	.92	.32
70414	110	100	23	49.3	47.6	.65	.35	.64	.27
70416	110	100	62	49.4	46.9	.92	.75	.92	.57
70417	110	100	86	49.5	49.4	.36	.15	.60	.09
70418	110	100	79	49.4	47.0	.56	.11	.42	.18
70501	110	100	60	49.6	49.2	.52	.35	.70	.32
70504	110	100	82	49.4	45.4	.68	.31	.65	.30
70505	110	100	76	49.9	46.7	.84	.43	1.00	.37
70507	110	100	61	49.5	47.4	.55	.42	.37	.25
70508	110	100	31	44.6	43.9	1.10	.95	1.20	.95
70509	110	100	72	47.7	47.0	.96	.72	1.04	.50
70510	110	100	19	42.8	42.1	.70	.50	.95	.72
70511	110	100	120	49.9	49.4	.60	.25	.62	.16
70513	110	100	120	49.8	49.2	.88	.42	.84	.30
70601	110	100	91	50.5	50.3	.60	.40	.68	.42
70602	110	100	121	50.1	49.8	.63	.40	.60	.18
70603	110	100	130	50.1	49.6	.60	.22	.79	.15

STRUCTURAL AND ELECTRICAL CHARACTERIZATION OF SILICON RIBBONS

by

K. Yang and G. H. Schwuttke

1. INTRODUCTION

Silicon ribbons grown by the capillary action shaping technique have a unique defect structure. Typical for ribbons grown under steady state conditions are various amounts of linear and planar defects. Such defects influence solar cell efficiency to different degrees[1]. Previously it was shown that the total defect density in a ribbon section is not representative of its solar cell efficiency[1]. Thus, it was concluded that the electrical activity of crystal defects in CAST ribbons can vary significantly[1].

This report describes a study primarily concerned with the identification of electrically active crystal defects in CAST ribbons. First, the electrically active defects are identified through EBIC contrast in the scanning electron microscope[1,2]. Subsequently, the crystallographic structure of a specific defect is analyzed through

transmission electron microscopy. Finally, its influence on minority carrier lifetime is determined through MOS C-t measurements.

2. MEASUREMENTS

Based on electrical measurements and preliminary structural investigations, ribbon quality can be classified into four categories. This classification is shown in Table I.

TABLE I. Classification of Ribbon Quality

Class	Lifetime Range (μsec)	Solar Cell Efficiency* (%)	Dominant Defects
I	1 to 10	5 to 8	First order (coherent) twins, stacking faults, dislocations below $10^4/cm^2$.
II	0.01 to 1	3 to 5	Higher order twins, multiple stacking faults, low-angle grain boundaries, dislocations above $10^4/cm^2$.
III	< 0.01	1 to 3	Grain boundaries, dislocations above $10^6/cm^2$.
IV	Not Measurable	--	Siliconcarbide dendrites on surface.
STANDARD CZ	10-500	8 to 12	None

*Measured without anti-reflection coating

Accordingly, the different ribbon quality groups are related to certain lifetime and solar cell efficiency ranges. Although this classification, was originally conceived phenomelogically, experience has shown that it presents a good guideline to solar cell efficiency obtainable from ribbon sections of certain perfection. The following investigations have produced results in support of this original classification.

2.1 EXPERIMENTAL

Examples of ribbon sections representing the different quality groups listed in Table I are shown in Fig. 1. MOS capacitors were fabricated on such ribbon sections, 24 mm x 60 mm, or 50 mm x 60 mm in size. Normally, 36 capacitors of 1.5 mm diameter were placed on a section. In some cases, high density masks with 400 capacitors were used. The two masks are shown in Fig. 2. Subsequently, generation lifetime of each capacitor was measured using the MOS C-t technique. After the lifetime measurements, the EBIC image of the MOS capacitor was obtained in the SEM, as described in reference 2. Thus, the subsurface defect structure in the silicon was displayed and qualitative information about the electrical activity of the crystal defects under the MOS dot was obtained. After the SEM investigation, the Al MOS

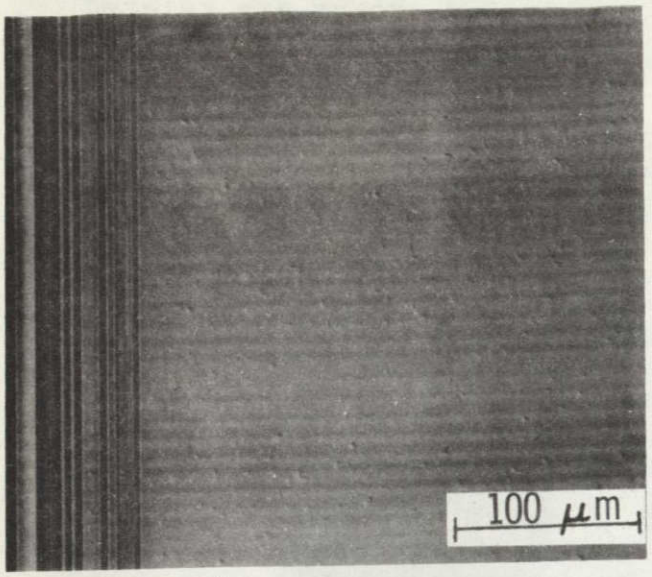

a. Perfect crystal
Lifetime: 825 μ sec

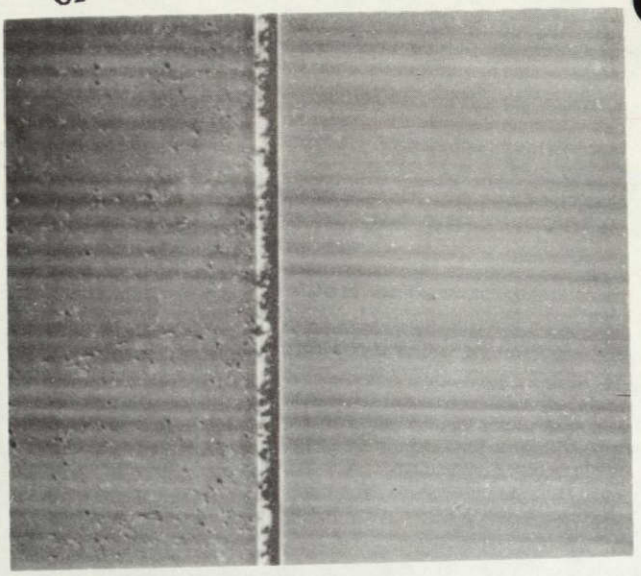

b. Dislocations in boundary and in left crystal section
Lifetime: 1.5 μ sec

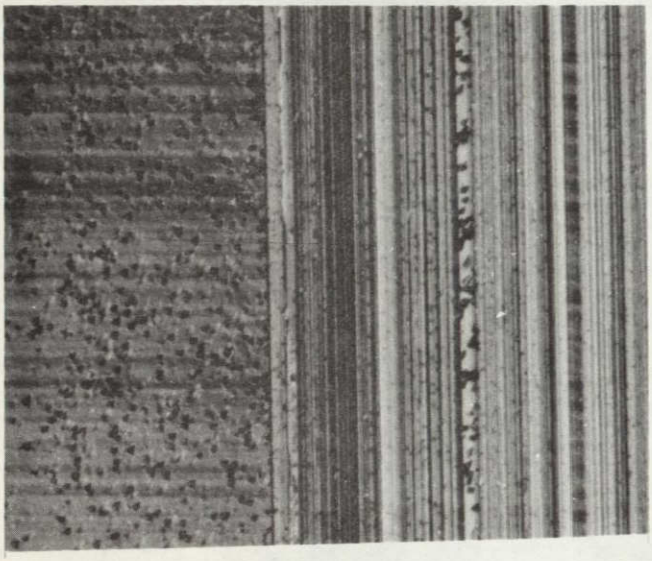

c. Dislocations and active boundaries
Lifetime: 0.145 μ sec

d. Dislocations and low-angle boundary
Lifetime: 0.02 μ sec

Fig. 1. Defect pattern and lifetime distribution.

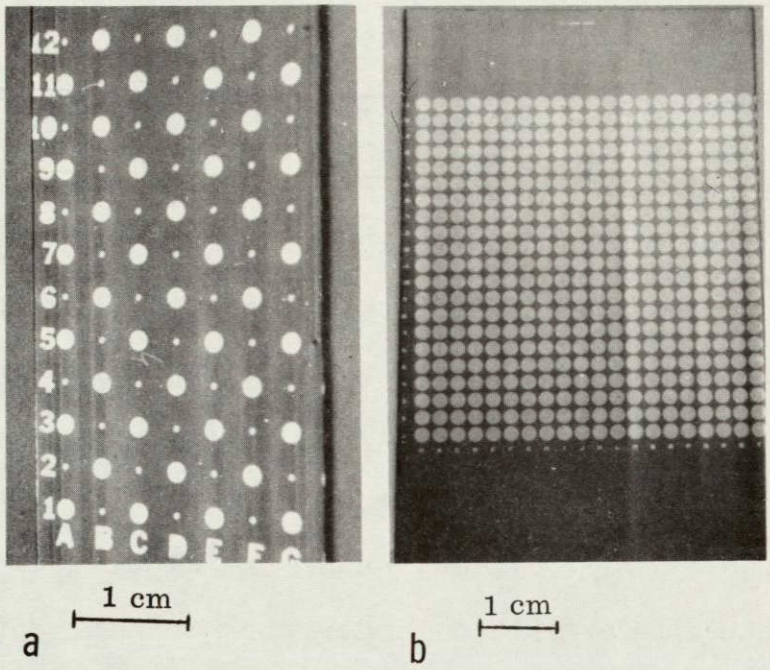

Fig. 2. (a) Low density and (b) high density MOS capacitor mask as used for the evaluation of lifetime for silicon ribbons. Dot size for both (a) and (b) is 1.5 mm.

dots and the SiO_2 were stripped of the ribbon surface and some MOS areas were Sirtl etched to reveal the crystal defects under the MOS dot in the optical microscope. A comparison of EBIC picture and optical picture allowed one to differentiate between the electrically active and the non-active defects. However, most of the MOS capacitors were punched out after stripping Al and SiO_2 as 2 mm disks (not Sirtl etched) and processed for TEM investigations. Before TEM investigations, the corresponding EBIC image of the MOS capacitor was studied. Details were obtained about the defect state in the silicon under the MOS dot as well as information was obtained about the electrical activity of the defects in the silicon under the MOS dot. Subsequently, the defects were analyzed in the TEM. A good correlation between defect state, type of defect, its influence on generation lifetime, and its electrical activity was thus possible.

2.2 RESULTS

2.2.1 DEFECTS IN CLASS I RIBBONS

The most obvious defects encountered under steady state growth conditions are linear boundaries which are visible in the ribbon surface even prior to etching. These boundaries

tend to grow parallel to the ribbon edges. While the majority of these boundaries are twins or stacking faults, some of them are multiple stacking faults or low angle grain boundaries. The electrical activity of these boundaries depends on their crystallographic nature and can vary significantly. This is illustrated in Figs. 3. The EBIC picture of Fig. 3a shows that most of the linear, parallel boundaries displayed in the optical micrograph of Fig. 3b are electrically nonactive except those at positions indicated by F and L. The activity is moderate for boundaries at F but is strong for boundaries at position L.

Figure 3c is an optical micrograph of area A indicated in Fig. 3b at higher magnification and shows that the nonactive boundaries are free of dislocation etch pits. TEM micrographs of this type of boundary are shown in Figs. 4a and 4b for ribbons of [011] and [211] surface orientation, respectively. These two surface orientations, especially the [011] are preferred orientations under steady state growth conditions. Twinning occurs in the (111) plane perpendicular to the [011] surface but inclined to the [211] surface. Using TEM image characteristics associated with twin boundaries and stacking faults the boundaries in Figs. 4a and 4b are analyzed as first order (coherent) twin boundaries and stacking faults[3]. Dislocations in or

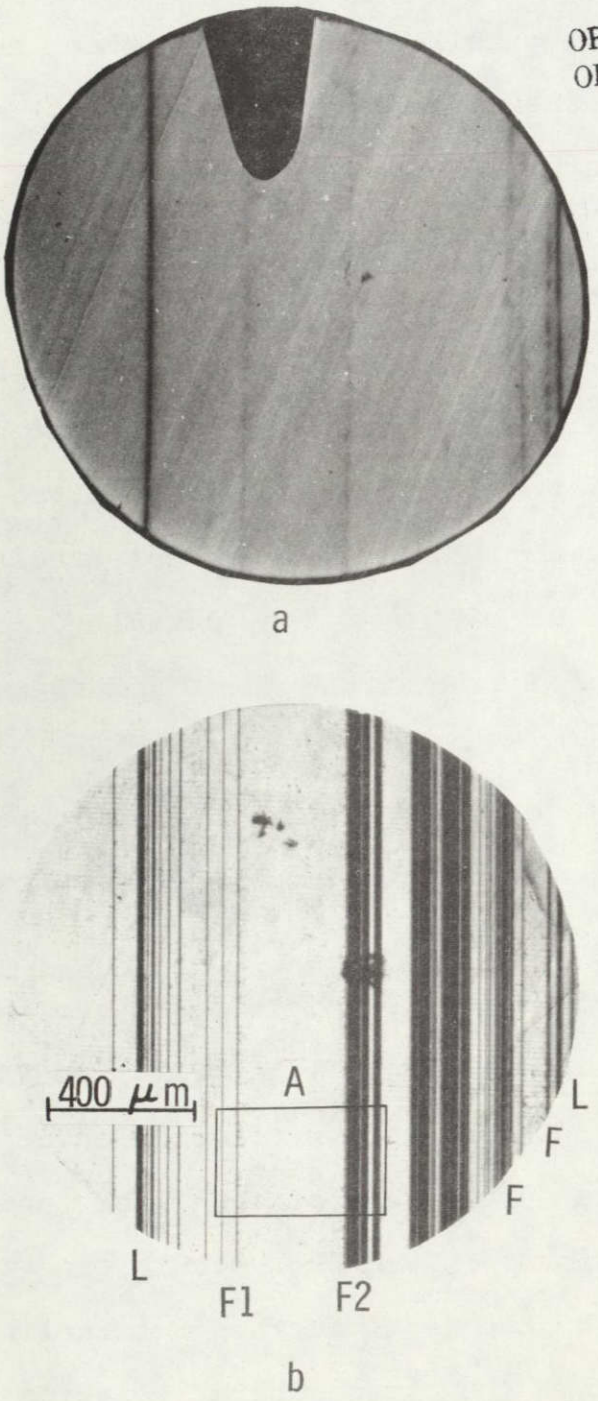

Fig. 3. (a) EBIC micrograph showing that most of the linear, parallel boundaries displaced in the optical micrograph of (b) are electrically nonactive except for those at the position indicated by F and L.

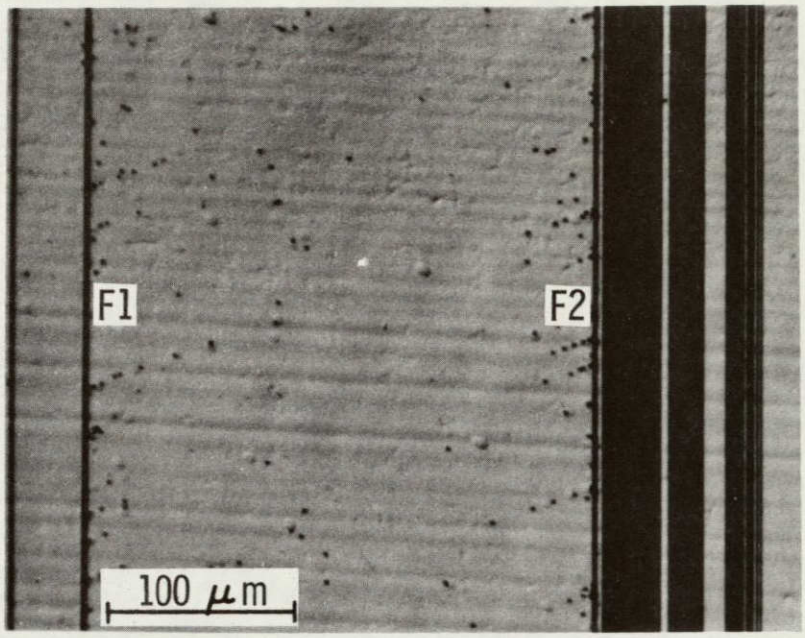

C

Fig. 3. (c) Area A of Fig. 3b at higher magnification. The nonactive boundaries are free of dislocation etch pits. Pits are observed along F1 and F2.

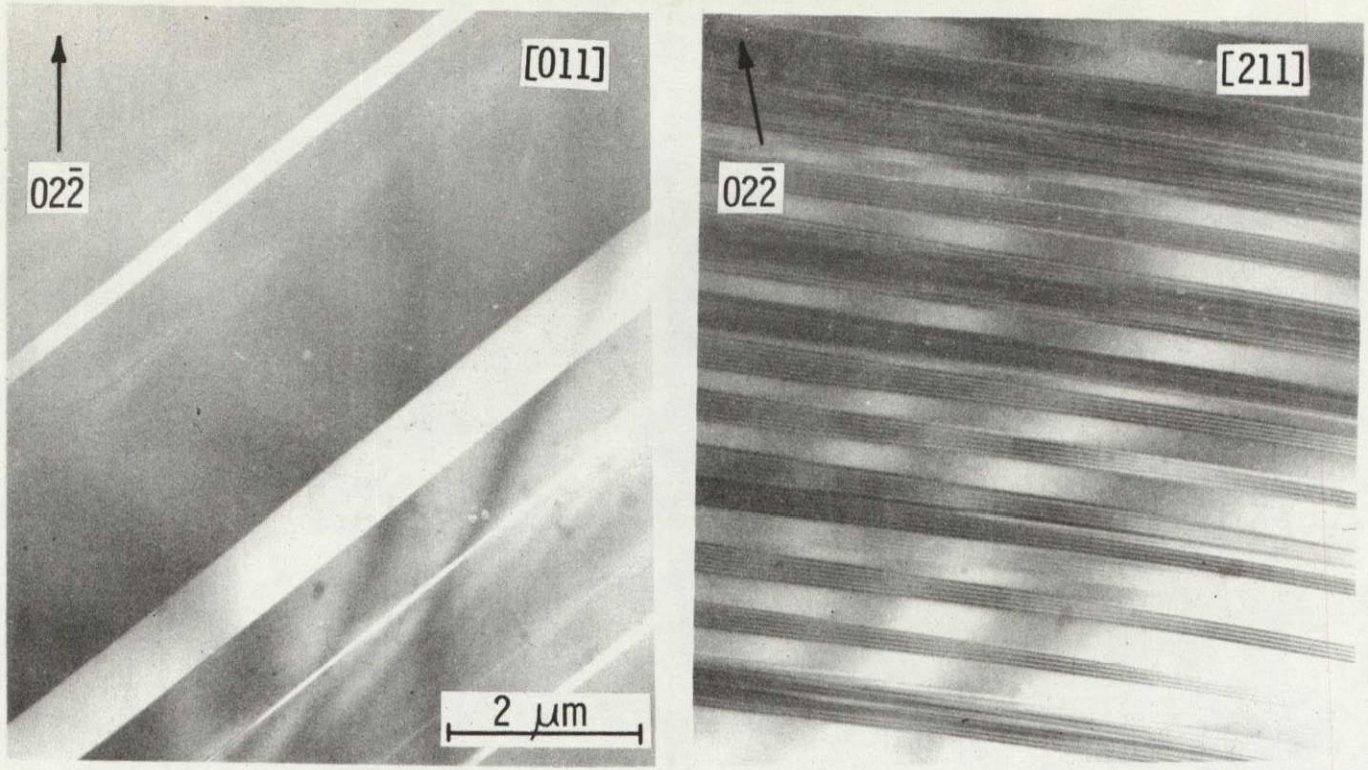

a b

Fig. 4. TEM micrographs showing that the nonactive boundaries are either coherent twin boundaries or stacking faults. (a) (011) and (b) (211) surface orientation.

between these nonactive boundaries, if any, are of very low density. There is only very weak electrical activity connected with such crystal areas.

Electrical activity of dislocations depends on type, distribution, and density. It can vary from weak to strong. First, we discuss homogeneously distributed dislocations. An example is seen in the EBIC image shown in Fig. 5a. The corresponding optical micrograph obtained after Sirtl etching is given in Figure 5b. A small area out of Fig. 5b is shown magnified in Fig. 5c.

The electrical activity of dislocations can be described by the product of minority carrier lifetime (τ) and dislocation density (N_D). For the 60 degree dislocations in ribbons, we find experimentally that $N_D \times \tau \simeq 0.5$ sec·cm^{-2}.

This would indicate that a dislocation density of $5 \times 10^5/cm^2$ results in a lifetime of 1 μsec. Thus dislocation densities of up to $10^5/cm^2$ are of relatively low electrical activity and acceptable in ribbon section.

The crystallographic nature of such dislocations was investigated. TEM studies show that for ribbons of [011]

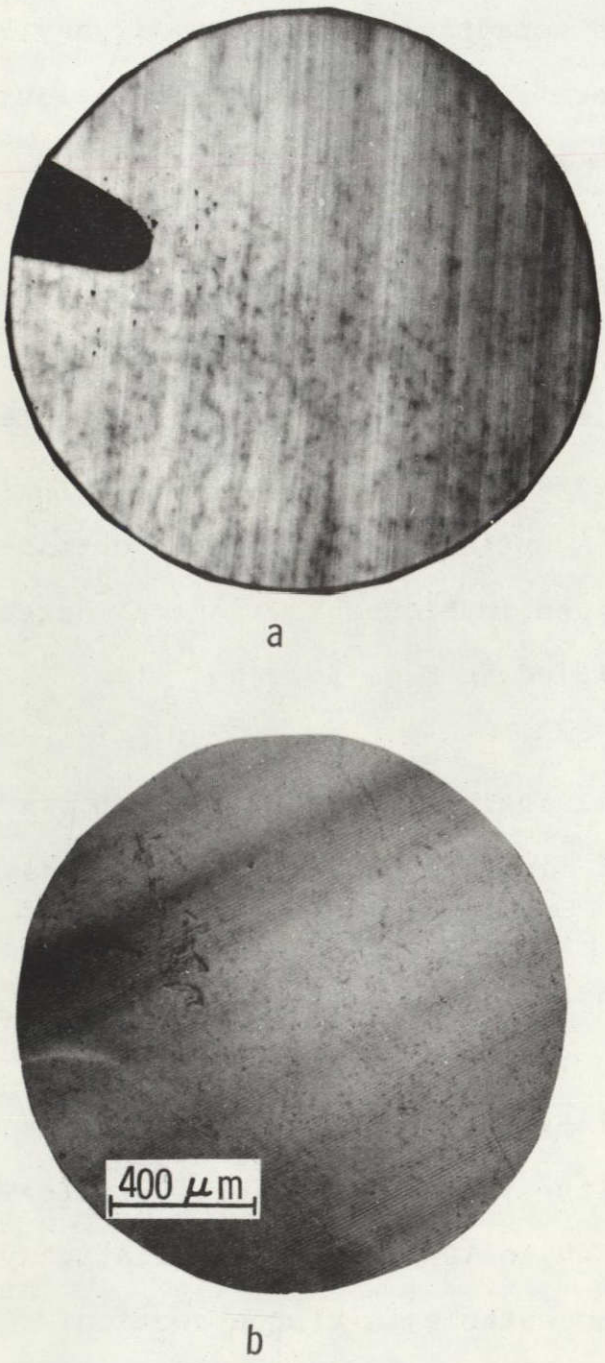

Fig. 5. (a) EBIC micrograph showing the electrical activity of dislocations. (b) The corresponding optical micrograph obtained after Sirtl etching.

C

Fig. 5. (c) A small area of 5 (b) at higher magnification showing dislocation etch pits. The dislocation density, N_D, is about 1 x 10^5 per cm^2.

surface orientation, the dislocations are of the 60 degree type with Burgers vector either parallel or inclined to the ribbon surface.

The dislocations are generated by stresses produced through the relatively large thermal gradients associated with the CAST growth technique. The density of dislocations (N_D) resulting from thermal stress effects can be estimated according to: $N_D = (\alpha/a) \cdot \delta\Delta T$ where $\alpha = 5 \times 10^{-6}/^{o}C$, is the expansion coefficient of Si, $a = 5.42 \times 10^{-8}$ cm, is the lattice constant of Si, and $\delta \Delta T$ is the deviation from the average thermal gradient ΔT at the interface. The deviation from the average thermal gradient at the growth front is estimated to be approximately $100^{o}C$. This yields a dislocation density of approximately $10^4/cm^2$, in good agreement with the density observed in the ribbons.

Quite frequently a second type of dislocation arrangement occurs in CAST ribbons. Typical for this arrangement are dislocations piled up against twin boundaries in the slip directions. Such dislocation pile-ups lead to interesting interactions between twin boundaries and dislocations. As a result of this interaction, twin boundaries deteriorate and become electrically active.

A TEM micrograph of such a boundary section is shown in

Fig. 6 for a ribbon of [211] surface orientation. Figure 6 shows that the slip dislocations pile-up against the linear boundary. In this area, the boundary degenerates into multiple overlapping faults. The structure of this boundary is remarkably different from the structure of nonactive twins and faults shown in Figs. 3a, 4a and 4b. The degeneration of this boundary is at least partially due to the interaction with the slip dislocations. A mechanism for a possible reaction has been proposed by Friedel[4]:

$$a/2[1\bar{1}0] + a/b[\bar{1}12] \rightarrow a/3[1\bar{1}1] \rightarrow a/b[21\bar{1}] + a/6[01\bar{1}]$$

This mechanism suggests that a slip dislocation with Burgers vector $a/2[1\bar{1}0]$ in the $(11\bar{1})$ slip plane reacts with a twin dislocation $b = (a/6)[\bar{1}12]$ in the $[1\bar{1}1]$ twin plane to form a Frank dislocation $a/3\ [1\bar{1}1]$. The Frank dislocation disassociates into a Shockley and a stair-rod dislocation. In Fig. 6, the straight dislocations (marked S) in the [011] direction is most likely a stair-rod dislocation. It should be noted that the slip dislocations located approximately in the [011] or [101] directions are 60 degree dislocations; such dislocations are electrically active due to their dangling bond structure. Quite often different types of linear boundaries of moderate activity are also observed. An example is shown in Figs. 7. Upon Sirtl etching, such boundaries show a high density of dislocation etch pits. This can be seen in Fig. 7a. Note that the dislocation density between such boundaries in a grain is very low. A

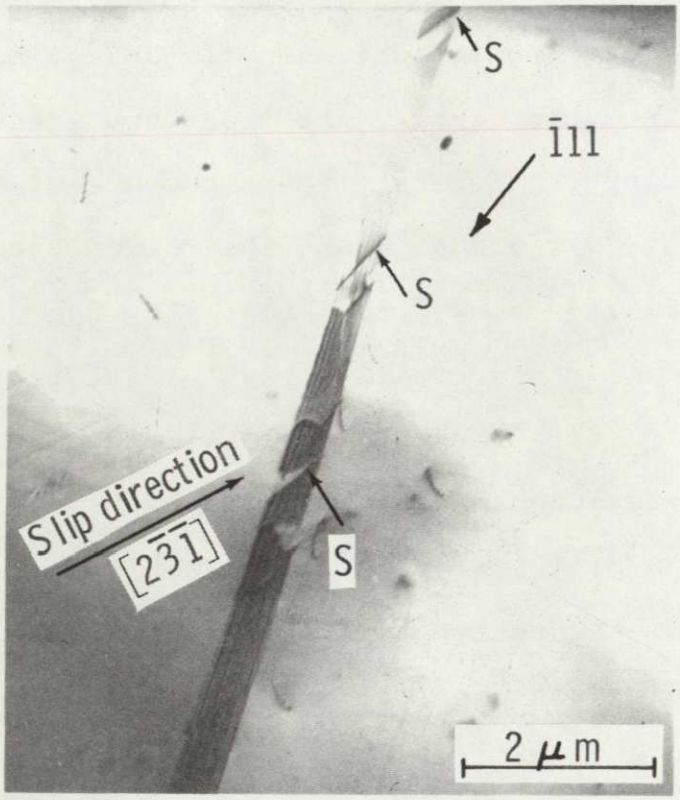

Fig. 6. TEM micrograph showing dislocation piling-up against a twin boundary in the slip direction.

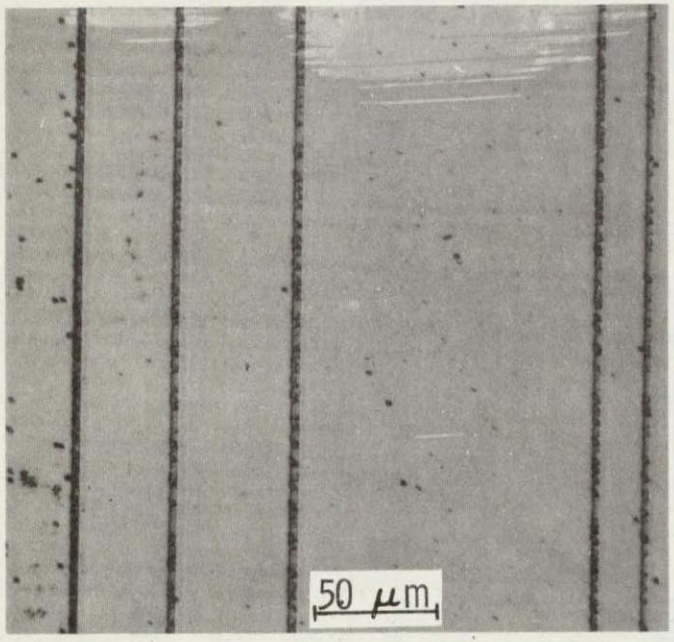

a

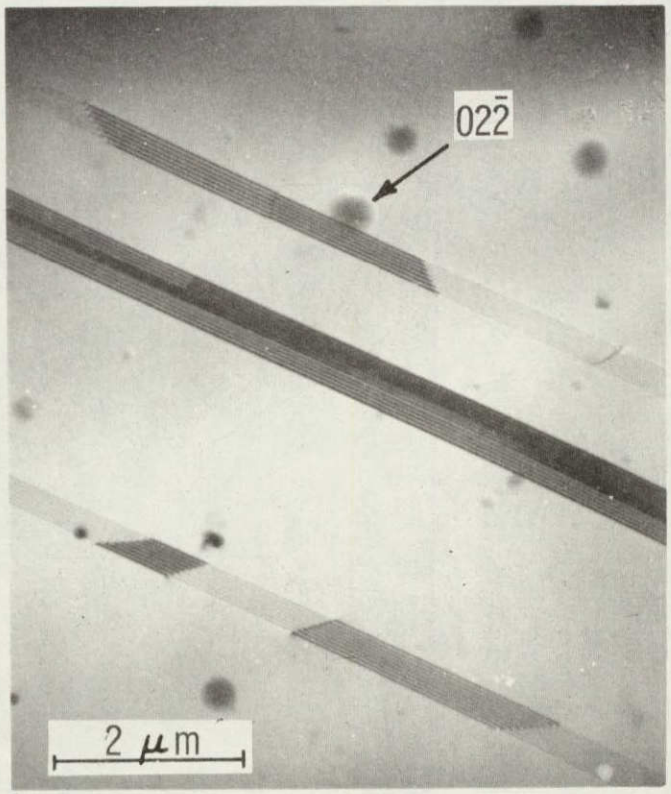

b

Fig. 7. (a) Optical micrograph showing that after Sirtl etching, linear boundaries of moderate activity reveal a high density of etch pits. (b) TEM micrograph showing that the boundaries in (a) consist of segments of stacking faults bounded by partial dislocations.

TEM micrograph showing these boundaries is given in Fig. 7b for a ribbon of [211] surface orientation. Fig. 7b indicates that the boundaries consist of segments of stacking faults bounded by partial dislocations. The bounding partials arrange in a <110> direction. It is evident that the etch pits observed after Sirtl etching result from the emergence of these partials at the ribbon surface.

It also can be seen that the fringe contrast associated with these faults changes in two neighboring segments. The change in fault contrast is due to the change in fault nature. It changes from intrinsic to extrinsic or vice versa. An example is given in the bright-field and in the dark-field images of Figs. 7c and 7d, respectively. According to established constrast criteria[3], the fault nature is intrinsic for segment I and extrinsic for segment II. These types of stacking faults have been observed in deformed nickel by Murr[5]. He considers a single intrinsic stacking fault as a one-layer twin with the twin boundaries characterized by intermixed regions of (h.c.p.) structure. An extrinsic stacking fault, (two overlapping instrinsic faults) is therefore a two-layer twin with contacting h.c.p. regions. In effect, N-stacking faults on every (111) plane form an N-layer twin.

Fig. 7. (c) The bright-field and (d) the dark-field images showing that two neighboring segments of a fault are different in nature. Segment I is extrinsic and segment II intrinsic.

Therefore, the faults shown in Fig. 7b can be considered as multiple layers of overlapping twins. The intrinsic segments are one-layer twins, and the extrinsic segments are two-layer twins. The fringe contrast arising from a three-layer twin is relatively weak.

2.2.2 DEFECTS IN CLASS II RIBBONS

As ribbon quality degrades, dislocation bands and degenerated linear boundaries are the dominant defects in silicon ribbons. Such defects are strongly electrically active and are shown in Figs. 8a and 8b. It can be seen that boundaries at position L are much more active than the boundaries at position F. Fig. 8c is a high magnification of area A indicated in Fig. 8a, and shows differences in the etching characteristics of boundaries at positions L and F. While boundary F is revealed as a sharp line, conical etch pits are seen along the boundary L. Linear boundaries of such etching behavior are low-angle grain boundaries. This is supported by the following observation: Conical pits are also observed along such boundaries whenever they are etched from the backside as it is done for TEM specimen preparation. The etch pits are similar to the one observed along low-angle tilt boundaries in germanium[6].

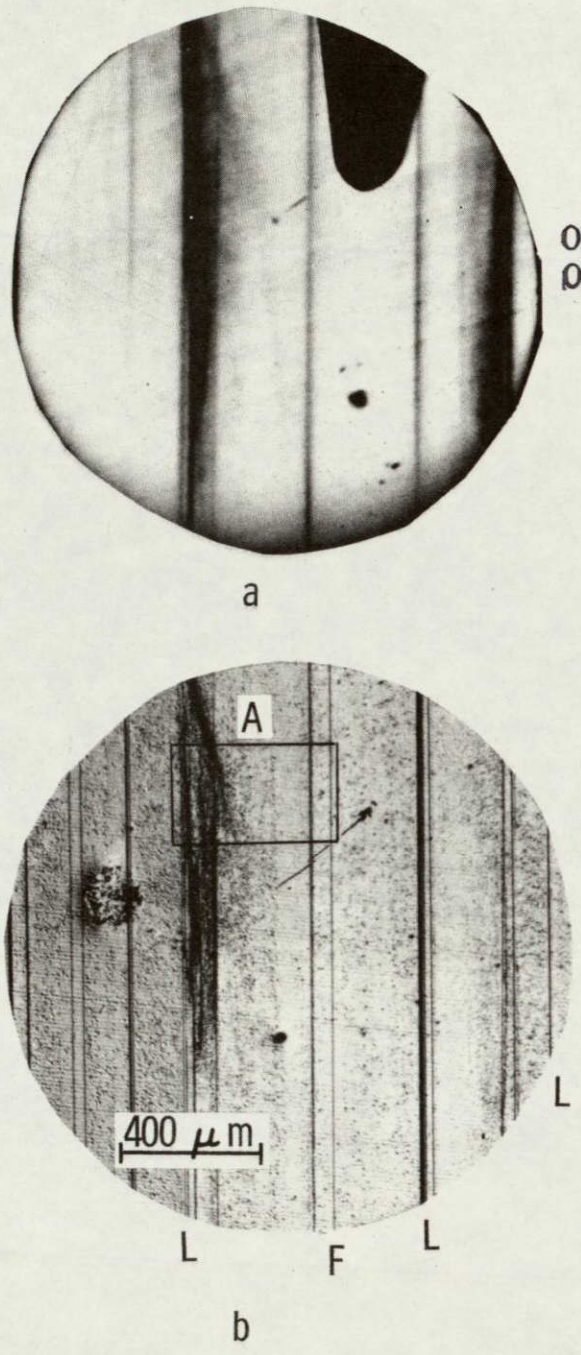

Fig. 8. (a) EBIC micrograph showing that dislocation bands and degenerated linear boundaries are strongly electrically active. (b) The corresponding optical micrograph of (a).

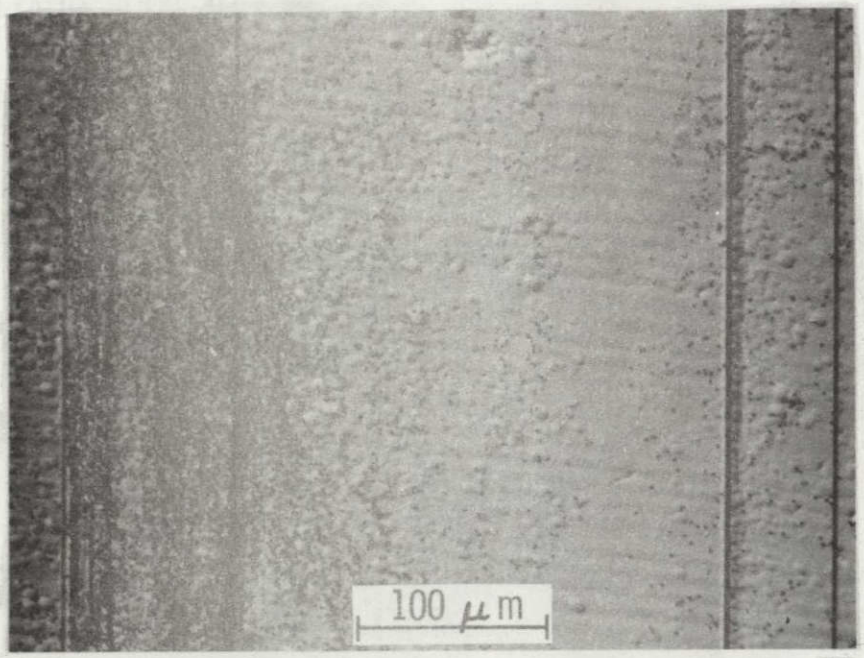

C

Fig. 8. (c) Area A of Fig. 8 at highest magnification. Note differences in the etching characteristics of boundaries L and F.

The TEM micrograph of a low-angle grain boundary L for a ribbon of [011] surface orientation is shown in Fig. 9. The boundary L as well as the twin planes T are in the $(1\bar{1}1)$ plane perpendicular to ribbon surface. The specimen was tilted into the $\{\bar{1}21\}$ zone to display the dislocation structure in the boundary. Figure 9 shows that the boundary consists of parallel dislocation arrays in the <110> directions. The spacing between these dislocations ranges from 0.1 to 0.4 μm with an average spacing of 0.2 μm. Most of the dislocations are out of contrast for the $[11\bar{1}]$ reflection in the $\{\bar{1}21\}$ zone and also for the $[13\bar{1}]$ reflection in the {013} zone. Thus the Burgers vector, b, of these dislocations is a/2 [101].

The misorientation θ between the grains A and B associated with the boundary can be measured directly from the diffraction pattern of a selected area (SAD). This is done in the microscope by adjusting the surface normal of grain B, the [011] axis, almost parallel to the main beam as shown in Fig. 9. The misorientation between grains A and B is measured as the shift of the [011] axis with respect to the main beam. The SAD of grain A shows that the shift is approximately two [111] spacings in the $[1\bar{1}1]$ direction. From the Bragg equation, one [111] spacing corresponds to 0.46 degrees for 200 Kev electrons. The misorientation is

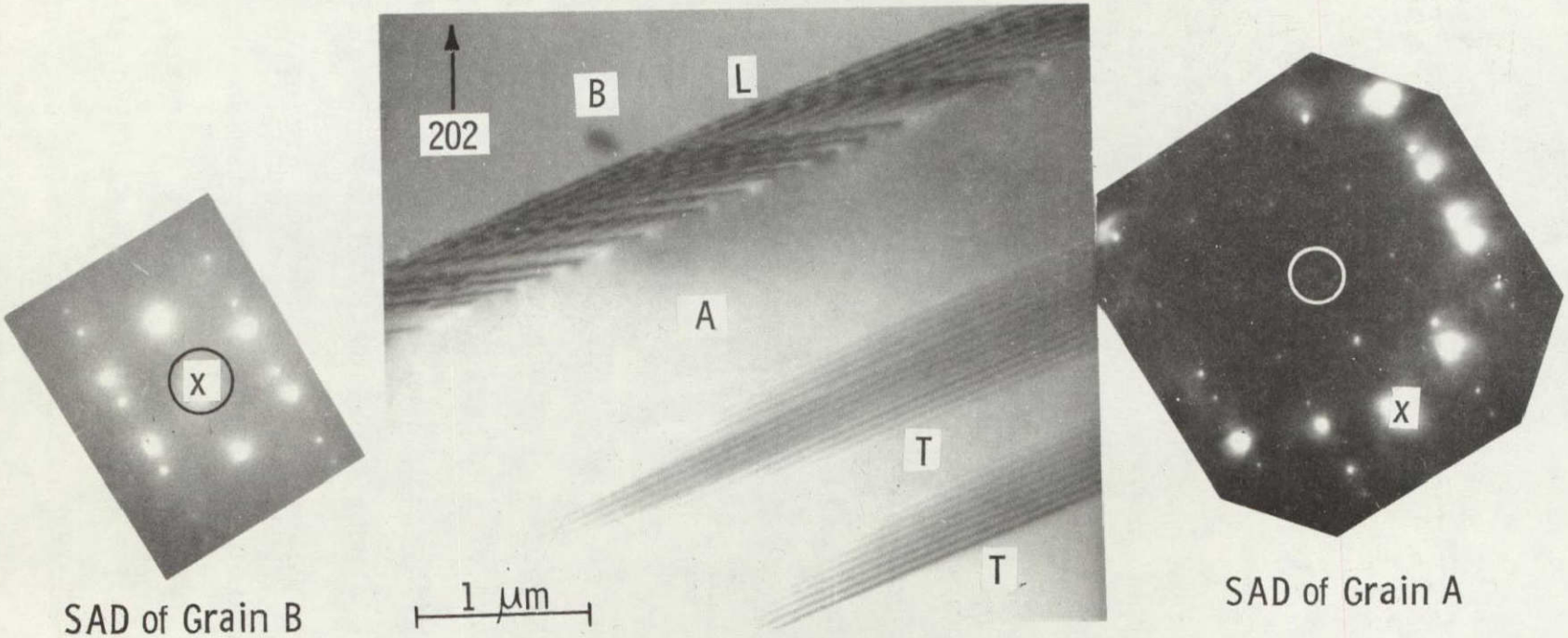

Fig. 9. TEM micrograph showing dislocations associated with a low-angle grain boundary. The misorientation between grain A and B as measured from the shift of the [011] axis (O) with respect to the main beam (X) is about 0.92°.

therefore approximately 0.92 degrees. Thus, the boundary is a low angle tilt boundary with the rotation axis in the [21$\bar{1}$] direction. This direction is the growth direction. The misorientation, is only 0.22 degrees if calculated from the dislocation spacing D (taken as 0.2 μm). However, it should be noted that in some cases, the shift of the surface normal is in the [0$\bar{1}$1] direction rather than in the [1$\bar{1}$1] direction. Thus, the boundary is not of the pure tilt type but is a mixture of a tilt and a twist boundary.

Although areas of low dislocation densities have a negligible influence on the minority carrier lifetime high dislocation densities as present in dislocation clusters or bands (Fig. 8c) represent areas of strong electrical activity. Again, a Burgers vector analysis of the dislocations in such clusters was made. For the sample area shown in Fig. 8c, different TEM micrographs were recorded using different operating reflections (g) in the <011> and <112> zones. Examples of these micrographs are given in Fig. 10a through 10e. The results are summarized in Table II.

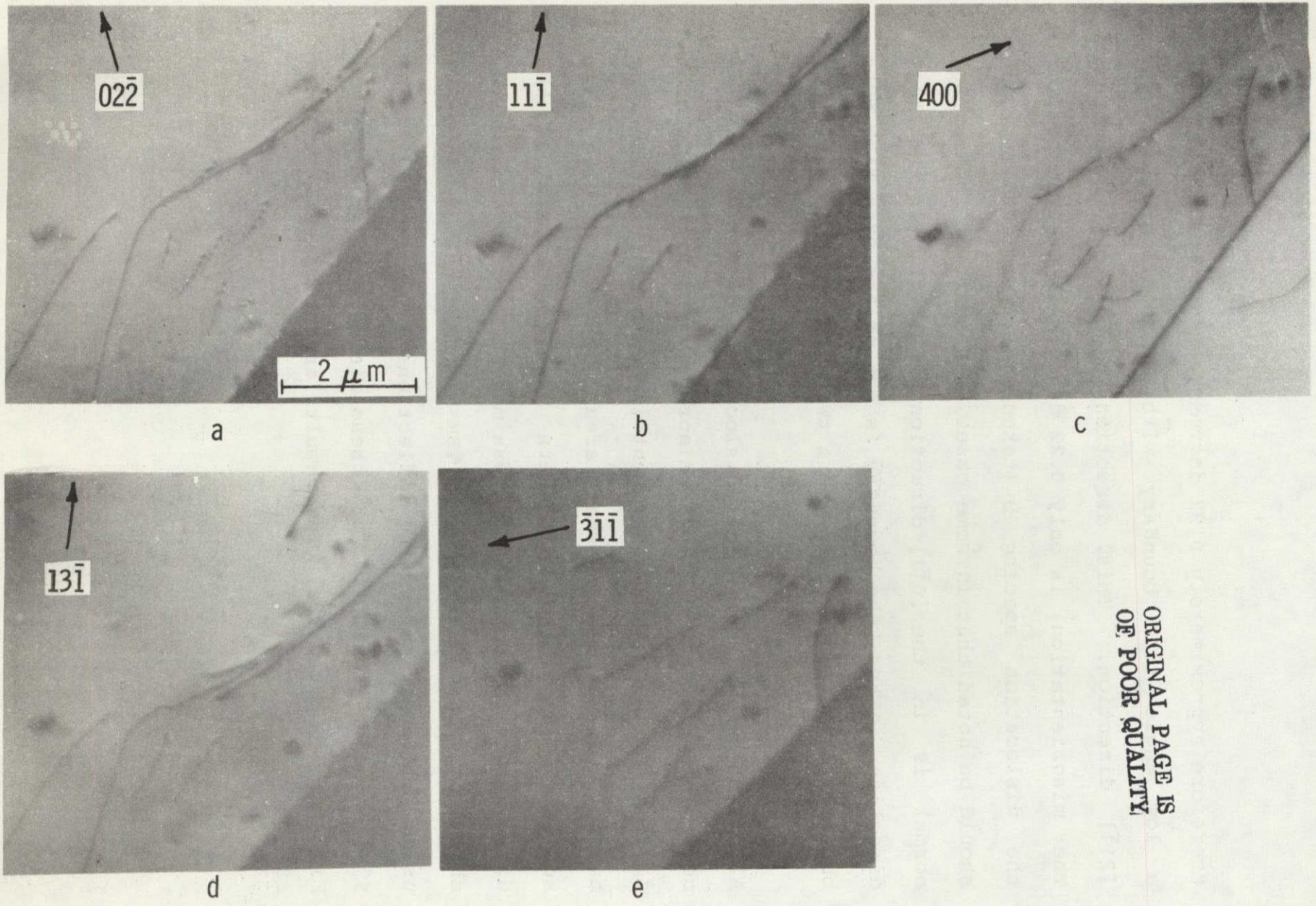

Fig. 10. TEM micrographs for the determination of Burgers vectors of band dislocations. (a) 022, (b) 111, (c) 400 (d) 131 and (e) 311 reflection.

TABLE II. Burgers Vector Analysis of Dislocation Bands

Dislocation No.	g for Dislocation Invisibility	Burgers Vector b	Dislocation Direction
1	$11\bar{1}$, $13\bar{1}$	a/2 [101]	[110]
2	400, $\overline{311}$	a/2 [$01\bar{1}$]	[110]
3	$11\bar{1}$, $13\bar{1}$	a/2 [101]	
4	400, $\overline{311}$	a/2 [$01\bar{1}$]	
5	400, $\overline{311}$	a/2 [$01\bar{1}$]	

Accordingly, the dislocations have Burgers vectors of the a/2 <110> type, either parallel or inclined to the (011) ribbon surface.

There are two groups of dislocations distinctly different in their line directions. One group, dislocations #1, 2 and 3, in Table II is inclined to the surface and the other, dislocation #5 in Table II is nearly parallel to the surface in the [211] growth direction. Both groups have similar Burgers vectors. Stereomicrographs reveal that the inclined dislocations tend to stay in a <110> direction whenever they are in the neighborhood of a linear boundary. Their orientation becomes ill-defined when they move away from the boundary. An example of such inclined dislocations present in a relatively small grain of several microns in size and bounded by two linear boundaries is shown in Fig. 11.

The long dislocations with line directions directed into the growth direction are observed at a relatively large distance from a linear boundary. Fig. 12a shows such long dislocations. The Burgers vectors of these dislocations is either a/2 [01$\bar{1}$] or a/2 [101], and is the same as found for the inclined dislocations (Fig. 11). The formation of these dislocations is observed independent of surface orientation. Another example of long dislocations for the [211] surface orientation, is shown in Fig. 12b. This type of long dislocation directed along the growth direction has also been observed in silicon web-dendrite crystals[7]. In dendrites, their occurrence is stress induced and is the result of liquid entrapment in the dendrite-fillet region. The similarity of such dislocations in web-dendrite and in CAST ribbons is shown in the x-ray topographs of Figs. 13a and 13b. Both have the same Burgers vector.

In most cases, the dislocations assume an intermediate structure between these two groups of dislocations. A stable configuration is formed through interaction of dislocations with different Burgers vectors. Such configurations are shown in Fig. 14a and 14b. Quite often, triple nodes are observed which form according to the reaction: (a/2) [011] + (a/2) [101] → (a/2) [110]. This reaction results in a reduction of half the dislocation

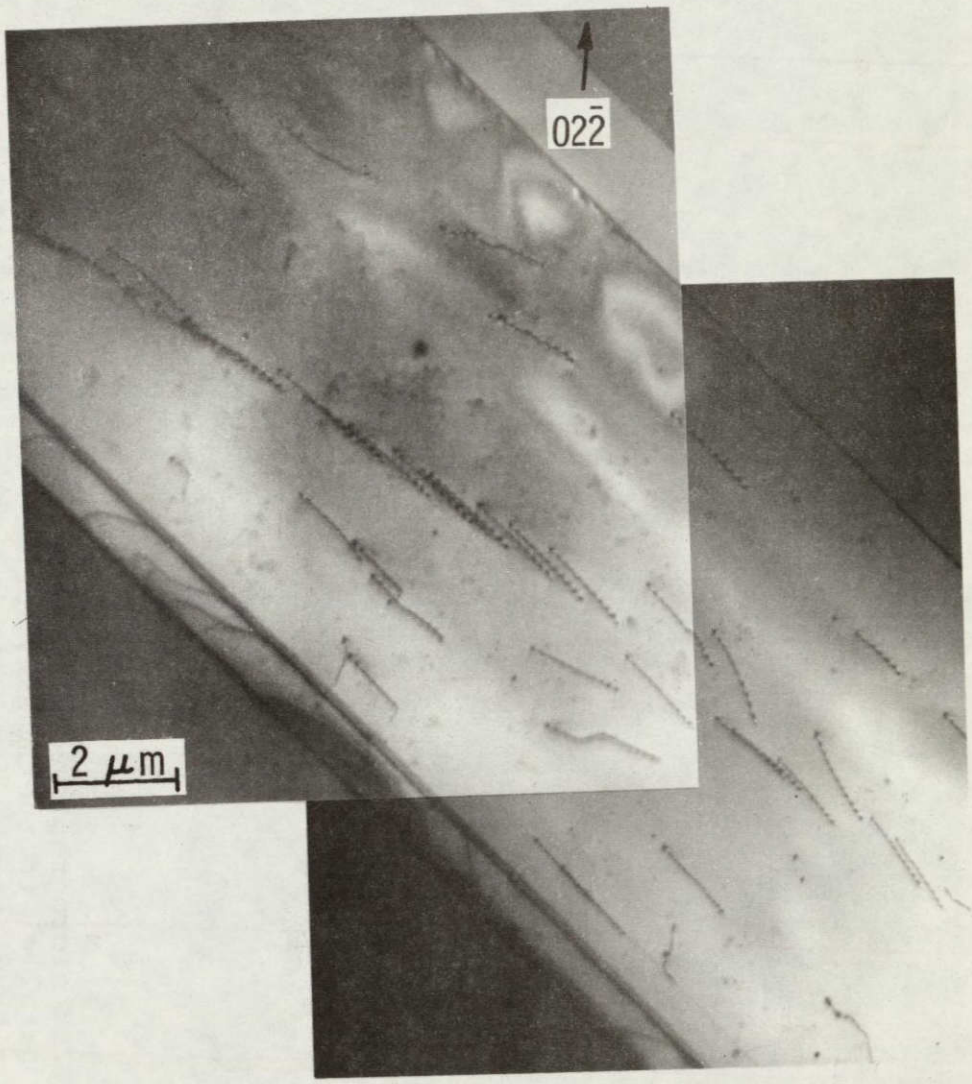

Fig. 11. TEM micrographs showing arrays of inclined dislocations in a grain bounded by two linear boundaries.

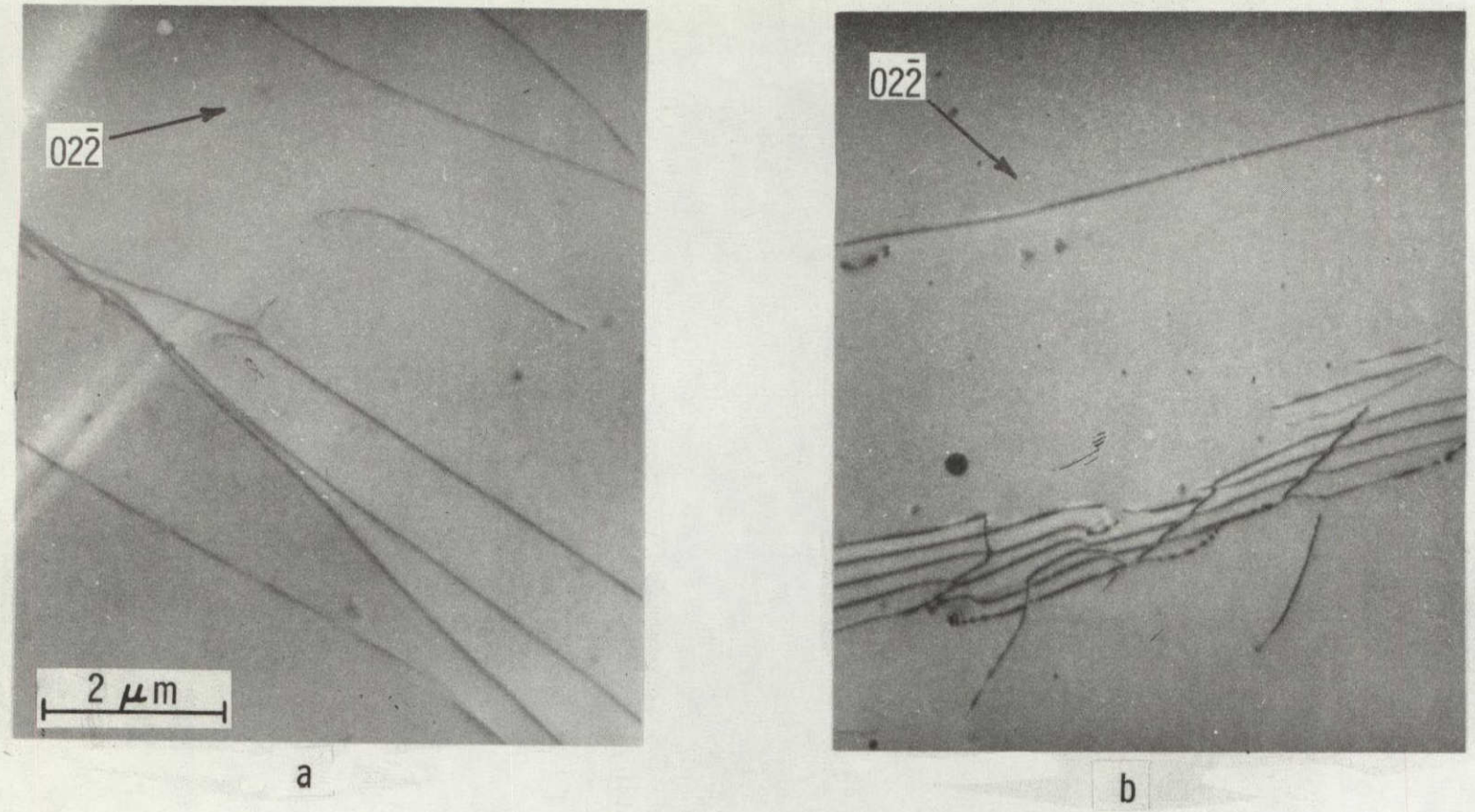

Fig. 12. TEM micrographs showing dislocations lying nearly parallel to the ribbon surface and running in the ribbon growth direction in ribbons of (a) (011) and (b) (211) surface orientation.

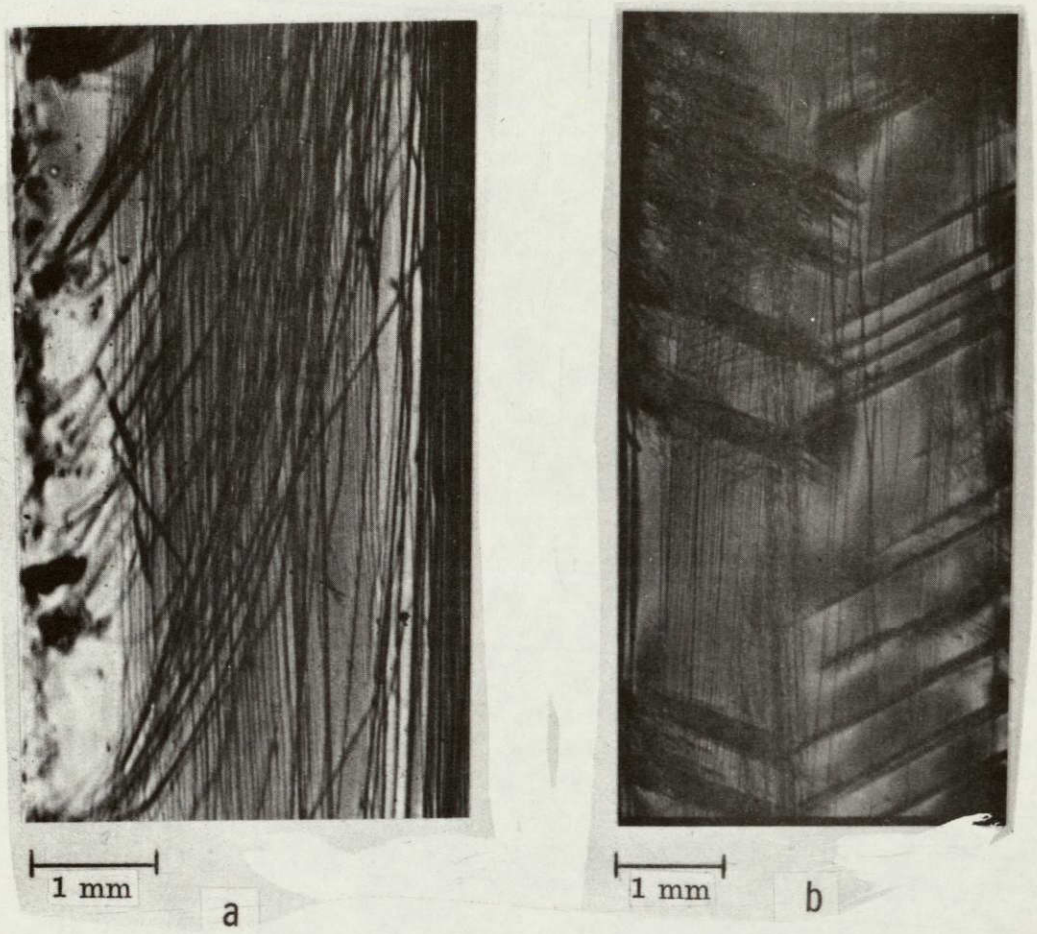

Fig. 13. X-ray topographs showing that dislocations tend to align in the growth direction in (a) web-dendritic crystals and in (b) CAST ribbons.

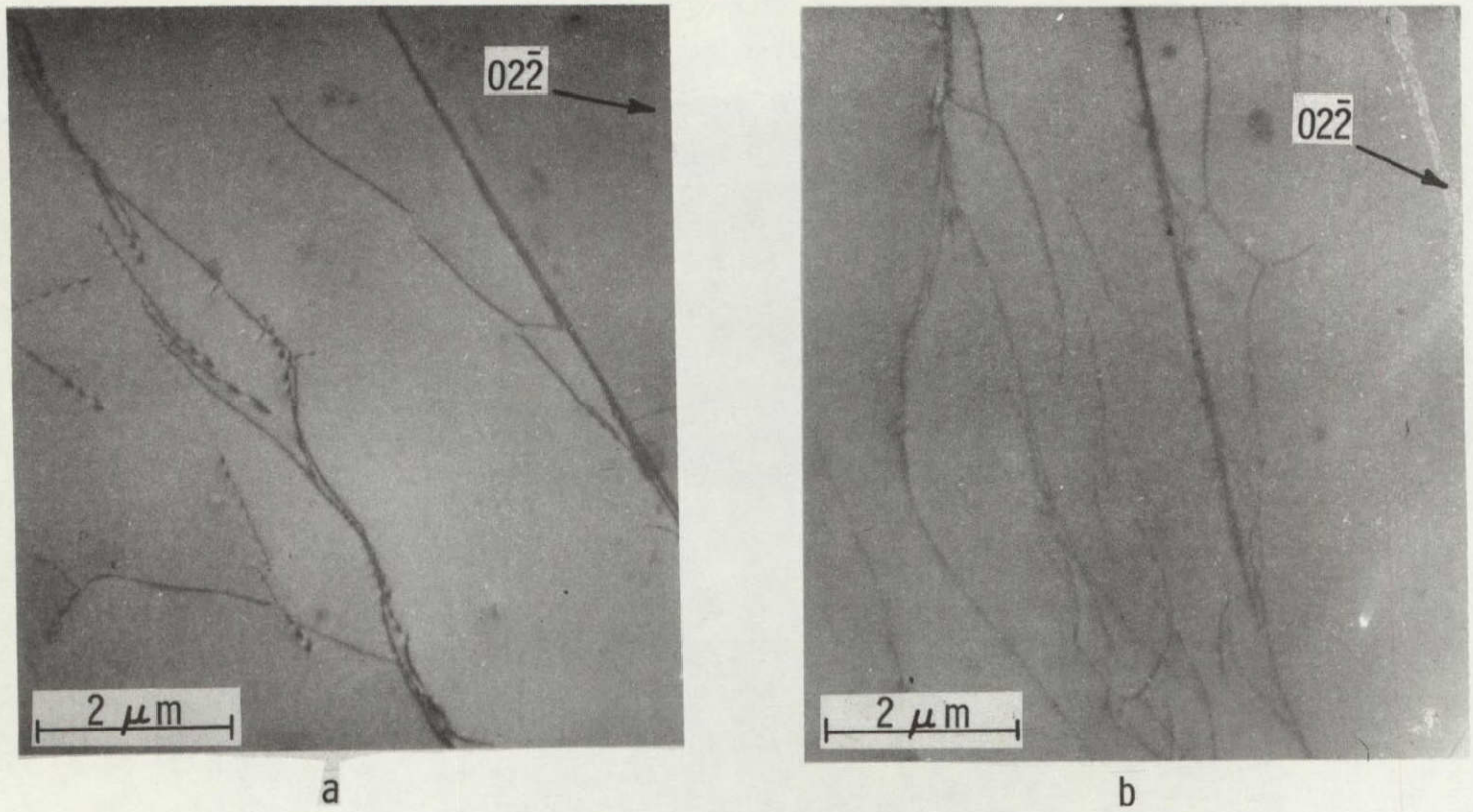

Fig. 14. TEM micrographs showing two examples, (a) and (b), of stable dislocation configurations formed through interaction of dislocations with different Burgers vectors.

energy. The resultant segments, with Burgers vector b = a/2 [110], are in the [$\bar{1}$10] direction. Thus, they are 90 degree dislocations with the unfavorable (001) slip plane. The movement of dislocations of type #5 in Table II is retarded through this reaction.

The misorientation of the grains across the boundaries and the detailed structure of such boundaries as shown in Figs. 8 through 11 were also investigated. The misorientation ranges in general from 0.5 to 1 degree off the [1$\bar{1}$1] direction. A typical structure of such a boundary as viewed from a [211] projection is shown in Figs. 15a and 15b. These boundaries consist of multiple overlapping layers of stacking faults or twins. Note that quite often they act as dislocation sources. While one end of a dislocation is emitted from a boundary, Fig. 15a, the other end is still pinned at the boundary. This suggests that the emission of a dislocation may result from the defaulting or from the detwinning of such a boundary. The formation of dislocation loops and dislocation lines as a result of such defaulting processes can also be clearly seen in Fig. 15b. Figure 15c shows that one dislocation loop and two dislocation segments are about to be emitted from a linear boundary.

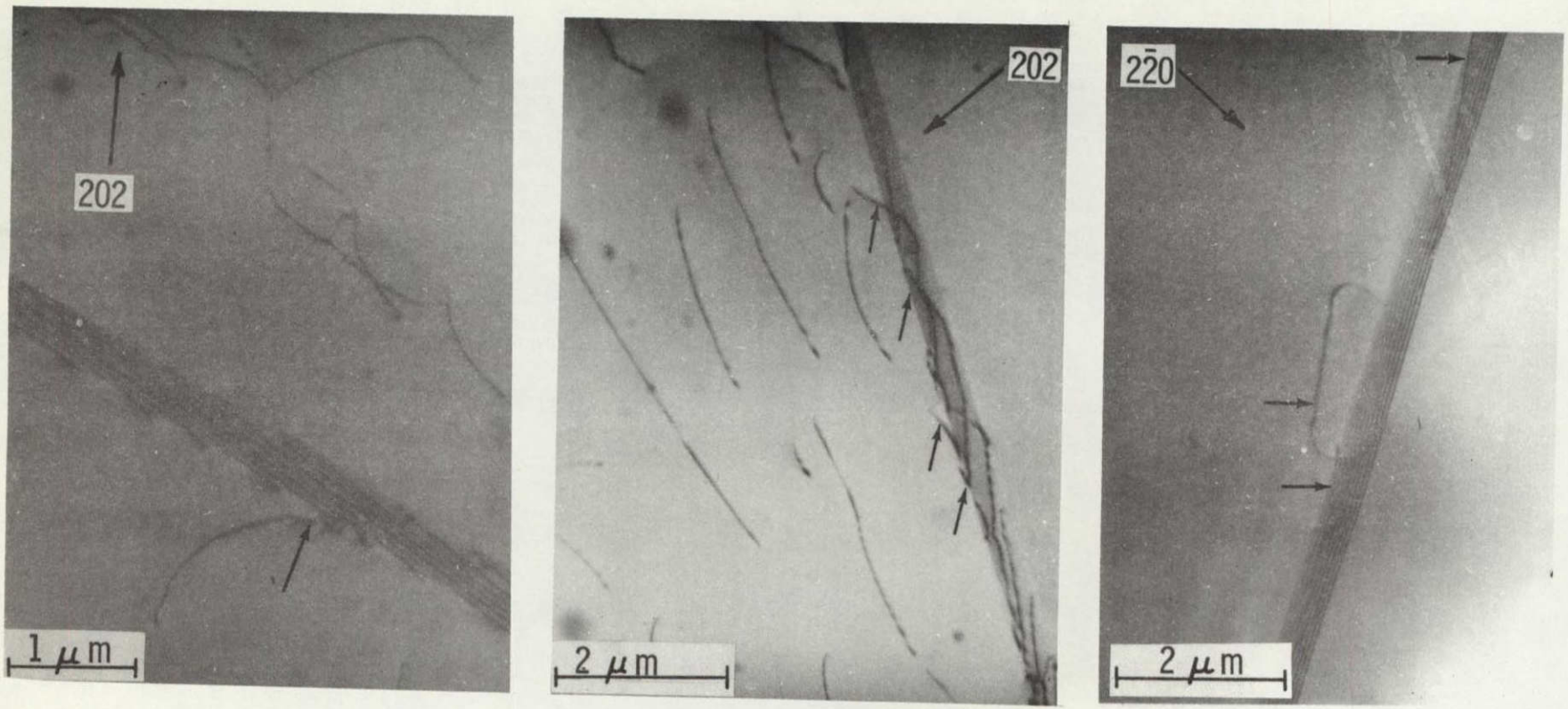

Fig. 15. TEM micrographs showing that (a) a dislocation segment, (b) dislocation segments and loops and (c) one loop and two segments as indicated by arrows are about to be emitted from a linear boundary.

2.2.3 DEFECTS IN CLASS III RIBBONS

As ribbon quality continues to degrade, grain boundaries as well as other active defects become more predominant. Grain boundaries show strong electrical activity as shown in Figs. 16a,b and 17a,b. Figs. 16c and 17c show also that a high etch-pit density is typical for dislocation bands. However, close to the grain boundaries the dislocation density is relatively low. The structure of the grain boundaries obtained after chemical etching (Fig. 16c) appears similar to that of the low-angle grain boundaries, shown in Fig. 8c at positions L. As shown later by TEM analysis grain boundaries contain a high density of closely spaced dislocations. The strong electrical activity of grain boundaries arises from such dislocations. Grain boundary dislocations in silicon ribbons are not revealed by chemical etching.

The electrical activity of various crystal defects ranging from nonactive parallel twins to strongly active dislocation bands and grain boundaries is again illustrated in Figs. 17a,b.

Grain boundaries are the result of non-accommodation of two crystal lattices at the intersection of two crystal grains. Under steady-state growth conditions, silicon

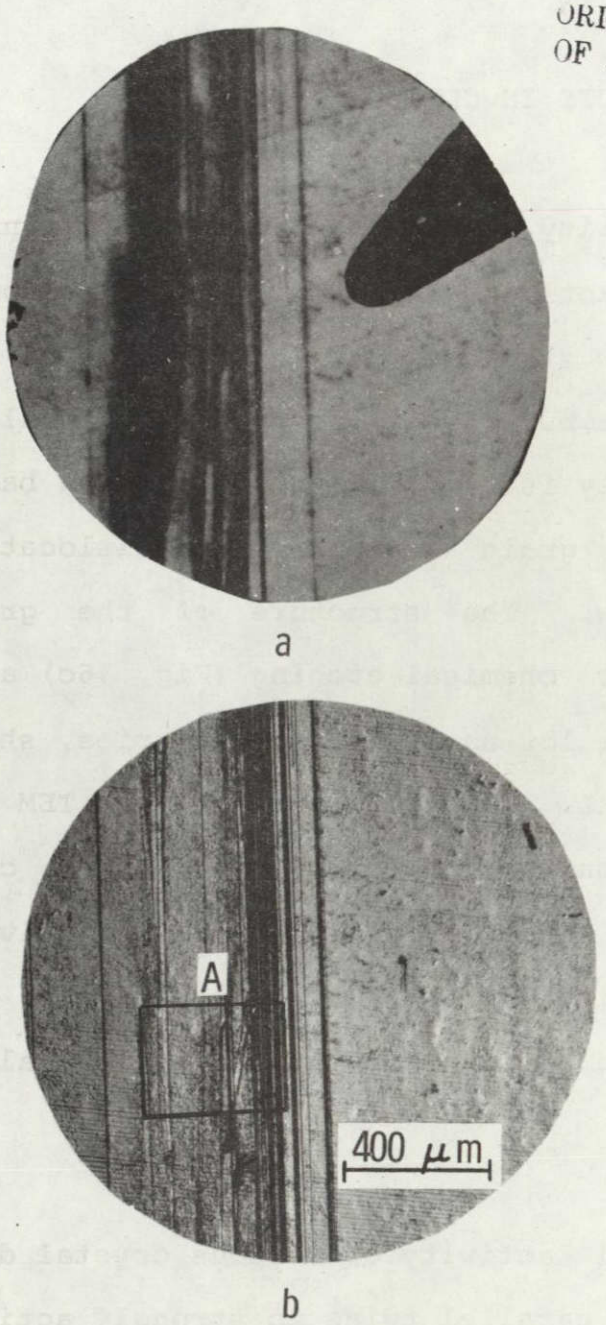

Fig. 16. (a) EBIC micrograph showing that grain boundaries and dislocation bands are strongly electrically active. (b) The corresponding optical micrograph of (a).

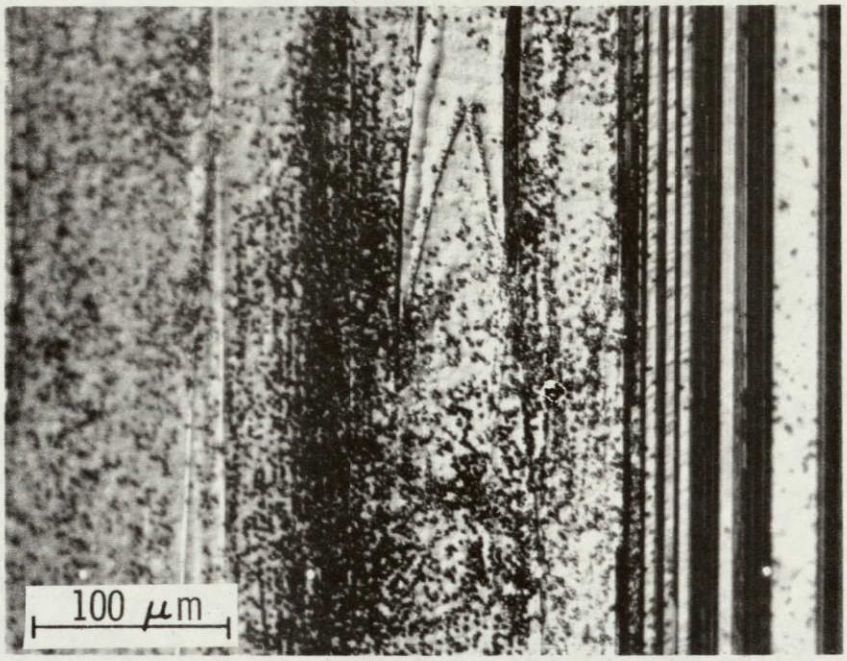

C

Fig. 16. (c) Area A marked, in Fig. 16b at higher magnification. Note a high density of dislocation etch pits.

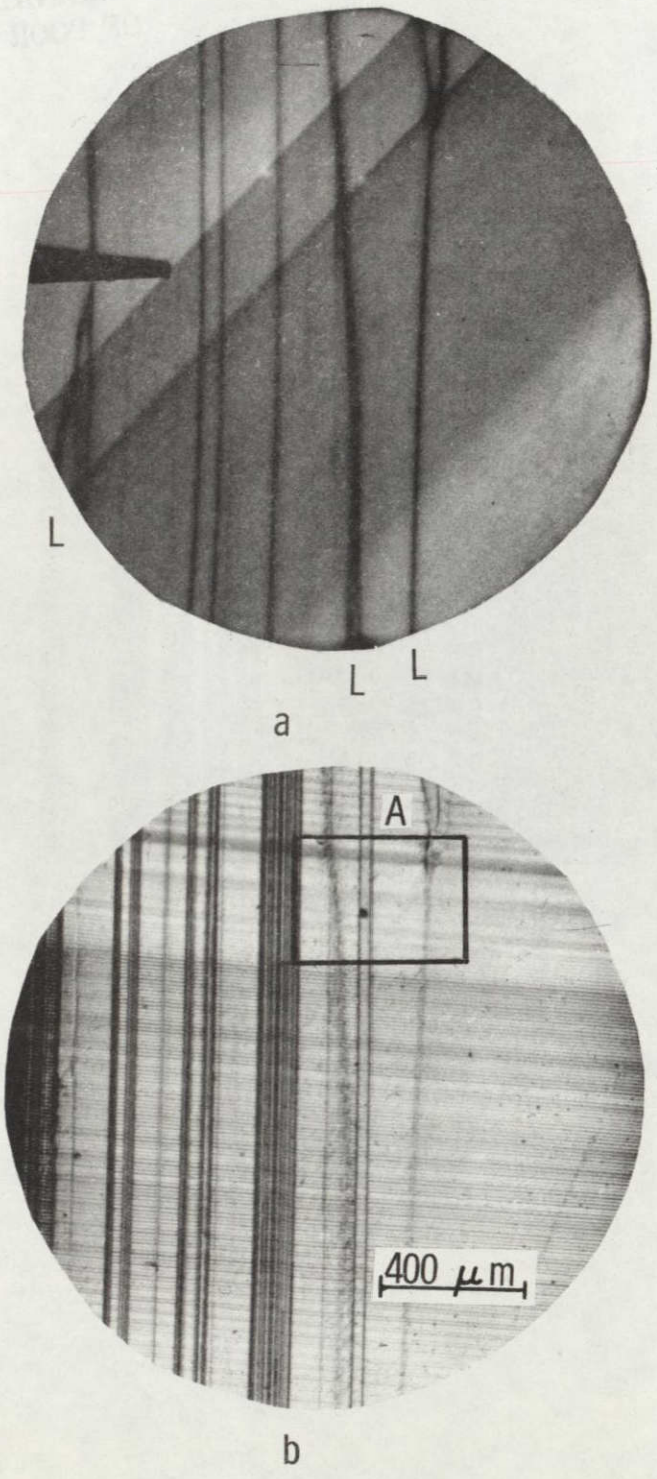

Fig. 17. (a) EBIC micrograph showing electrical activity of grain boundaries at position "L". (b) Optical micrograph corresponding to (a).

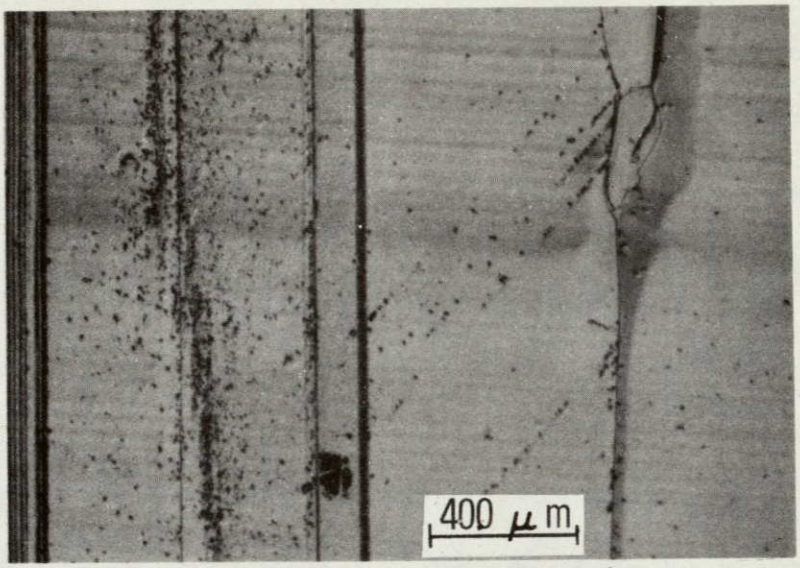

Fig. 17. (c) Area A in Fig. 17b at higher magnification shows high etch-pit density in dislocation bands. Note relatively low density close to grain boundaries. Note etch pits in boundaries at positions L.

ribbons assume a preferred surface orientation of [011] or [211]. These orientations tend to minimize surface energy. In addition, the occurrence of [211] surface orientation can also result from the twinning of [011] ribbons. Quite often, grain boundaries form when ribbon crystals of such preferred orientations meet. Two types of boundaries are thus obtained. One appears to be a zigzag boundary with a high density of dislocations piled up against the boundary. The optical micrograph of this type is shown in Fig. 18a. TEM micrographs of such boundaries are shown in Figs. 18b,c. In the TEM micrographs a dislocation pile-up is evident on both sides of the boundary. The boundary itself contains closely-spaced dislocations. The spacing between the dislocations is approximately 0.1 to 0.2 μm. The formation of such boundaries gives rise to a surface step. As a result, TEM specimens prepared from such boundaries show a change in thickness across the boundary. The change in thickness is evident in Figs. 18b,c., because it changes the transmittance of the electron beam. The thicker crystal section appears dark in the micrograph.

Another type of grain boundary is formed at the intersection of <011> and <211> grains and is shown in Fig. 19a. This boundary is straight and the grains on both sides contain parallel faults. The fault density in the [011] grain is higher than it is in the [$\bar{1}$21] grain. The linear faults in

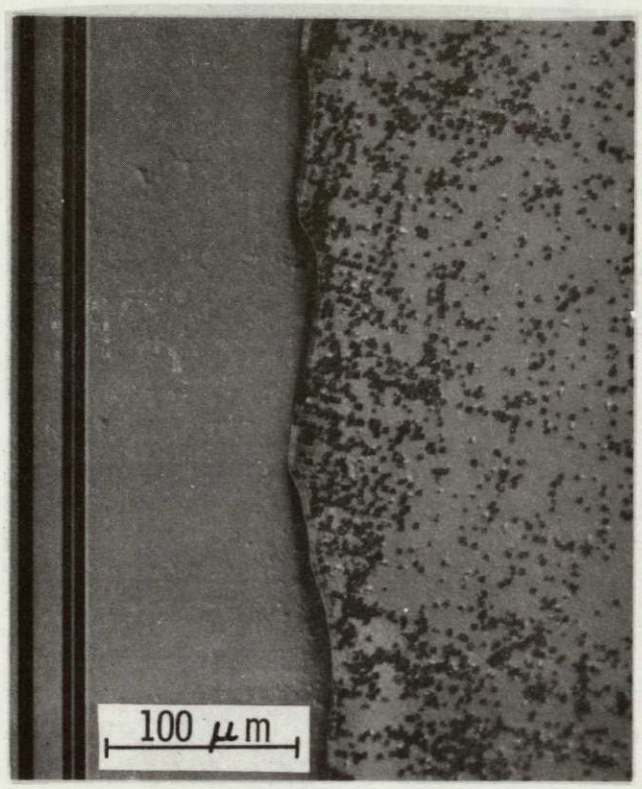

a

Fig. 18. (a) Optical micrograph showing a zigzag boundary with a high density of dislocations piled up against the boundary. Dislocations left of boundary not revealed by etching.

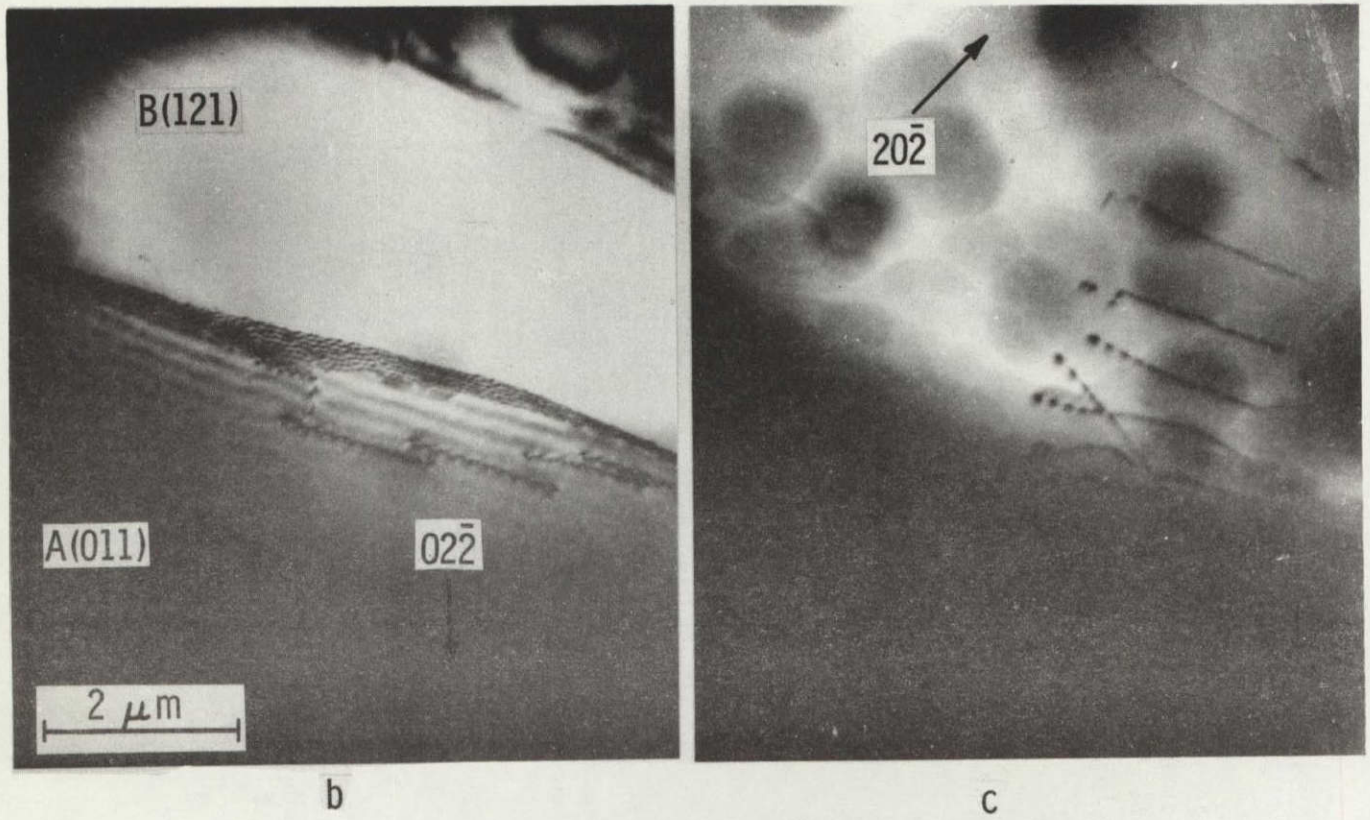

Fig. 18. (b) and (c) are TEM micrographs showing dislocation pileup on both sides of a grain boundary. Due to a change in thickness across the boundary, (b) and (c) were taken with different exposure times.

the [011] grain are in the $(1\bar{1}1)$ plane perpendicular to the surface and run in the $[\bar{2}11]$ direction (Figs. 19a,b). The faults in the $[\bar{1}21]$ grain are in the inclined (111) plane and are in the $[\bar{1}23]$ direction. The grain boundary is in the $[\bar{3}22]$ direction of the [011] grain or in the $[\bar{3}45]$ direction of the $(\bar{1}21)$ grain. Thus the boundary direction makes an angle of 10.7 degrees or 8.05 degrees with the fault direction of the two grains, respectively. Figure 19a shows that this angle is about 9 degrees in both grains. From such data, it is deduced that the grain boundary is in the $(2\bar{1}2)$ plane of the [121] grain. This indicates that both grains have a common (122) boundary plane with a misorientation between the $(2\bar{1}2)$ plane and the $(\bar{2}\bar{1}2)$ plane. This boundary plane makes an angle of 76.3 degrees with the (011) surface or 74.2 degrees with the $(\bar{1}21)$ surface. This indicates that both grains must tilt around the boundary direction by 2.1 degrees, such that the boundary plane can satisfy the crystallographic conditions described. Figure 19b recorded with the g-vector [202] shows that the boundary contains many "ledges". Ledges are defined at the end of the next paragraph. It is interesting to note that the faults typical for each grain do not intersect the grain boundary. Apparently, there is a repulsive force active preventing such an interaction.

A "ledge" structure is observed in nearly all straight portions of a grain boundary independent of the

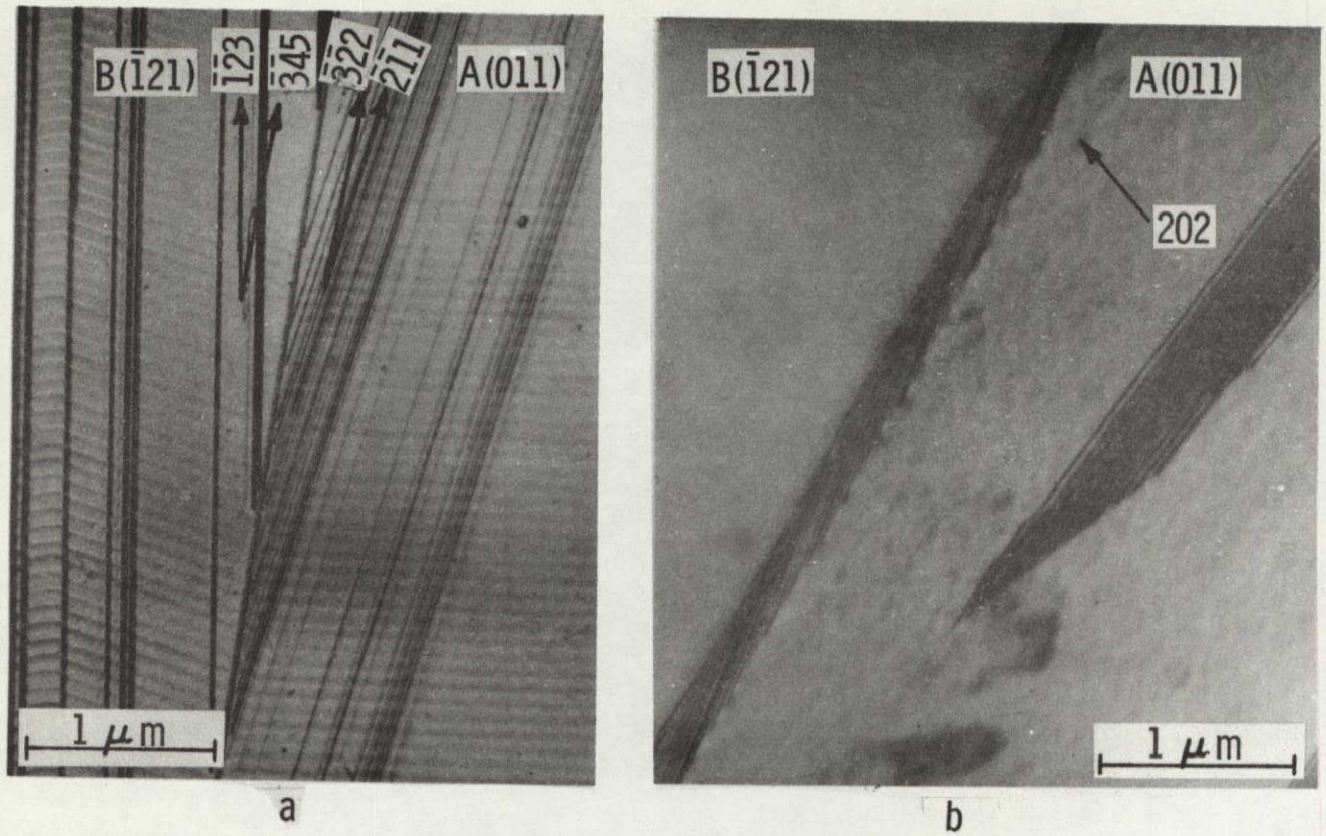

Fig. 19. (a) Optical micrograph showing a grain boundary formed at the intersection of the [011] and the [1̄21] grains. (b) TEM micrograph showing that the boundary contains many ledges. The ledges in the boundary and the fault were revealed by tilting the {011} grain to the {1̄21} zone.

crystallographic plane it occupies. Figures 20a,b show that the ledge contrast arises from the $(11\bar{1})$ grain boundary of a (211) grain. The micrographs in Figs. 20a,b were taken with g-vectors $[\bar{1}11]$ and $[2\bar{2}0]$. With the $[2\bar{2}0]$ reflection, obtained by tilting the specimen towards the [111] zone axis, the ledge contrast disappears and dislocation contrast can be recognized. It is evident that not all "ledges" are dislocations. A similar ledge structure has been observed in grain boundaries of stainless steel[8]. Murr, et al,[8] interpreted such grain boundary ledges as a result of adjustment or of shuffling of the crystal planes forming the boundary. Shuffling of crystal planes is necessary to give rise to coincident lattice sites or boundary positions resulting into a lower energy configuration.

Grain boundaries formed by two grains--one of low index orientation and the other of high-index orientation are also frequently observed. Such grain boundaries contain many dislocations. Figure 21 shows such a boundary formed by grains A, B, and C. As determined from Kikuchi patterns, the surface orientations of the grains marked A, B, C, are [011], $[\bar{2}37]$, and $[\bar{2}73]$, respectively. The dislocation spacing in the boundary varies from 0.1 to 0.2 μm. As the spacing decreases, the dislocations progress from curved lines to straight, parallel lines. These straight dislocations finally pile up at the intersections formed by

Fig. 20. TEM micrograph showing that the ledges lying in the (111) plane of a (211) grain are (a) in contrast with g = $\bar{1}11$, and (b) out of contrast with g = $2\bar{2}0$ by tilting the grain toward the (111) zone.

the grain boundary G and boundaries S_2, and T. This indicates that such intersections act as a barrier for the movement of these dislocations. The parallel boundaries, S_1 and S_2, are stacking faults, boundary T is a twin boundary as determined from the contrast of the outer fringes. It should be noted that the dislocation contrast appears to be dark when grain C is the strongly diffracting grain, (Fig. 21a). The contrast reverses for opposite g vector. This contrast reversal is not observed when grain A acts as the strongly diffracting grain. According to McDonald and Ardell[9], such a contrast reversal occurs only in the grain boundary which lies in the lower surface of the strongly diffracting grain. Therefore, the boundary G lies in the lower surface of grain C or the upper surface of grain A.

The strong activity of grain boundaries is tied to the low density of coincidence lattice sites available in such boundaries. In order to lower the boundary energy, lattice bonds at the boundaries must rearrange themselves. This leads to bond distortion and, as a result gives rise to a high density of dislocations or ledges. These dislocations and/or ledges act as strong recombination centers and cause the strong electrical activity of the fault.

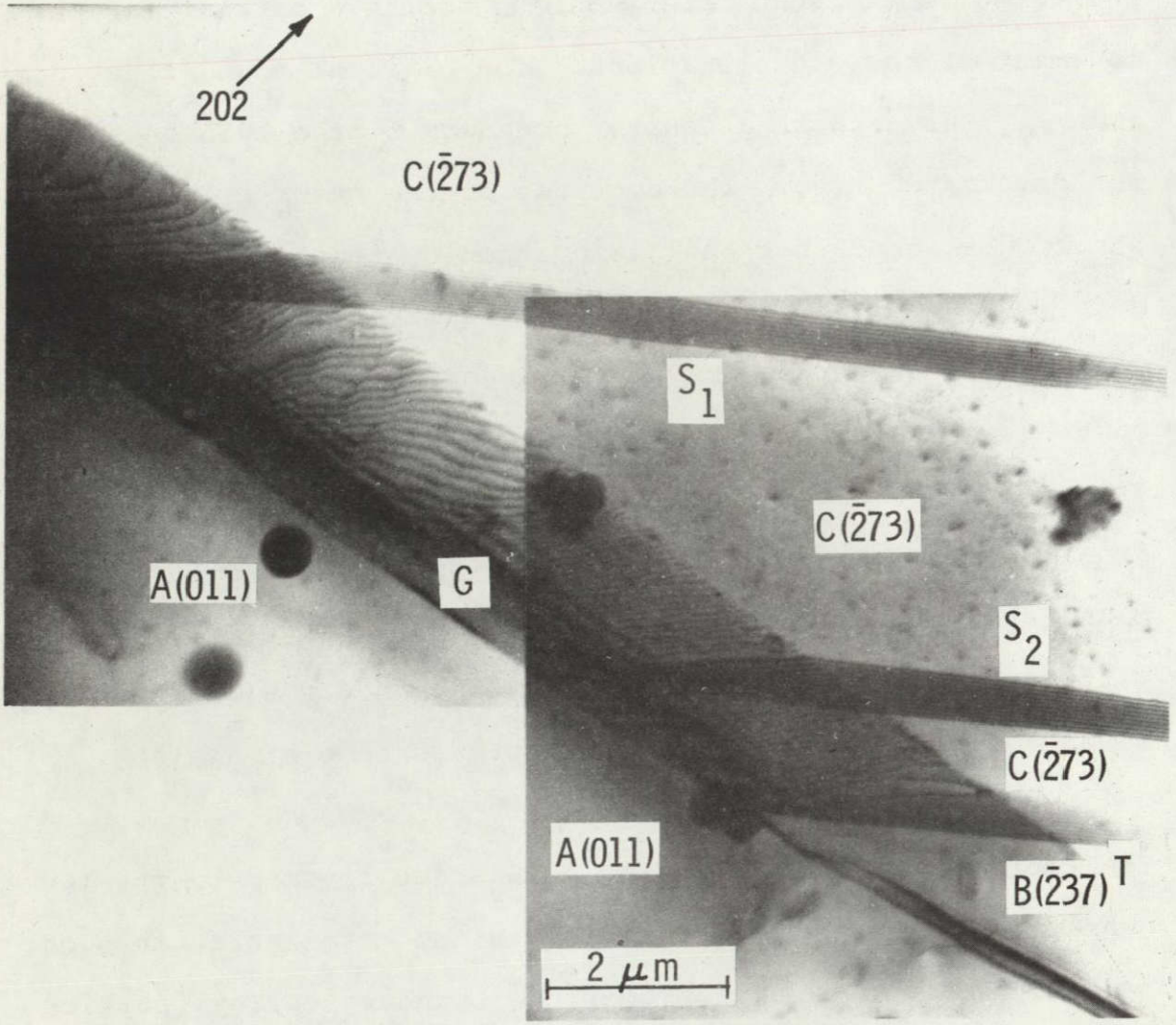

Fig. 21. TEM micrograph showing a grain boundary (g) formed by the (011) grain (A) and the ($\bar{2}73$) grain (C). The boundary contains a high density of dislocations. S_1 and S_2 are stacking faults. T is twin boundary.

2.2.4 DEFECTS IN CLASS IV RIBBONS

Silicon Carbide Dendrites and Inclusions

Silicon carbide inclusions lead to the formation of various kinds of grain boundaries. These boundaries can be twin boundaries, low-angle and/or high-angle grain boundaries.

An example of a SiC inclusion and its result on ribbon perfection is shown in Fig. 22a. In these figures, the inclusion is indicated at position I. As determined from the Kikuchi patterns shown in Figs. 22b,c, the surface orientation for grain A, is [211]. For grain B it is [255]. The boundary, B_{AB}, in the [01$\bar{1}$] direction, is a twin boundary with the (111) twin plane inclined 19.5 degrees to the surface of both grains. The surface orientation of grains C and D is about 1 degree off the [211] orientation of grain A. Thus, the boundaries, B_{AC} and B_{CD}, represent a low-angle grain boundary. The boundaries, B_{BC} and B_{BD} are high-angle grain boundaries. Such boundaries are not in fixed position relative to the lattice but tend to rotate during the growth of the ribbon. The rotation is accomplished by the generation of ledges and dislocations in the boundary plane.

3.0 DISCUSSION and CONCLUSIONS

The investigations presented leave no doubt that lifetime of

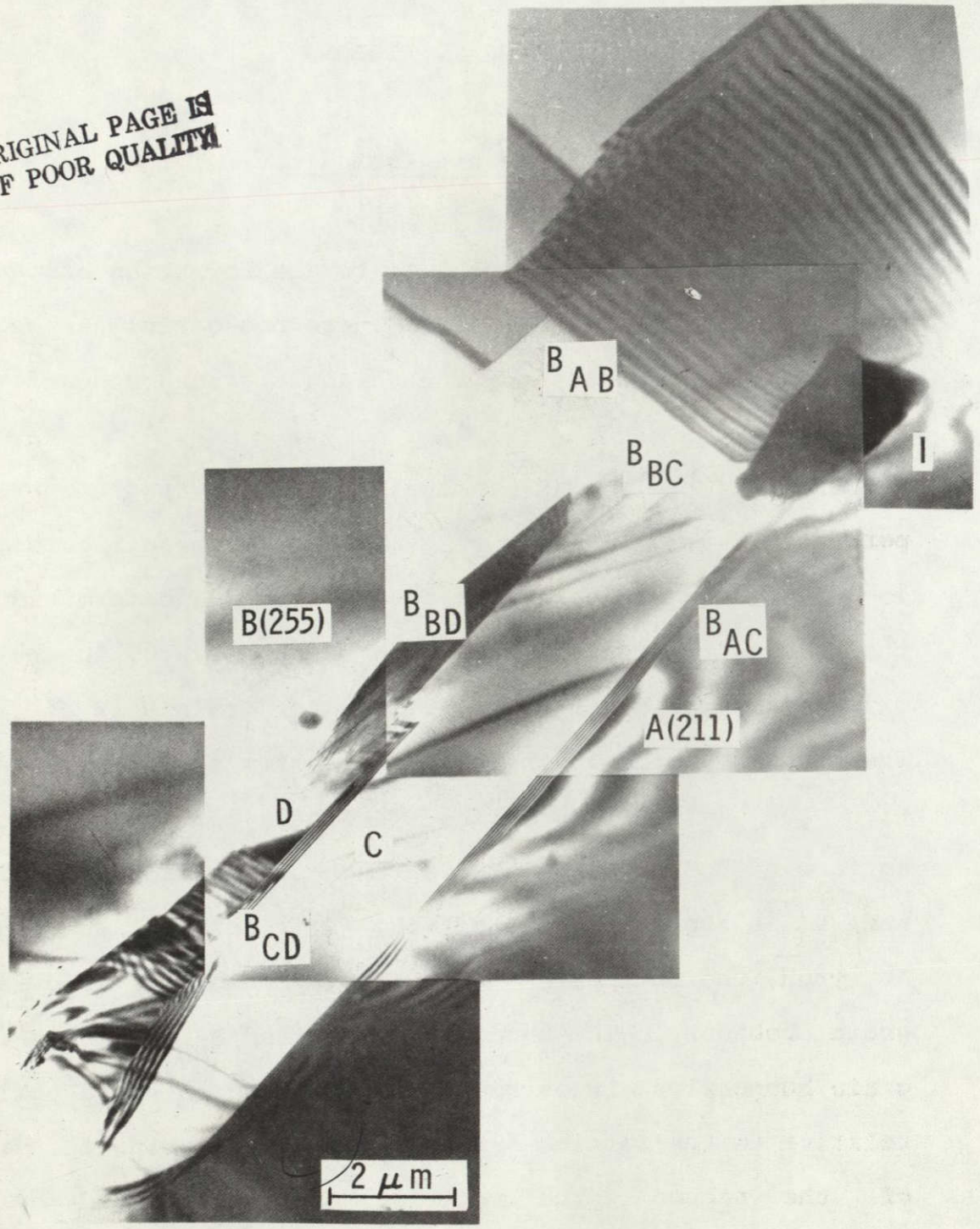

a

Fig. 22. (a) TEM micrographs showing that the inclusion of a SiC particle leads to the formation of various kinds of grain boundaries.

Fig. 22. (b) Electron diffraction pattern of grain A and (c) of grain B.

minority carriers and thus efficiency of solar cells is influenced to various degrees by crystal defects. This decrease in lifetime is essentially due to dislocations which can be present in densities larger than $10^6/cm^2$ either in dislocation clusters or in low and large angle grain boundaries. The lifetime problem is obviously compounded through chemical impurities which may be present preferentially along the dislocations. In this context it is of interest to know how carbon influences lifetime in silicon. To the best of our knowledge no information is available on this subject. However, it is known that carbon is incorporated substitutionally into silicon and thus leads to lattice constriction. An immediate result of this lattice constriction is "twinning" to relieve lattice strain. Twinning occurs profusely in CAST ribbons grown with carbon dies and presently we know of no way to eliminate it.

The electrical activity of the various defects observed in CAST ribbons is summarized in Table III. Accordingly, we differentiate between three groups of defects. In group I the defects are strongly active, in group II they are moderately active and the defects in group III are practically electrically non-active.

TABLE III. Electrical Activity of Crystal Defects in Ribbons

Group I Strongly Active	Group II Moderately Active	Group III Nonactive
Silicon carbide dendrites and inclusions	Multiple overlapping stacking faults	First order (coherent) Twins
Grain boundaries	Grown-in dislocations	Stacking Faults
Degenerated Twins, low-angle boundaries		
Dislocation bands		

If CAST ribbons are ever going to be a major contender in the race of low cost silicon for high efficiency photovoltaic energy conversion one must learn how to achieve "controlled" ribbon growth leading to the elimination of at least group I defects. By controlled ribbon growth we mean:

1. Control of the seeding phase
2. Control of the surface orientation
3. Control of carbon in solution
4. Control of silicon carbide formation
5. Control of impurities in ribbons

The subjects listed under 1 through 5 are obviously die dependent. Unfortunately, the most promising die material used so far is carbon or carbon coated with silicon carbide.

Considerable progress in ribbon perfection could be made through achieving control of seeding and thus control of surface orientation. So far, surface orientation of ribbons, even if obtained under steady state growth conditions, is at best fortuitous.

To obtain ribbon of controlled surface orientation must be a major goal of all future work in ribbon growth. Otherwise, we see little hope to eliminate grain boundaries and dislocation clusters during ribbon growth.

The reduction or total elimination of SiC particles is also an important goal of future ribbon growth development. Here we have made considerable progress. In this context clever die design leading to the high melt meniscus technique and the use of silicon carbide coated dies are helpful factors.

In conclusion we feel that ribbon growth through capillary action shaping remains a redoubtable task if it has to compete with the perfection level of Czochralski, Float Zone, or even web-dendrite crystals. Nevertheless, the

technique has an excellent potential, and "one" future breakthrough--most likely in the die material--could tip the balance in favor of CAST or similar techniques.

4.0 SUMMARY

Electrically active defects in CAST ribbons are identified as silicon carbide inclusions, high and low angle grain boundaries and high order twin boundaries, multiple stacking faults, dislocation bands and dislocations.

The electrical activity of grown-in dislocations due to their low density is only moderate. Grown-in dislocations are generated by thermal gradients associated with the growth technique. Their density varies from 3×10^3 to 5×10^5 per cm^2.

Dislocation bands with densities larger than 10^6 dislocation/cm^2 are strongly active. They consist of two groups of dislocations. One group is inclined towards the ribbon surface, while the other is almost parallel to ribbon surface in the growth direction. Both groups of dislocations have the same type of Burgers vectors, a/2 [011] and/or a/2 [101]. Dislocation networks are formed through the interaction of the two dislocations which leads to the formation of 90 degree dislocations.

Grain boundaries are strongly active. Their formation results mainly from foreign inclusions such as silicon carbide or from non-accommodation of crystal lattice planes during twinning. Such non-accommodation of crystal lattices occurs when two crystals of different preferred orientation, such as [011] and [211] orientations, join. The boundaries contain dislocations and/or ledges which are spaced approximately 0.1 μm apart.

First order (coherent) twins and stacking faults are nonactive. Their electrical activity increases as they degenerate into multiple overlapping faults and low-angle boundaries. The low-angle boundaries contain a high density of dislocations. The dislocation spacing ranges from 0.1 to 0.4 μm with an average of 0.2 μm. Degenerated twins act as dislocation sources.

5.0 ACKNOWLEDGMENT

Electron Microscopy support was given by Mr. H. Ilker, electrical characterization was done by Mr. C. P. Schneider, and EBIC measurements were made by R. Dessauer and E. Hearn.

6.0 REFERENCES

1. G. H. Schwuttke, K. H. Yang and R. Hezel, in Technical Report No. 5, JPL Contract No.: 954144, Sept. 1976.

2. W. R. Bottoms, D. Guterman and P. Roitman, J. Vac. Sci. Technol., 12, 1, 134, Jan./Feb., (1975).

3. R. Gevers, A. Art and S. Amelinckx, Phys. Status Solidi, 31, 363 (1963).

4. J. Friedel, "Dislocations," p. 181, Addison-Wesley Publishing Co., Reading, Mass. (1964).

5. L. E. Murr, Thin Solid Films, 4, 389 (1969.

6. F. L. Vogel, Jr., Acta Met., 3, 245 (1955).

7. S. O'Hara and G. H. Schwuttke, J. Appl. Phys., 36, 2475 (1965).

8. L. E. Murr, R. J. Horylev and W. N. Lin, Phil. Mag., 22, 515 (1970).

9. R. C. McDonald and A. J. Ardell, Phys. Stat. Sol. (a), 18, 407 (1973).

SIMULATED COMPARISON BETWEEN CZOCHRALSKI AND FLOAT-ZONE MATERIAL THROUGHPUT

by

A. Kran, T. F. Ciszek and G. H. Schwuttke

1.0 INTRODUCTION

There is little doubt that the ERDA programs on low-cost silicon solar cells and similar programs in other parts of the world are already impacting our present technologies to produce polysilicon and single crystal silicon. Presently, it is still an open question whether directly produced films or ribbons will be able to compete with conventional bulk material obtained from the large diameter Czochralski crystal.

In this context it is interesting to note that Float Zone material is never mentioned as a contender for low cost bulk material. Nevertheless, FZ crystals are already available up to 5 inches in diameter. The balance between advantages and drawbacks of the two basic growth methods (CZ and FZ) is mainly application, not economics, dependent. For solar cells, FZ material has the potential to yield solar cells of better efficiency as compared to those fabricated from CZ crystals.

Therefore, it is important to compare the capabilities of these two basic growth techniques for converting polycrystalline silicon into ingots of single-crystal material. A computer program simulates the potential weekly throughput of ingots. Processing parameters used are identical except for the values of the following parameters, which are peculiar to the crystal-growth technique: growth rate, crystal length, equipment setup and cool-down time, and the time required to melt the polycrystalline material.

2.0 EXAMPLES OF OUTPUT FROM COMPUTER PROGRAM

The following provides an example of the method used by the computer program for calculating crystal ingot throughput, and should be reviewed in conjunction with Table I.

For simplicity's sake, assume a 24-hour-a-day, seven-day work-week operation, a maximum crystal length of 100 cm, and a growth rate of 10 cm/hr. Hence we can grow one crystal every ten hours. Further assuming a setup time for each run of two hours and a crucible heat-up time of one hour, the first crystal will be grown Monday after 13 hours of operation. Three hours later we are ready to start the next run, which will be completed after the first two hours on Tuesday. Accordingly, we had two crystal starts on Monday, with a workday consisting of four hours of setup time, 2 hours of crucible heat-up time, and 18 hours of crystal

TABLE I. Algorithm for Analyzing Crystal Production

	Number of Crystals Pulled per Week and Time Distribution							
	Mon.	Tue.	Wed.	Thu.	Fri.	Sat.	Sun.	Total
Workday, Hours:	24.00	24.00	24.00	24.00	24.00	24.00	24.00	168.00
No. of Crystal starts	2.00	2.00	2.00	2.00	2.00	1.00	1.00	12.00
Last XTL, % of Max.							0.90	0.90
Daily setup time, hrs	4.00	4.00	4.00	4.00	4.00	3.00	3.00	26.00
Crucible heatup, hrs	2.00	2.00	2.00	2.00	2.00	1.00	1.00	13.00
Crystal pulling, hrs	18.00	18.00	18.00	18.00	18.00	20.00	19.00	129.00
Rem Unprod time, hrs								
Total Time, Hours	24.00	24.00	24.00	24.00	24.00	24.00	24.00	168.00

pulling time, a total of 24 hours. There is no wasted time in this case, since there is no termination of effort at the end of the workday, as there would be in a 16-hour work-day, for example.

On Tuesday, we also have two crystal starts, but we will not complete the second start until after four hours into Wednesday. On Wednesday we have a similar situation, but now require six hours of Thursday to complete Wednesday's second start. An additional two hour time shift, from six to eight hours, occurs on Thursday, and then completes the cycle by Friday. In other words, we complete setup and complete that run before the only start of the day occurs. One hour remains of Saturday to complete half of the setup for Sunday. During Sunday we make one complete run, and then have enough time for setup, heatup, and complete growing of 90% of the next crystal, giving us 1.9 crystals grown during that day.

2.1 Discussion of Material Processing Parameters

The study, through computer simulation, compares weekly throughput of 10-, 12-, and 15-cm-diameter Czochralski (CZO) and float-zone (FZ) ingots. Six cases (three each) are presented for two modes of factory operation: seven days,

24 hours per day and five days, 16 hours per day. For CZO technology, projections from previous reports (e.g., Quarterly Technical Progress Report Number 7, p. 43) are used. Future FZ technology is more difficult to predict because industry-wide manufacturing experience, as compared to CZO, is presently limited. A number of data points, however, are available. For instance, we know that several years back, 5.5 cm diameter FZ material was grown at 24 cm/hr, or 43% of theoretical maximum growth rate. FZ wafers up to 10 cm diameter are available today. 15 cm diameter capability exists at Wacker.

Accordingly, we have prepared three FZ technology projections (Table II), and chosen to use the most optimistic (last column) as the basis for this analysis. We project that technology can be developed to achieve a 24 cm/hr growth rate for 15 cm diameter crystals, the same as is practical for smaller diameter ingots. We recognize that this may require new ideas in equiment development so that problems, specifically created by rapid FZ growth, may be overcome. For instance, techniques must be found to more effectively remove the heat of fusion from the molten zone.

Increasing crystal diameter to 12 and then 15 cm, while holding actual growth rate constant at 24 cm/hr is an

TABLE II. Czochralski & Float Zone Technology Projection Matrix

Crystal Dia.,cm	Czochralski			Float-Zone								
				Projection 1			Projection 2			Projection 3		
	Actual Gr.Rt. cm/hr	Theor. Gr.Rt. % of Max	STATUS	Actual Gr.Rt. cm/hr	Theor. Gr.Rt % of Max	STATUS	Actual Gr.Rt. cm/hr	Theor. Gr.Rt. % of Max	STATUS	Actual Gr.Rt. cm/hr	Theor. Gr.Rt. % of Max	STATUS
5.0	10.00	19	A	24.00	43	A	24.00	43	A	24.0	43	A
10.0	9.83	25	A	9.83	25	A	15.73	40	C	24.0	61	O
12.0	14.30	40	C	14.30	40	C	16.15	45	C	24.0	67	O
15.0	12.80	40	O*	12.80	40	O*	16.05	50	O	24.0	75	O

LEGEND:

A - Achieved
C - Conservative Projection
O - Optimistic Projection
* - Activity & Capability Exists at Wacker

optimistic assumption, since it forecasts a 75% advance towards achieving the calculated maximum growth rate (from 43% for 5.5 cm diameter to 75% of maximum growth rate for 15 cm diameter crystals). However, it does not appear that much different from CZO, considering that CZO technology is commonly expected to increase from 25% to 40% of maximum growth rate, which represents a jump of 60%. The parameters discussed so far are listed in Table II.

Even though FZ ingots are inherently not easier to support than CZO ingots during the crystallization cycle, they are generally considerably longer. This fact is expected to remain true for the projected 12-15 cm diameter crystals. Accordingly, a crystal length of 75 cm for CZO and 150 cm for FZ was used throughout the study. Wacker has actually produced such long FZ crystal of up to 100 mm diameter.

Machine-availability time to grow crystal is reduced, in addition to random machine failure, by the time required to set up the crystal grower for the next run. This includes time to cool down the current run and such routine tasks as cleaning the puller and installing the next charge. The time required to perform these functions is estimated at 2 hours for CZO and 1 hour for FZ. Melting the polysilicon takes about 2.5 hours for CZO and 0.5 hour for FZ, because the latter technique, as the name implies, requires the

melting of only a narrow zone at a time. The other parameters are listed at the beginning of each of the 12 figures discussed next.

3.0 RESULTS OF STUDY

The results of this study are grouped into 12 figures as follows:

Seven-Day Week, 24-Hour-per-Day Operation

Fig. 1. Czochralski Technology - 10-cm diameter

- o List of Variables
- o Crystal Pulling Results
- o Number of Crystals Pulled and Time Distribution
- o Number of Crystals Pulled and Percentage Time Distribution

Fig. 2. Float-Zone Technology - 10-cm diameter

- o (same as above)

Fig. 3. Czochralski Technology - 12-cm diameter

(same as above)

Fig. 4. Float-Zone Technology - 12-cm diameter
(same as above)

Fig. 5. Czochralski Technology - 15-cm diameter
(same as above)

Fig. 6. Float-Zone Technology - 15-cm diameter
(same as above)

Five-Day Week, 16-Hour-per-Day Operation

Figs. 7-12 (same as above)

In general, factory working hours are established by management on a one-, two-, or three-shift basis with specified start-stop times. Production scheduling is built around these hours. For this study, two modes of operation were chosen: seven-day around-the-clock and five-days, 16 hours per day. No special consideration was given to such items as compatibility between working hours and machine cycle time, resulting (by accident) in excessive machine idle time for CZO during the second mode of operation. This can be seen, for example, in Fig. 7. Specified processing parameters are such that only one crystal start per day is possible, and a number of hours remain at the end

LIST OF VARIABLES AND THEIR CURRENT VALUES

CZOCHRALSKI TECHNIQUE

CRYSTAL DIAMETER (D),CM : 10
SEED AND TAIL CONES, ANGLE WITH C/L, DEGREES (AL) 30
GROWTH RATE (V2),CM/HR: 9.83
MAXIMUM CRYSTAL LENGTH, INCLUDING CONES (L), CM: 75
LAST CRYSTAL MUST BE 50 PERCENT OF MAX LENGTH TO BE STARTED
NO. OF HOURS WORKED EACH DAY OF THE WEEK (WD) : 24
NO. OF DAYS WORKED PER WEEK (DAYS) : 7
UNSCHEDULED DOWNTIME, PCT OF WORKDAY: 0
AVG SET-UP TIME (SU), HOURS: 2
AVG CRUCIBLE HEAT-UP TIME (WU), HOURS: 2.5

CRYSTAL PULLING

MAX LENGTH: 75 CM GROWTH RATE: 9.83 CM/HR · CZO TECHNIQUE· DIA, CM 10
WEEKLY VOLUME, CU-CM : 68368
WEEKLY AVG VOL,CU-CM/MIN : 6.78
WEEKLY WEIGHT, KG: 166.82

	MON.	TUE.	WED.	THU.	FRI.	SAT.	SUN.	TOTAL
WORKDAY, HOURS :	24.0	24.0	24.0	24.0	24.0	24.0	24.0	168.0
NO OF CRYSTAL STARTS	2.0	2.0	2.0	2.0	2.0	2.0	1.0	13.0
TOTAL LENGTH, METERS	1.5	1.5	1.5	1.5	1.5	1.5	1.3	10.3
VOLUME, CUBIC-CM	9967	9967	9967	9967	9967	9967	8565	68368
CUBIC-CM GROWN/MIN	6.9	6.9	6.9	6.9	6.9	6.9	5.9	

NUMBER OF CRYSTALS PULLED PER WEEK AND TIME DISTRIBUTION

	MON.	TUE.	WED.	THU.	FRI.	SAT.	SUN.	TOTAL
WORKDAY, HOURS :	24.0	24.0	24.0	24.0	24.0	24.0	24.0	168.0
NO OF CRYSTAL STARTS	2.0	2.0	2.0	2.0	2.0	2.0	1.0	13.0
LAST XTL,PRTN OF MAX							0.8	0.8
DAILY SETUP TIME,HRS	4.0	4.0	4.0	4.0	4.0	4.0	4.0	28.0
CRUCIBLE HEAT-UP,HRS	5.0	5.0	5.0	5.0	5.0	5.0	5.0	35.0
CRYSTAL PULLING, HRS	15.0	15.0	15.0	15.0	15.0	15.0	15.0	105.0
REM UNPROD TIME, HRS								
TOTAL TIME, HOURS	24.0	24.0	24.0	24.0	24.0	24.0	24.0	168.0

NUMBER OF CRYSTALS PULLED PER WEEK AND PERCENTAGE TIME DISTRIBUTION

	MON.	TUE.	WED.	THU.	FRI.	SAT.	SUN.	TOTAL
WORKDAY, HOURS :	24.0	24.0	24.0	24.0	24.0	24.0	24.0	168.0
NO OF CRYSTAL STARTS	2.0	2.0	2.0	2.0	2.0	2.0	1.0	13.0
LAST XTL,PCT OF MAX							0.8	0.8
DAILY SETUP TIME,PCT	16.7	16.7	16.7	16.7	16.7	16.7	16.7	16.7
CRUCIBLE HEAT-UP,PCT	20.8	20.8	20.8	20.8	20.8	20.8	20.8	20.8
CRYSTAL PULLING, PCT	62.5	62.5	62.5	62.5	62.5	62.5	62.5	62.5
REM UNPROD TIME, PCT								
TOTAL TIME, PERCENT	100.0	100.0	100.0	100.0	100.0	100.0	100.0	100.0

Fig. 1. Czochralski technology: 10-cm-diameter, 3-shift operation.

LIST OF VARIABLES AND THEIR CURRENT VALUES

FLOAT ZONE TECHNIQUE

CRYSTAL DIAMETER (D),CM : 10
SEED AND TAIL CONES, ANGLE WITH C/L, DEGREES (AL) 30
GROWTH RATE (V2),CM/HR: 24
MAXIMUM CRYSTAL LENGTH, INCLUDING CONES (L), CM: 150
LAST CRYSTAL MUST BE 50 PERCENT OF MAX LENGTH TO BE STARTED
NO. OF HOURS WORKED EACH DAY OF THE WEEK (WD) : 24
NO. OF DAYS WORKED PER WEEK (DAYS) : 7
UNSCHEDULED DOWNTIME, PCT OF WORKDAY: 0
AVG SET-UP TIME (SU), HOURS: 1
AVG CRUCIBLE HEAT-UP TIME (HU), HOURS: 0.5

CRYSTAL PULLING

MAX LENGTH: 150 CM GROWTH RATE: 24 CM/HR - FZ TECHNIQUE- DIA, CM 10
WEEKLY VOLUME, CU-CM : 234517
WEEKLY AVG VOL,CU-CM/MIN : 23.27
WEEKLY WEIGHT, KG: 572.22

	MON.	TUE.	WED.	THU.	FRI.	SAT.	SUN.	TOTAL
WORKDAY, HOURS :	24.0	24.0	24.0	24.0	24.0	24.0	24.0	168.0
NO OF CRYSTAL STARTS	3.0	4.0	3.0	3.0	3.0	3.0	2.6	21.6
TOTAL LENGTH, METERS	4.5	6.0	4.5	4.5	4.5	4.5	3.9	32.4
VOLUME, CUBIC-CM	32622	43496	32622	32622	32622	32622	27910	234517
CUBIC-CM GROWN/MIN	22.7	30.2	22.7	22.7	22.7	22.7	19.4	

NUMBER OF CRYSTALS PULLED PER WEEK AND TIME DISTRIBUTION

	MON.	TUE.	WED.	THU.	FRI.	SAT.	SUN.	TOTAL
WORKDAY, HOURS :	24.0	24.0	24.0	24.0	24.0	24.0	24.0	168.0
NO OF CRYSTAL STARTS	3.0	4.0	3.0	3.0	3.0	3.0	2.0	21.0
LAST XTL,PRTN OF MAX							0.6	0.6
DAILY SETUP TIME,HRS	3.8	3.3	3.0	3.0	3.0	3.0	3.0	22.0
CRUCIBLE HEAT-UP,HRS	1.5	2.0	1.5	1.5	1.5	1.5	1.5	11.0
CRYSTAL PULLING, HRS	18.8	18.8	19.5	19.5	19.5	19.5	19.5	135.0
REM UNPROD TIME, HRS								
TOTAL TIME, HOURS	24.0	24.0	24.0	24.0	24.0	24.0	24.0	168.0

NUMBER OF CRYSTALS PULLED PER WEEK AND PERCENTAGE TIME DISTRIBUTION

	MON.	TUE.	WED.	THU.	FRI.	SAT.	SUN.	TOTAL
WORKDAY, HOURS :	24.0	24.0	24.0	24.0	24.0	24.0	24.0	168.0
NO OF CRYSTAL STARTS	3.0	4.0	3.0	3.0	3.0	3.0	2.0	21.0
LAST XTL,PCT OF MAX							0.6	0.6
DAILY SETUP TIME,PCT	15.6	13.5	12.5	12.5	12.5	12.5	12.5	13.1
CRUCIBLE HEAT-UP,PCT	6.3	8.3	6.3	6.3	6.3	6.3	6.3	6.5
CRYSTAL PULLING, PCT	78.1	78.1	81.2	81.2	81.2	81.2	81.2	80.4
REM UNPROD TIME, PCT								
TOTAL TIME, PERCENT	100.0	100.0	100.0	100.0	100.0	100.0	100.0	100.0

Fig. 2. Float-zone technology: 10-cm-diameter, 3-shift operation.

LIST OF VARIABLES AND THEIR CURRENT VALUES

CZOCHRALSKI TECHNIQUE

```
CRYSTAL DIAMETER (D),CM : 12
SEED AND TAIL CONES, ANGLE WITH C/L, DEGREES (AL) 30
GROWTH RATE (V2),CM/HR: 14.3
MAXIMUM CRYSTAL LENGTH, INCLUDING CONES (L), CM: 75
LAST CRYSTAL MUST BE 50 PERCENT OF MAX LENGTH TO BE STARTED
NO. OF HOURS WORKED EACH DAY OF THE WEEK (WD) : 24
NO. OF DAYS WORKED PER WEEK (DAYS) : 7
UNSCHEDULED DOWNTIME, PCT OF WORKDAY: 0
AVG SET-UP TIME (SU), HOURS: 2
AVG CRUCIBLE HEAT-UP TIME (HU), HOURS: 2.5
```

CRYSTAL PULLING

```
MAX LENGTH: 75 CM  GROWTH RATE: 14.3 CM/HR - CZO TECHNIQUE- DIA, CM 12
WEEKLY VOLUME, CU-CM : 117558
WEEKLY AVG VOL,CU-CM/MIN :   11.66
WEEKLY WEIGHT, KG:      286.84
```

	MON.	TUE.	WED.	THU.	FRI.	SAT.	SUN.	TOTAL
WORKDAY, HOURS :	24.0	24.0	24.0	24.0	24.0	24.0	24.0	168.0
NO OF CRYSTAL STARTS	3.0	2.0	2.0	3.0	2.0	3.0	2.0	17.0
TOTAL LENGTH, METERS	2.3	1.5	1.5	2.3	1.5	2.3	1.5	12.8
VOLUME, CUBIC-CM	20746	13830	13830	20746	13830	20746	13830	117558
CUBIC-CM GROWN/MIN	14.4	9.6	9.6	14.4	9.6	14.4	9.6	

NUMBER OF CRYSTALS PULLED PER WEEK AND TIME DISTRIBUTION

	MON.	TUE.	WED.	THU.	FRI.	SAT.	SUN.	TOTAL
WORKDAY, HOURS :	24.0	24.0	24.0	24.0	24.0	24.0	24.0	168.0
NO OF CRYSTAL STARTS	3.0	2.0	2.0	3.0	2.0	3.0	2.0	17.0
LAST XTL,PRTN OF MAX								
DAILY SETUP TIME,HRS	6.0	4.0	6.0	4.0	6.0	4.0	4.0	34.0
CRUCIBLE HEAT-UP,HRS	7.5	5.0	6.8	5.7	6.1	6.4	5.0	42.5
CRYSTAL PULLING, HRS	10.5	15.0	11.2	14.3	11.9	13.6	12.7	89.2
REM UNPROD TIME, HRS							2.3	2.3
TOTAL TIME, HOURS	24.0	24.0	24.0	24.0	24.0	24.0	24.0	168.0

NUMBER OF CRYSTALS PULLED PER WEEK AND PERCENTAGE TIME DISTRIBUTION

	MON.	TUE.	WED.	THU.	FRI.	SAT.	SUN.	TOTAL
WORKDAY, HOURS :	24.0	24.0	24.0	24.0	24.0	24.0	24.0	168.0
NO OF CRYSTAL STARTS	3.0	2.0	2.0	3.0	2.0	3.0	2.0	17.0
LAST XTL,PCT OF MAX								
DAILY SETUP TIME,PCT	25.0	16.7	25.0	16.7	25.0	16.7	16.7	20.2
CRUCIBLE HEAT-UP,PCT	31.3	20.8	28.3	23.8	25.3	26.8	20.8	25.3
CRYSTAL PULLING, PCT	43.8	62.5	46.7	59.5	49.7	56.5	52.8	53.1
REM UNPROD TIME, PCT							9.7	1.4
TOTAL TIME, PERCENT	100.0	100.0	100.0	100.0	100.0	100.0	100.0	100.0

Fig. 3. Czochralski technology: 12-cm-diameter, 3-shift operation.

LIST OF VARIABLES AND THEIR CURRENT VALUES

FLOAT ZONE TECHNIQUE

CRYSTAL DIAMETER (D),CM : 12
SEED AND TAIL CONES, ANGLE WITH C/L, DEGREES (AL) 30
GROWTH RATE (V2),CM/HR: 24
MAXIMUM CRYSTAL LENGTH, INCLUDING CONES (L), CM: 150
LAST CRYSTAL MUST BE 50 PERCENT OF MAX LENGTH TO BE STARTED
NO. OF HOURS WORKED EACH DAY OF THE WEEK (WD) : 24
NO. OF DAYS WORKED PER WEEK (DAYS) : 7
UNSCHEDULED DOWNTIME, PCT OF WORKDAY: 0
AVG SET-UP TIME (SU), HOURS: 1
AVG CRUCIBLE HEAT-UP TIME (HU), HOURS: 0.5

CRYSTAL PULLING

MAX LENGTH: 150 CM GROWTH RATE: 24 CM/HR · FZ TECHNIQUE· DIA, CM 12
WEEKLY VOLUME, CU-CM : 331959
WEEKLY AVG VOL,CU-CM/MIN : 32.93
WEEKLY WEIGHT, KG: 809.98

	MON.	TUE.	WED.	THU.	FRI.	SAT.	SUN.	TOTAL
WORKDAY, HOURS :	24.0	24.0	24.0	24.0	24.0	24.0	24.0	168.0
NO OF CRYSTAL STARTS	3.0	4.0	3.0	3.0	3.0	3.0	2.6	21.6
TOTAL LENGTH, METERS	4.5	6.0	4.5	4.5	4.5	4.5	3.9	32.4
VOLUME, CUBIC-CM	46192	61590	46192	46192	46192	46192	39407	331959

NUMBER OF CRYSTALS PULLED PER WEEK AND TIME DISTRIBUTION

	MON.	TUE.	WED.	THU.	FRI.	SAT.	SUN.	TOTAL
WORKDAY, HOURS :	24.0	24.0	24.0	24.0	24.0	24.0	24.0	168.0
NO OF CRYSTAL STARTS	3.0	4.0	3.0	3.0	3.0	3.0	2.0	21.0
LAST XTL,PRTN OF MAX							0.6	0.6
DAILY SETUP TIME,HRS	3.8	3.3	3.0	3.0	3.0	3.0	3.0	22.0
CRUCIBLE HEAT-UP,HRS	1.5	2.0	1.5	1.5	1.5	1.5	1.5	11.0
CRYSTAL PULLING, HRS	18.8	18.8	19.5	19.5	19.5	19.5	19.5	135.0
REM UNPROD TIME, HRS								
TOTAL TIME, HOURS	24.0	24.0	24.0	24.0	24.0	24.0	24.0	168.0

NUMBER OF CRYSTALS PULLED PER WEEK AND PERCENTAGE TIME DISTRIBUTION

	MON.	TUE.	WED.	THU.	FRI.	SAT.	SUN.	TOTAL
WORKDAY, HOURS :	24.0	24.0	24.0	24.0	24.0	24.0	24.0	168.0
NO OF CRYSTAL STARTS	3.0	4.0	3.0	3.0	3.0	3.0	2.0	21.0
LAST XTL,PCT OF MAX							0.6	0.6
DAILY SETUP TIME,PCT	15.6	13.5	12.5	12.5	12.5	12.5	12.5	13.1
CRUCIBLE HEAT-UP,PCT	6.3	8.3	6.3	6.3	6.3	6.3	6.3	6.5
CRYSTAL PULLING, PCT	78.1	78.1	81.2	81.2	81.2	81.2	81.2	80.4
REM UNPROD TIME, PCT								
TOTAL TIME, PERCENT	100.0	100.0	100.0	100.0	100.0	100.0	100.0	100.0

Fig. 4. Float-zone technology: 12-cm-diameter, 3-shift operation

LIST OF VARIABLES AND THEIR CURRENT VALUES

CZOCHRALSKI TECHNIQUE

CRYSTAL DIAMETER (D),CM : 15
SEED AND TAIL CONES, ANGLE WITH C/L, DEGREES (AL) 30
GROWTH RATE (V2),CM/HR: 12.8
MAXIMUM CRYSTAL LENGTH, INCLUDING CONES (L), CM: 75
LAST CRYSTAL MUST BE 50 PERCENT OF MAX LENGTH TO BE STARTED
NO. OF HOURS WORKED EACH DAY OF THE WEEK (HD) : 24
NO. OF DAYS WORKED PER WEEK (DAYS) : 7
UNSCHEDULED DOWNTIME, PCT OF WORKDAY: 0
AVG SET-UP TIME (SU), HOURS: 2
AVG CRUCIBLE HEAT-UP TIME (HU), HOURS: 2.5

CRYSTAL PULLING

MAX LENGTH: 75 CM GROWTH RATE: 12.8 CM/HR · CZO TECHNIQUE· DIA, CM 15
WEEKLY VOLUME, CU-CM : 163085
WEEKLY AVG VOL,CU-CM/MIN : 16.18
WEEKLY WEIGHT, KG: 397.93

	MON.	TUE.	WED.	THU.	FRI.	SAT.	SUN.	TOTAL
WORKDAY, HOURS :	24.0	24.0	24.0	24.0	24.0	24.0	24.0	168.0
NO OF CRYSTAL STARTS	2.0	3.0	2.0	2.0	3.0	2.0	2.0	16.0
TOTAL LENGTH, METERS	1.5	2.3	1.5	1.5	2.3	1.5	1.5	12.0
VOLUME, CUBIC-CM	20386	30578	20386	20386	30578	20386	20386	163085
CUBIC-CM GROWN/MIN	14.2	21.2	14.2	14.2	21.2	14.2	14.2	

NUMBER OF CRYSTALS PULLED PER WEEK AND TIME DISTRIBUTION

	MON.	TUE.	WED.	THU.	FRI.	SAT.	SUN.	TOTAL
WORKDAY, HOURS :	24.0	24.0	24.0	24.0	24.0	24.0	24.0	168.0
NO OF CRYSTAL STARTS	2.0	3.0	2.0	2.0	3.0	2.0	2.0	16.0
LAST XTL.PRTN OF MAX								
DAILY SETUP TIME,HRS	6.0	4.0	4.0	6.0	4.0	4.0	4.0	32.0
CRUCIBLE HEAT-UP,HRS	6.3	6.2	5.0	5.8	6.7	5.0	5.0	40.0
CRYSTAL PULLING, HRS	11.7	13.8	15.0	12.2	13.3	15.0	12.7	93.7
REM UNPROD TIME, HRS							2.3	2.3
TOTAL TIME, HOURS	24.0	24.0	24.0	24.0	24.0	24.0	24.0	168.0

NUMBER OF CRYSTALS PULLED PER WEEK AND PERCENTAGE TIME DISTRIBUTION

	MON.	TUE.	WED.	THU.	FRI.	SAT.	SUN.	TOTAL
WORKDAY, HOURS :	24.0	24.0	24.0	24.0	24.0	24.0	24.0	168.0
NO OF CRYSTAL STARTS	2.0	3.0	2.0	2.0	3.0	2.0	2.0	16.0
LAST XT' .PCT OF MAX								
DAILY SETUP TIME,PCT	25.0	16.7	16.7	25.0	16.7	16.7	16.7	19.0
CRUCIBLE HEAT-UP,PCT	26.2	25.9	20.8	24.0	28.1	20.8	20.8	23.8
CRYSTAL PULLING, PCT	48.8	57.4	62.5	51.0	55.3	62.5	53.1	55.8
REM UNPROD TIME, PCT							9.4	1.3
TOTAL TIME, PERCENT	100.0	100.0	100.0	100.0	100.0	100.0	100.0	100.0

Fig. 5. Czochralski technology: 15-cm-diameter, 3-shift operation.

LIST OF VARIABLES AND THEIR CURRENT VALUES

FLOAT ZONE TECHNIQUE

CRYSTAL DIAMETER (D),CM : 15
SEED AND TAIL CONES, ANGLE WITH C/L, DEGREES (AL) 30
GROWTH RATE (V2),CM/HR: 24
MAXIMUM CRYSTAL LENGTH, INCLUDING CONES (L), CM: 150
LAST CRYSTAL MUST BE 50 PERCENT OF MAX LENGTH TO BE STARTED
NO. OF HOURS WORKED EACH DAY OF THE WEEK (WD) : 24
NO. OF DAYS WORKED PER WEEK (DAYS) : 7
UNSCHEDULED DOWNTIME, PCT OF WORKDAY: 0
AVG SET-UP TIME (SU), HOURS: 1
AVG CRUCIBLE HEAT-UP TIME (HU), HOURS: 0.5

CRYSTAL PULLING

MAX LENGTH: 150 CM GROWTH RATE: 24 CM/HR - FZ TECHNIQUE- DIA. CM 15
WEEKLY VOLUME, CU-CM : 505218
WEEKLY AVG VOL.CU-CM/MIN : 50.12
WEEKLY WEIGHT, KG: 1232.73

	MON.	TUE.	WED.	THU.	FRI.	SAT.	SUN.	TOTAL
WORKDAY, HOURS :	24.0	24.0	24.0	24.0	24.0	24.0	24.0	168.0
NO OF CRYSTAL STARTS	3.0	4.0	3.0	3.0	3.0	3.0	2.6	21.6
TOTAL LENGTH, METERS	4.5	6.0	4.5	4.5	4.5	4.5	3.9	32.4
VOLUME, CUBIC-CM	70339	93786	70339	70339	70339	70339	59736	505218
CUBIC-CM GROWN/MIN	48.8	65.1	48.8	48.8	48.8	48.8	41.5	

NUMBER OF CRYSTALS PULLED PER WEEK AND TIME DISTRIBUTION

	MON.	TUE.	WED.	THU.	FRI.	SAT.	SUN.	TOTAL
WORKDAY, HOURS :	24.0	24.0	24.0	24.0	24.0	24.0	24.0	168.0
NO OF CRYSTAL STARTS	3.0	4.0	3.0	3.0	3.0	3.0	2.0	21.0
LAST XTL.PRTN OF MAX							0.6	0.6
DAILY SETUP TIME,HRS	3.0	3.3	3.0	3.0	3.0	3.0	3.0	22.0
CRUCIBLE HEAT-UP,HRS	1.5	2.0	1.5	1.5	1.5	1.5	1.5	11.0
CRYSTAL PULLING, HRS	18.8	18.8	19.5	19.5	19.5	19.5	19.5	135.0
REM UNPROD TIME, HRS								
TOTAL TIME, HOURS	24.0	24.0	24.0	24.0	24.0	24.0	24.0	168.0

NUMBER OF CRYSTALS PULLED PER WEEK AND PERCENTAGE TIME DISTRIBUTION

	MON.	TUE.	WED.	THU.	FRI.	SAT.	SUN.	TOTAL
WORKDAY, HOURS :	24.0	24.0	24.0	24.0	24.0	24.0	24.0	168.0
NO OF CRYSTAL STARTS	3.0	4.0	3.0	3.0	3.0	3.0	2.0	21.0
LAST XTL.PCT OF MAX							0.6	0.6
DAILY SETUP TIME,PCT	15.6	13.5	12.5	12.5	12.5	12.5	12.5	13.1
CRUCIBLE HEAT-UP,PCT	6.3	8.3	6.3	6.3	6.3	6.3	6.3	6.5
CRYSTAL PULLING, PCT	78.1	78.1	81.2	81.2	81.2	81.2	81.2	80.4
REM UNPROD TIME, PCT								
TOTAL TIME, PERCENT	100.0	100.0	100.0	100.0	100.0	100.0	100.0	100.0

Fig. 6. Float-zone technology: 15-cm-diameter, 3-shift operation.

LIST OF VARIABLES AND THEIR CURRENT VALUES

CZOCHRALSKI TECHNIQUE

CRYSTAL DIAMETER (D),CM : 10
SEED AND TAIL CONES, ANGLE WITH C/L, DEGREES (AL) 30
GROWTH RATE (V2),CM/HR: 9.83
MAXIMUM CRYSTAL LENGTH, INCLUDING CONES (L), CM: 75
LAST CRYSTAL MUST BE 50 PERCENT OF MAX LENGTH TO BE STARTED
NO. OF HOURS WORKED EACH DAY OF THE WEEK (WD) : 16
NO. OF DAYS WORKED PER WEEK (DAYS) : 5
UNSCHEDULED DOWNTIME, PCT OF WORKDAY: 0
AVG SET-UP TIME (SU), HOURS: 2
AVG CRUCIBLE HEAT-UP TIME (WU), HOURS: 2.5

CRYSTAL PULLING

MAX LENGTH: 75 CM GROWTH RATE: 9.83 CM/HR · CZO TECHNIQUE· DIA, CM 10
WEEKLY VOLUME, CU-CM : 24918
WEEKLY AVG VOL,CU-CM/MIN : 5.19
WEEKLY WEIGHT, KG: 60.80

	MON.	TUE.	WED.	THU.	FRI.	SAT.	SUN.	TOTAL
WORKDAY, HOURS :	16.0	16.0	16.0	16.0	16.0			80.0
NO OF CRYSTAL STARTS	1.0	1.0	1.0	1.0	1.0			5.0
TOTAL LENGTH, METERS	0.8	0.8	0.8	0.8	0.8			3.8
VOLUME, CUBIC-CM	4984	4984	4984	4984	4984			24918
CUBIC-CM GROWN/MIN	5.2	5.2	5.2	5.2	5.2			

NUMBER OF CRYSTALS PULLED PER WEEK AND TIME DISTRIBUTION

	MON.	TUE.	WED.	THU.	FRI.	SAT.	SUN.	TOTAL
WORKDAY, HOURS :	16.0	16.0	16.0	16.0	16.0			80.0
NO OF CRYSTAL STARTS LAST XTL,PRTN OF MAX	1.0	1.0	1.0	1.0	1.0			5.0
DAILY SETUP TIME,HRS	4.0	2.0	2.0	2.0				10.0
CRUCIBLE HEAT-UP,HRS	2.5	2.5	2.5	2.5	2.5			12.5
CRYSTAL PULLING, HRS	7.6	7.6	7.6	7.6	7.6			38.1
REM UNPROD TIME, HRS	1.9	3.9	3.9	3.9	5.9			19.4
TOTAL TIME, HOURS	16.0	16.0	16.0	16.0	16.0			80.0

NUMBER OF CRYSTALS PULLED PER WEEK AND PERCENTAGE TIME DISTRIBUTION

	MON.	TUE.	WED.	THU.	FRI.	SAT.	SUN.	TOTAL
WORKDAY, HOURS :	16.0	16.0	16.0	16.0	16.0			80.0
NO OF CRYSTAL STARTS LAST XTL,PCT OF MAX	1.0	1.0	1.0	1.0	1.0			5.0
DAILY SETUP TIME,PCT	25.0	12.5	12.5	12.5				12.5
CRUCIBLE HEAT-UP,PCT	15.6	15.6	15.6	15.6	15.6			15.6
CRYSTAL PULLING, PCT	47.7	47.7	47.7	47.7	47.7			47.7
REM UNPROD TIME, PCT	11.7	24.2	24.2	24.2	36.7			24.2
TOTAL TIME, PERCENT	100.0	100.0	100.0	100.0	100.0			100.0

Fig. 7. Czochralski technology: 10-cm-diameter, 2-shift operation.

LIST OF VARIABLES AND THEIR CURRENT VALUES

FLOAT ZONE TECHNIQUE

CRYSTAL DIAMETER (D),CM : 10
SEED AND TAIL CONES, ANGLE WITH C/L, DEGREES (AL) 30
GROWTH RATE (V2),CM/HR: 24
MAXIMUM CRYSTAL LENGTH, INCLUDING CONES (L), CM: 150
LAST CRYSTAL MUST BE 50 PERCENT OF MAX LENGTH TO BE STARTED
NO. OF HOURS WORKED EACH DAY OF THE WEEK (HD) : 16
NO. OF DAYS WORKED PER WEEK (DAYS) : 5
UNSCHEDULED DOWNTIME, PCT OF WORKDAY: 0
AVG SET-UP TIME (SU), HOURS: 1
AVG CRUCIBLE HEAT-UP TIME (HU), HOURS: 0.5

CRYSTAL PULLING

MAX LENGTH: 150 CM GROWTH RATE: 24 CM/HR · FZ TECHNIQUE· DIA, CM 10
WEEKLY VOLUME, CU-CM : 108741
WEEKLY AVG VOL,CU-CM/MIN : 22.65
WEEKLY WEIGHT, KG: 265.33

	MON.	TUE.	WED.	THU.	FRI.	SAT.	SUN.	TOTAL
WORKDAY, HOURS :	16.0	16.0	16.0	16.0	16.0			80.0
NO OF CRYSTAL STARTS	2.0	2.0	2.0	2.0	2.0			10.0
TOTAL LENGTH, METERS	3.0	3.0	3.0	3.0	3.0			15.0
VOLUME, CUBIC-CM	21748	21748	21748	21748	21748			108741
CUBIC-CM GROWN/MIN	22.7	22.7	22.7	22.7	22.7			

NUMBER OF CRYSTALS PULLED PER WEEK AND TIME DISTRIBUTION

	MON.	TUE.	WED.	THU.	FRI.	SAT.	SUN.	TOTAL
WORKDAY, HOURS :	16.0	16.0	16.0	16.0	16.0			80.0
NO OF CRYSTAL STARTS	2.0	2.0	2.0	2.0	2.0			10.0
LAST XTL,PRTN OF MAX								
DAILY SETUP TIME,HRS	2.5	2.5	2.0	2.0	1.0			10.0
CRUCIBLE HEAT-UP,HRS	1.0	1.0	1.0	1.0	1.0			5.0
CRYSTAL PULLING, HRS	12.5	12.5	12.5	12.5	12.5			62.5
REM UNPROD TIME, HRS			0.5	0.5	1.5			2.5
TOTAL TIME, HOURS	16.0	16.0	16.0	16.0	16.0			80.0

NUMBER OF CRYSTALS PULLED PER WEEK AND PERCENTAGE TIME DISTRIBUTION

	MON.	TUE.	WED.	THU.	FRI.	SAT.	SUN.	TOTAL
WORKDAY, HOURS :	16.0	16.0	16.0	16.0	16.0			80.0
NO OF CRYSTAL STARTS	2.0	2.0	2.0	2.0	2.0			10.0
LAST XTL,PCT OF MAX								
DAILY SETUP TIME,PCT	15.6	15.6	12.5	12.5	6.3			12.5
CRUCIBLE HEAT-UP,PCT	6.3	6.3	6.3	6.3	6.3			6.3
CRYSTAL PULLING, PCT	78.1	78.1	78.1	78.1	78.1			78.1
REM UNPROD TIME, PCT			3.1	3.1	9.4			3.1
TOTAL TIME, PERCENT	100.0	100.0	100.0	100.0	100.0			100.0

Fig. 8. Float-zone technology: 10-cm-diameter, 2-shift operation.

LIST OF VARIABLES AND THEIR CURRENT VALUES

CZOCHRALSKI TECHNIQUE

```
CRYSTAL DIAMETER (D),CM : 12
SEED AND TAIL CONES, ANGLE WITH C/L, DEGREES (AL) 30
GROWTH RATE (V2),CM/HR: 14.3
MAXIMUM CRYSTAL LENGTH, INCLUDING CONES (L), CM: 75
LAST CRYSTAL MUST BE 50 PERCENT OF MAX LENGTH TO BE STARTED
NO. OF HOURS WORKED EACH DAY OF THE WEEK (WD) : 16
NO. OF DAYS WORKED PER WEEK (DAYS) : 5
UNSCHEDULED DOWNTIME, PCT OF WORKDAY: 0
AVG SET-UP TIME (SU), HOURS: 2
AVG CRUCIBLE HEAT-UP TIME (HU), HOURS: 2.5
```

CRYSTAL PULLING

```
MAX LENGTH: 75 CM  GROWTH RATE: 14.3 CM/HR · CZO TECHNIQUE· DIA, CM 12
WEEKLY VOLUME, CU-CM :  43588
WEEKLY AVG VOL,CU-CM/MIN :     9.08
WEEKLY WEIGHT, KG:      106.36
```

	MON.	TUE.	WED.	THU.	FRI.	SAT.	SUN.	TOTAL
WORKDAY, HOURS :	16.0	16.0	16.0	16.0	16.0			80.0
NO OF CRYSTAL STARTS	1.0	1.7	1.0	1.7	1.0			6.4
TOTAL LENGTH, METERS	0.8	1.3	0.8	1.3	0.8			4.8
VOLUME, CUBIC-CM	6915	11421	6915	11421	6915			43588
CUBIC-CM GROWN/MIN	7.2	11.9	7.2	11.9	7.2			

NUMBER OF CRYSTALS PULLED PER WEEK AND TIME DISTRIBUTION

	MON.	TUE.	WED.	THU.	FRI.	SAT.	SUN.	TOTAL
WORKDAY, HOURS :	16.0	16.0	16.0	16.0	16.0			80.0
NO OF CRYSTAL STARTS	1.0	1.0	1.0	1.0	1.0			5.0
LAST XTL,PRTN OF MAX		0.7		0.7				1.4
DAILY SETUP TIME,HRS	4.0	2.0	4.0	2.0	2.0			14.0
CRUCIBLE HEAT-UP,HRS	2.5	5.0	2.5	5.0	2.5			17.5
CRYSTAL PULLING, HRS	5.2	9.0	5.2	9.0	5.2			33.7
REM UNPROD TIME, HRS	4.3		4.3		6.3			14.8
TOTAL TIME, HOURS	16.0	16.0	16.0	16.0	16.0			80.0

NUMBER OF CRYSTALS PULLED PER WEEK AND PERCENTAGE TIME DISTRIBUTION

	MON.	TUE.	WED.	THU.	FRI.	SAT.	SUN.	TOTAL
WORKDAY, HOURS :	16.0	16.0	16.0	16.0	16.0			80.0
NO OF CRYSTAL STARTS	1.0	1.0	1.0	1.0	1.0			5.0
LAST XTL,PCT OF MAX		0.7		0.7				1.4
DAILY SETUP TIME,PCT	25.0	12.5	25.0	12.5	12.5			17.5
CRUCIBLE HEAT-UP,PCT	15.6	31.3	15.6	31.3	15.6			21.9
CRYSTAL PULLING, PCT	32.8	56.3	32.8	56.3	32.8			42.2
REM UNPROD TIME, PCT	26.6		26.6		39.1			18.5
TOTAL TIME, PERCENT	100.0	100.0	100.0	100.0	100.0			100.0

Fig. 9. Czochralski technology: 12-cm-diameter, 2-shift operation.

LIST OF VARIABLES AND THEIR CURRENT VALUES

FLOAT ZONE TECHNIQUE

CRYSTAL DIAMETER (D),CM : 12
SEED AND TAIL CONES, ANGLE WITH C/L, DEGREES (AL) 30
GROWTH RATE (V2),CM/HR: 24
MAXIMUM CRYSTAL LENGTH, INCLUDING CONES (L), CM: 150
LAST CRYSTAL MUST BE 50 PERCENT OF MAX LENGTH TO BE STARTED
NO. OF HOURS WORKED EACH DAY OF THE WEEK (HD) : 16
NO. OF DAYS WORKED PER WEEK (DAYS) : 5
UNSCHEDULED DOWNTIME, PCT OF WORKDAY: 0
AVG SET-UP TIME (SU), HOURS: 1
AVG CRUCIBLE HEAT-UP TIME (HU), HOURS: 0.5

CRYSTAL PULLING

MAX LENGTH: 150 CM GROWTH RATE: 24 CM/HR · FZ TECHNIQUE· DIA, CM 12
WEEKLY VOLUME, CU-CM : 153975
WEEKLY AVG VOL,CU-CM/MIN : 32.08
WEEKLY WEIGHT, KG: 375.70

	MON.	TUE.	WED.	THU.	FRI.	SAT.	SUN.	TOTAL
WORKDAY, HOURS :	16.0	16.0	16.0	16.0	16.0			80.0
NO OF CRYSTAL STARTS	2.0	2.0	2.0	2.0	2.0			10.0
TOTAL LENGTH, METERS	3.0	3.0	3.0	3.0	3.0			15.0
VOLUME, CUBIC-CM	30795	30795	30795	30795	30795			153975
CUBIC-CM GROWN/MIN	32.1	32.1	32.1	32.1	32.1			

NUMBER OF CRYSTALS PULLED PER WEEK AND TIME DISTRIBUTION

	MON.	TUE.	WED.	THU.	FRI.	SAT.	SUN.	TOTAL
WORKDAY, HOURS :	16.0	16.0	16.0	16.0	16.0			80.0
NO OF CRYSTAL STARTS	2.0	2.0	2.0	2.0	2.0			10.0
LAST XTL,PRTN OF MAX								
DAILY SETUP TIME,HRS	2.5	2.5	2.0	2.0	1.0			10.0
CRUCIBLE HEAT-UP,HRS	1.0	1.0	1.0	1.0	1.0			5.0
CRYSTAL PULLING, HRS	12.5	12.5	12.5	12.5	12.5			62.5
REM UNPROD TIME, HRS			0.5	0.5	1.5			2.5
TOTAL TIME, HOURS	16.0	16.0	16.0	16.0	16.0			80.0

NUMBER OF CRYSTALS PULLED PER WEEK AND PERCENTAGE TIME DISTRIBUTION

	MON.	TUE.	WED.	THU.	FRI.	SAT.	SUN.	TOTAL
WORKDAY, HOURS :	16.0	16.0	16.0	16.0	16.0			80.0
NO OF CRYSTAL STARTS	2.0	2.0	2.0	2.0	2.0			10.0
LAST XTL,PCT OF MAX								
DAILY SETUP TIME,PCT	15.6	15.6	12.5	12.5	6.3			12.5
CRUCIBLE HEAT-UP,PCT	6.3	6.3	6.3	6.3	6.3			6.3
CRYSTAL PULLING, PCT	78.1	78.1	78.1	78.1	78.1			78.1
REM UNPROD TIME, PCT			3.1	3.1	9.4			3.1
TOTAL TIME, PERCENT	100.0	100.0	100.0	100.0	100.0			100.0

Fig. 10. Float-zone technology: 12-cm-diameter, 2-shift operation.

LIST OF VARIABLES AND THEIR CURRENT VALUES

CZOCHRALSKI TECHNIQUE

CRYSTAL DIAMETER (D),CM : 15
SEED AND TAIL CONES, ANGLE WITH C/L, DEGREES (AL) 30
GROWTH RATE (V2),CM/HR: 12.8
MAXIMUM CRYSTAL LENGTH, INCLUDING CONES (L), CM: 75
LAST CRYSTAL MUST BE 50 PERCENT OF MAX LENGTH TO BE STARTED
NO. OF HOURS WORKED EACH DAY OF THE WEEK (WD) : 16
NO. OF DAYS WORKED PER WEEK (DAYS) : 5
UNSCHEDULED DOWNTIME, PCT OF WORKDAY: 0
AVG SET-UP TIME (SU), HOURS: 2
AVG CRUCIBLE HEAT-UP TIME (HU), HOURS: 2.5

CRYSTAL PULLING

MAX LENGTH: 75 CM GROWTH RATE: 12.8 CM/HR · CZO TECHNIQUE· DIA, CM 15
WEEKLY VOLUME, CU-CM : 59050
WEEKLY AVG VOL,CU-CM/MIN : 12.30
WEEKLY WEIGHT, KG: 144.08

	MON.	TUE.	WED.	THU.	FRI.	SAT.	SUN.	TOTAL
WORKDAY, HOURS :	16.0	16.0	16.0	16.0	16.0			80.0
NO OF CRYSTAL STARTS	1.0	1.5	1.0	1.5	1.0			6.1
TOTAL LENGTH, METERS	0.8	1.2	0.8	1.2	0.8			4.6
VOLUME, CUBIC-CM	10193	14236	10193	14236	10193			59050
CUBIC-CM GROWN/MIN	10.6	14.8	10.6	14.8	10.6			

NUMBER OF CRYSTALS PULLED PER WEEK AND TIME DISTRIBUTION

	MON.	TUE.	WED.	THU.	FRI.	SAT.	SUN.	TOTAL
WORKDAY, HOURS :	16.0	16.0	16.0	16.0	16.0			80.0
NO OF CRYSTAL STARTS	1.0	1.0	1.0	1.0	1.0			5.0
LAST XTL,PRTN OF MAX		0.5		0.5				1.1
DAILY SETUP TIME,HRS	4.0	2.0	4.0	2.0	2.0			14.0
CRUCIBLE HEAT-UP,HRS	2.5	5.0	2.5	5.0	2.5			17.5
CRYSTAL PULLING, HRS	5.9	9.0	5.9	9.0	5.9			35.6
REM UNPROD TIME, HRS	3.6		3.6		5.6			12.9
TOTAL TIME, HOURS	16.0	16.0	16.0	16.0	16.0			80.0

NUMBER OF CRYSTALS PULLED PER WEEK AND PERCENTAGE TIME DISTRIBUTION

	MON.	TUE.	WED.	THU.	FRI.	SAT.	SUN.	TOTAL
WORKDAY, HOURS :	16.0	16.0	16.0	16.0	16.0			80.0
NO OF CRYSTAL STARTS	1.0	1.0	1.0	1.0	1.0			5.0
LAST XTL,PCT OF MAX		0.5		0.5				1.1
DAILY SETUP TIME,PCT	25.0	12.5	25.0	12.5	12.5			17.5
CRUCIBLE HEAT-UP,PCT	15.6	31.3	15.6	31.3	15.6			21.9
CRYSTAL PULLING, PCT	36.6	56.3	36.6	56.3	36.6			44.5
REM UNPROD TIME, PCT	22.8		22.8		35.3			16.2
TOTAL TIME, PERCENT	100.0	100.0	100.0	100.0	100.0			100.0

Fig. 11. Czochralski technology: 15-cm-diameter, 2-shift operation.

LIST OF VARIABLES AND THEIR CURRENT VALUES

FLOAT ZONE TECHNIQUE

CRYSTAL DIAMETER (D),CM : 15
SEED AND TAIL CONES, ANGLE WITH C/L, DEGREES (AL) 30
GROWTH RATE (V2),CM/HR: 24
MAXIMUM CRYSTAL LENGTH, INCLUDING CONES (L), CM: 150
LAST CRYSTAL MUST BE 50 PERCENT OF MAX LENGTH TO BE STARTED
NO. OF HOURS WORKED EACH DAY OF THE WEEK (WD) : 16
NO. OF DAYS WORKED PER WEEK (DAYS) : 5
UNSCHEDULED DOWNTIME, PCT OF WORKDAY: 0
AVG SET-UP TIME (SU), HOURS: 1
AVG CRUCIBLE HEAT-UP TIME (HU), HOURS: 0.5

CRYSTAL PULLING

MAX LENGTH: 150 CM GROWTH RATE: 24 CM/HR · FZ TECHNIQUE· DIA, CM 15
WEEKLY VOLUME, CU-CM : 234464
WEEKLY AVG VOL,CU-CM/MIN : 46.86
WEEKLY WEIGHT, KG: 572.09

	MON.	TUE.	WED.	THU.	FRI.	SAT.	SUN.	TOTAL
WORKDAY, HOURS :	16.0	16.0	16.0	16.0	16.0			80.0
NO OF CRYSTAL STARTS	2.0	2.0	2.0	2.0	2.0			10.0
TOTAL LENGTH, METERS	3.0	3.0	3.0	3.0	3.0			15.0
VOLUME, CUBIC-CM	46893	46893	46893	46893	46893			234464
CUBIC-CM GROWN/MIN	48.8	48.8	48.8	48.8	48.8			

NUMBER OF CRYSTALS PULLED PER WEEK AND TIME DISTRIBUTION

	MON.	TUE.	WED.	THU.	FRI.	SAT.	SUN.	TOTAL
WORKDAY, HOURS :	16.0	16.0	16.0	16.0	16.0			80.0
NO OF CRYSTAL STARTS	2.0	2.0	2.0	2.0	2.0			10.0
LAST XTL,PRTN OF MAX								
DAILY SETUP TIME,HRS	2.5	2.5	2.0	2.0	1.0			10.0
CRUCIBLE HEAT-UP,HRS	1.0	1.0	1.0	1.0	1.0			5.0
CRYSTAL PULLING, HRS	12.5	12.5	12.5	12.5	12.5			62.5
REM UNPROD TIME, HRS			0.5	0.5	1.5			2.5
TOTAL TIME, HOURS	16.0	16.0	16.0	16.0	16.0			80.0

NUMBER OF CRYSTALS PULLED PER WEEK AND PERCENTAGE TIME DISTRIBUTION

	MON.	TUE.	WED.	THU.	FRI.	SAT.	SUN.	TOTAL
WORKDAY, HOURS :	16.0	16.0	16.0	16.0	16.0			80.0
NO OF CRYSTAL STARTS	2.0	2.0	2.0	2.0	2.0			10.0
LAST XTL,PCT OF MAX								
DAILY SETUP TIME,PCT	15.6	15.6	12.5	12.5	6.3			12.5
CRUCIBLE HEAT-UP,PCT	6.3	6.3	6.3	6.3	6.3			6.3
CRYSTAL PULLING, PCT	78.1	78.1	78.1	78.1	78.1			78.1
REM UNPROD TIME, PCT			3.1	3.1	9.4			3.1
TOTAL TIME, PERCENT	100.0	100.0	100.0	100.0	100.0			100.0

Fig. 12. Float-zone technology: 15-cm-diameter, 2-shift operation

of each day where the machine remains idle. It has been set up for the next run, but insufficient time remains to heat up the polysilicon and pull a reasonably long (specified at 50% of normal length) crystal.

Another example is shown in Fig. 8, where during the first day of operation (Monday) the equipment remains idle for 4.3 hours, or 26.6% of the workday. In a more flexible production environment, 3.4 hours of overtime (2.5 + 5.2 - 4.3) would have resulted in a second crystal for the day. This problem does not happen to occur with the FZ case (Figs. 10, 11, and 12), since the conditions (technology parameters) are such that two crystal starts per day can be readily scheduled.

The foregoing points to the fact that cost-effective bulk (CZO,FZ) crystal growth for photovoltaic applications should be a 24-hour round-the-clock operation, similar in concept to a steel mill. If, for some reason, this is not possible, then working hours of equipment operators should be scheduled around the crystal-growing cycle and not around arbitrary shift hours.

Today, FZ crystallization from polysilicon into single-crystal material is not consistently achieved with one pass through the crystal, increasing processing time and

cost. Granted, float zoning is a more difficult crystal growing technique than CZO, requiring greater operator skill. This condition, however, should not become a detractor from FZ technology and could be overcome through better operator training and automation.

The cost of polysilicon rods, suitable for FZ growth, is currently about twice the cost of polysilicon for CZO growth. Even though the former require somewhat more operator attention during the manufacturing cycle and the product (polyrod) must be free of cracks, there appears to be no compelling reason why the cost of polysilicon material in any bulk form should not be essentially the same, assuming an equal demand for it in the marketplace.

Float-zone single-crystal material throughput, as one would expect from a review of the processing parameters, is considerably higher than CZO throughput. This difference is due to the variation in crystallization, or growth, rates, as shown in Table II. It is also due to the fact that longer crystals are grown with FZ than with CZO and, finally, to the variation in machine-setup and polysilicon melt-down times. This is shown graphically in Figs. 13 and 14, where weekly material volume (cm^3) vs crystal diameter (cm) is plotted for the two modes of operation. As can be

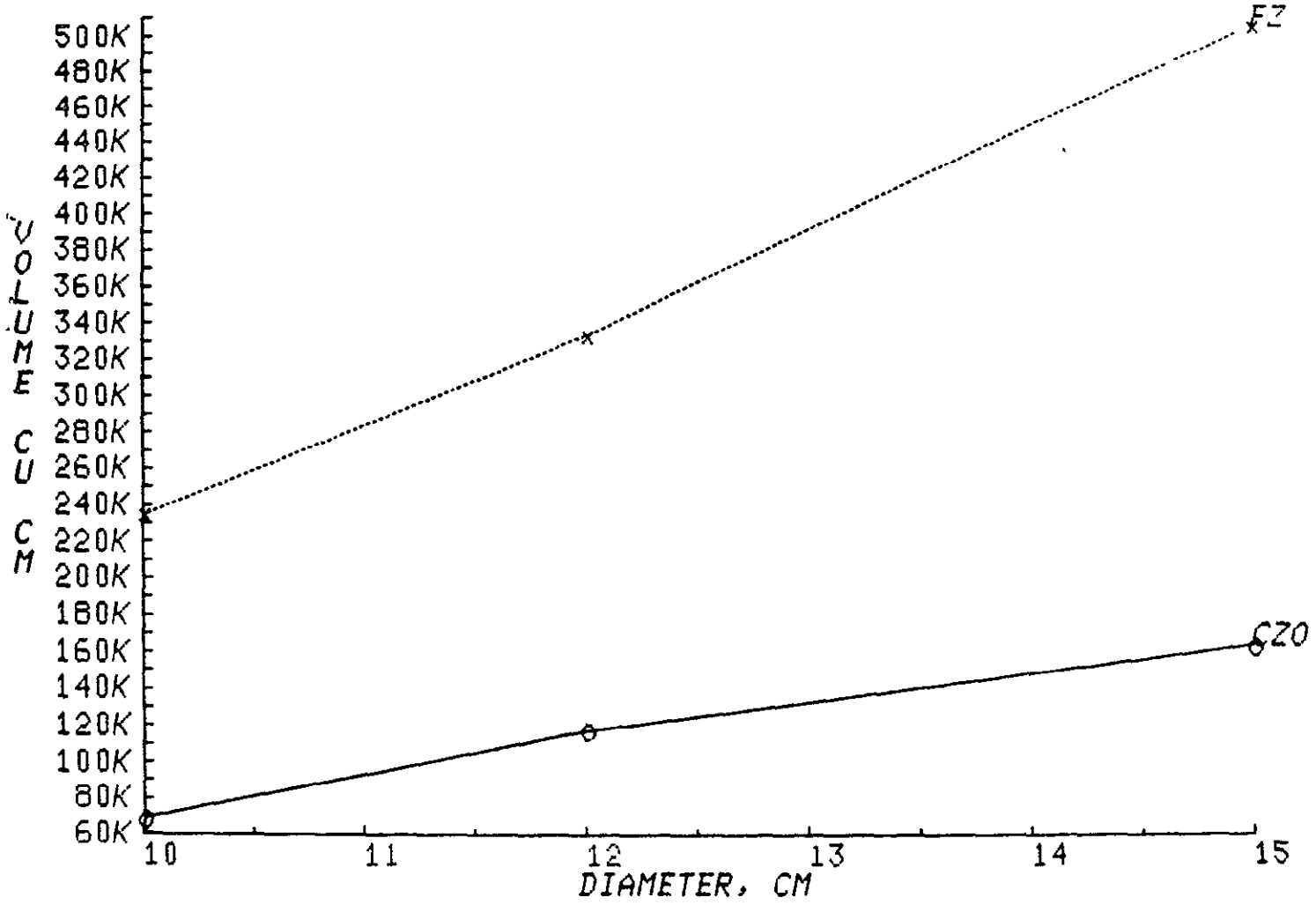

Fig. 13. Czochralski versus float-zone material throughput (7-day, 24-hour operation).

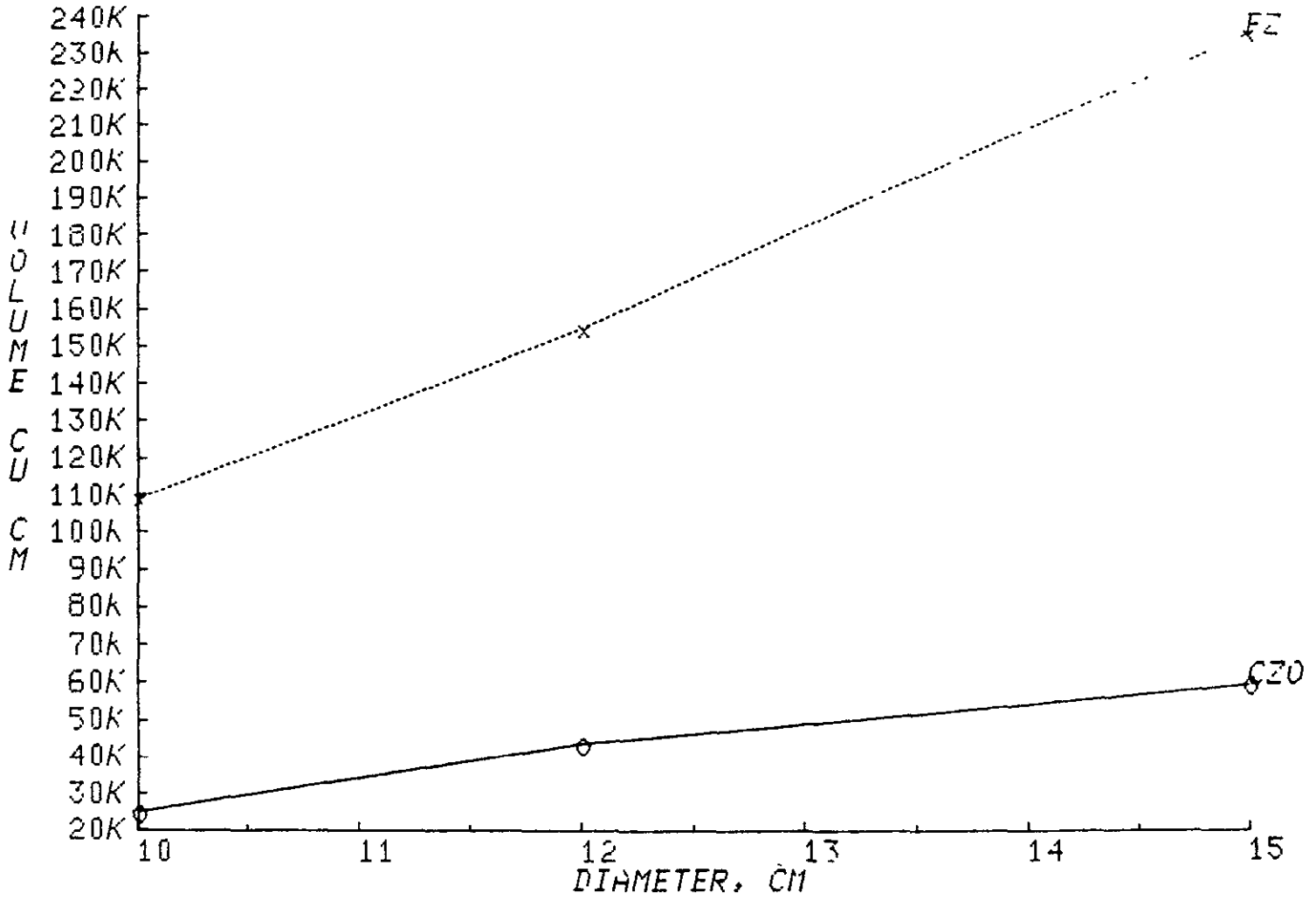

Fig. 14. Czochralski versus float-zone material throughput (5-day, 16-hour operation).

seen from Fig. 13, FZ, in this projection, outproduces CZO by a factor of 3 for all three crystal diameters chosen. For the five-day, 16-hour-per-day operation (Fig. 14), this difference is even greater because of the long CZO machine idle time discussed earlier. Since the curves for the other two projections of Table II would fall below the pictured FZ curve, this curve might be viewed as our current estimate of future FZ technology potential.

In sum, we believe that FZ technology is potentially less expensive than CZO, and a relatively small investment in technology development and equipment should solve technology-related throughput-limiting problems.

Here is our scoreboard:

	FZ	CZO
Productivity	3	1
Equipment Cost	1	1
Raw Material (Future) Cost	1	1
Crucible Cost	0	1

We conclude that the potential advantages of FZ technology have been underestimated, and that rapid action should be taken to develop FZ to the level of CZO.

4.0 CONCLUSIONS

- Float-zone technology is potentially less expensive than Czochralski technology and, consequently, should be rapidly developed and automated to the level of today's Czochralski technology.

- Float-zone technology can potentially outproduce Czochralski technology by a factor of 3.

- Cost-effective bulk (CZO, FZ) crystal growth for photovoltaic devices demands a 24-hour-per-day factory operation. If this is not possible, careful scheduling of technician and equipment is required to avoid excessively idle equipment.

5.0 ACKNOWLEDGMENT

Computer terminal support was provided by Mrs. S. A. Focht.